KAPL-P-000323
(K99136)

Recombination Processes on Low Bandgap Antimonides for Thermophotovoltaic Applications

S. Saroop, G. W. Charache

September 1999

NOTICE

KNOLLS ATOMIC POWER LABORATORY SCHENECTADY, NEW YORK 12301

Operated for the U.S. Department of Energy
by KAPL, Inc. a Lockheed Martin Company

Recombination Processes in Low Bandgap Antimonides for Thermophotovoltaic Applications

By

Sudesh Saroop

A Thesis Submitted to the Graduate

Faculty of Rensselaer Polytechnic Institute

in Partial Fulfillment of the

Requirements for the Degree of

DOCTOR OF PHILOSOPHY

Department of Electrical, Computer, and Systems Engineering

Approved by the
Examining Committee:

Prof. Ronald J. Gutmann, Thesis Advisor

Prof. Emeritus Jose M. Borrego, Co-Advisor

Prof. Ishwara B. Bhat, Member

Dr. Greg W. Charache, Member

Prof. T. Paul Chow, Member

Prof. Peter D. Persans, Member

Rensselaer Polytechnic Institute
Troy, New York

July 1999
(For Graduation August 1999)

CONTENTS

APPENDICES

LIST OF TABLES

LIST OF FIGURES

ACKNOWLEDGMENT

The author would like to thank Dr. Ronald J. Gutmann for his guidance, dedication, seemingly unending support, and for working seven days a week when needed during the entire research program. The author is deeply indebted to Dr. Jose M. Borrego for his many contributions to the research and understanding of the physical phenomena, and for always bringing a fresh perspective. The friendship and assistance of the members of the RPI TPV program, both students and staff, have been an invaluable part of the life of the author for the past four years and he is very grateful for the innumerable hours spent both at work and after hours. The contributions and support of Dr. Greg W. Charache for his insights and collaboration in the development and application of the photoreflectance system are greatly appreciated. Many thanks to Dr. Christine A. Wang and Dr. Partha S. Dutta for their excellent material growth and for providing many samples used both for system characterization as well as in the investigation of recombination mechanisms in antimonides. Finally, no words can express the feelings of the author for his family, for their support, both emotionally and financially, and especially to Mom and Dad for their encouragement to aspire to fulfill our dreams. This thesis is dedicated to each of the author's grandparents who provide the inspiration to persevere in times of hardship and to his uncle, Ashram, who first planted the seed many years ago which blossomed into the dream embodied in the pursuit of a doctoral degree.

ABSTRACT

Recombination processes in antimonide-based materials for thermophotovoltaic (TPV) devices have been investigated using a radio-frequency (RF) photoreflectance technique, in which a Nd-YAG pulsed laser is used to excite excess carriers and the short-pulse response and photoconductivity decay are monitored with an inductively-coupled non-contacting RF probe. The system has been used to characterize surface and bulk recombination mechanisms in Sb-based materials.

Both lattice-matched AlGaAsSb and GaSb have been used to double-cap epitaxial InGaAsSb active layers to evaluate bulk lifetime and surface recombination velocity with different active layer thicknesses. With an active layer doping of $2\text{x}10^{17}$ cm^{-3}, effective bulk lifetimes of 95 ns and surface recombination velocities (SRV) on the order of 10^3 cm/s have been obtained. As the laser intensity is increased the lifetime decreases, which indicates that radiative or Auger recombination dominates under these high level injection conditions. The bulk lifetime fits the radiative recombination equations well with a radiative lifetime around 200 ns for the AlGaAsSb-capped samples grown at 550 °C and 70 ns for the GaSb-capped samples grown at 525 °C. As the active layer bandgap decreases from 0.59 to 0.50 eV with GaSb caps, fitting the bulk lifetimes to a purely radiative recombination behavior shows that the radiative lifetime increases as well as the fitting error, indicating that other modes of bulk recombination play greater roles in the lower bandgap samples. The low SRV obtained and the radiative-dominated bulk recombination are indications that the material studied is of very high quality.

Commercial and in-house low-doped unpassivated bulk p-type GaSb substrates and n-type quasi-binary InGaAsSb substrates having bandgaps in the range of 0.40 to 0.62 eV have been studied with the system. Values on the order of 10^6 cm/s have been obtained for the surface recombination velocity of both sets of substrates. The dependence of bulk lifetimes of the GaSb samples (~40 ns) on injection level indicate that Shockley-Read-Hall recombination is dominant, whereas the quasi-binary substrates (25-50 ns) exhibit an inverse dependence on optical excitation energy, indicating that radiative or Auger recombination is dominant. Immersion in liquid nitrogen (77 K) reveals that at low temperatures the bulk lifetime increases in both GaSb and quasi-binary substrates, indicating that radiative recombination dominates.

1. Introduction

The basic principle governing photovoltaic devices (i.e., solar cells), the photovoltaic effect, was first observed in 1839 by Becquerel using electrolytic cells. Subsequent discoveries of the photoconductive and photovoltaic effects in Se in the 1870's led to the first description of the Se photovoltaic cell by Fritts in 1883. These discoveries laid the foundation for further development of photovoltaic device technology, with Se-based devices ultimately achieving a solar conversion efficiency of 1%. The advent of Czochralski single crystal growth of Si and diffused p-n junctions made the Si solar cell practical with a 6% conversion efficiency with improvements in fabrication and device understanding leading to a 14% efficient Si solar cell in 1958. Ensuing research emphasis was placed in the adaptation of these cells in space power systems, improvement of reliability, and reduction of cost. By the early 1970's the cost was less than \$1/cm^2 of device area or about \$60 per Watt[1]. One major limitation of this technology is that the solar radiant power density is at most 108 mW/cm^2 on a clear day with the sun at its zenith. With a theoretical maximum efficiency of 21.7% for Si, a maximum power density of 23.4 mW/cm^2 can be obtained without solar concentrators or approximately 0.5 W/cm^2 with a concentrator.

Thermophotovoltaic (TPV) devices are p-n junctions similar to photovoltaic devices. However, whereas solar cells convert the visible light from the sun into electricity, TPVs are designed to convert infrared energy into electrical energy using terrestrial heat sources. One advantage of such a system is increased power density since the cells are located close to the heat source. Another advantage is that higher efficiencies are possible with the insertion of spectral filters between the cells and the source. The filters ideally permit only the useful portion of the source spectrum (above bandgap radiation) to impinge on the cells. While filters can be used in solar cell technology to reduce cell temperature, the filters also reflect the below-bandgap radiation back to the source in TPV systems, thus requiring less fuel to maintain a given source temperature. Alternatively, selective radiators (typically ceramics, such as Yb_2O_3-Al_2O_3 or Co-doped MgO) can be used to convert the wide black-body spectrum of the heat source into narrow emissions just above the bandgap, further increasing the efficiency since the photons well above bandgap do not contribute to efficient conversion. Besides producing electrical power from a few watts up to 500 W, the exhaust heat can be used to heat a room in a cogeneration configuration. A commercial cogeneration system has been demonstrated which provides 5000 BTU/hr in addition to 20 W of continuous electricity[2].

The first proposal for a TPV device was made in 1961 by P. Aigrain, with one of the first reported devices appearing in 1963 by Wedlock[3] using a Ge p-i-n structure. This device was built around a 1600 °C heat source and achieved a conversion efficiency of 4.23%. In the last few years the material system of choice has been InGaAs because the low bandgap (0.55 eV) made feasible a 13.6% single-cell conversion efficiency[4] (out-of-cavity) with a lower radiator temperature of 1090 °C. The current state of TPV technology is focused on Sb-based compounds (GaSb, InGaSb, and InGaAsSb) with InGaAsSb lattice-matched to GaSb providing the highest performance[5].

The best performance to date has been achieved with epitaxially grown materials. These materials can be grown relatively defect-free with well controlled compositions and doping profiles, but at a high cost. In the solar cell arena, bulk grown crystals with diffused junctions have shown lower efficiencies but at a much lower cost. The commercial TPV systems available are implemented with diffused-junction bulk GaSb. Thus, besides trying to obtain peak performance from epitaxial devices, study of diffused junctions in boule-grown GaSb, InGaSb, and InGaAsSb can lead to more cost-effective systems. In order to maximize the efficiency of either approach, the electrical and optical characteristics such as absorption constant, electron and hole mobility, trap energies and densities, surface recombination velocities, and minority carrier lifetime must be known to optimize a device structure.

Photovoltaic devices depend heavily on the various carrier recombination processes which exist to return an excited system to its equilibrium state. These processes include recombination at surfaces and interfaces, Shockley-Read-Hall (SRH) recombination, Auger recombination, and, especially in III-V compounds, radiative recombination. An understanding of these processes is critical to the improvement of the materials and the design of antimonide-based TPV devices[6, 7]. A brief discription of these recombination processes is presented below and is discussed more completely in Chapter 2.

An abrupt interruption of the lattice at the surface of a crystal results in dangling bonds, which generally attract impurity atoms if not properly passivated. These dangling bonds and impurity atoms introduce energy levels within the bandgap and act as recombination centers, or sinks of free carriers, near the surface. A similar condition exists at the interface between different materials. A recombination velocity up to 10^7 cm/s is observed for an unpassivated surface. Since higher energy photons are absorbed closer to the surface, these photogenerated carriers have a high probability of recombining at the surface; therefore, poor surfaces drastically reduce the efficiency of TPV cells in this part of the spectrum.

SRH recombination is a non-radiative process whereby electrons and holes recombine at defect sites within the bulk of a crystal; these defects are crystallographic imperfections such as missing atoms, defect clusters, impurity atoms, or dislocations. The rate of recombination is proportional to the density of the defects, and can thus be reduced with improved growth and preparation techniques. Furthermore, recombination centers are most efficient when the defect energy level is near the middle of the semiconductor bandgap. Defects can also result in free-carrier trapping, in which the capture rate at trapping centers for one carrier type far exceeds that for the opposite charge, thereby effectively trapping carriers for relatively long times with a low probability for recombination with the opposite type. Separation of free-carrier recombination and free-carrier trapping at defect levels can be difficult.

Radiative recombination is a band-to-band transition requiring a free electron and free hole producing a photon, and is the inverse of photogeneration. From conservation of momentum considerations, this process occurs predominantly in direct-bandgap semiconductors. Since two carriers are required, the probability of occurrence is proportional to the electron-hole (*np*) product thereby producing shorter lifetimes than the SRH process. In GaAs the calculated lifetimes[8] range from less than 1 ns at 1.6×10^{19} cm^{-3} to >10 ns at 4.0×10^{17} cm^{-3}, while in GaSb radiative-limited lifetimes are expected[9] to be on the order of 100 ns at 10^{17} cm^{-3} and 1 ns at 10^{19} cm^{-3} carrier concentrations. In addition, due to the high absorption in direct-bandgap semiconductors, the emitted photon could be reabsorbed to create another hole-electron pair. This photon recycling has the effect of increasing the measured lifetimes several times over, depending on the sample thickness and surface passivation.

In Auger recombination, the energy from a band-to-band hole-electron pair is transformed into the kinetic energy of a third particle. The probability for this process varies as n^2p or np^2 and produces relatively short lifetimes (< 1ns), especially in heavily-doped or highly excited semiconductors. Both Auger and radiative recombination are processes intrinsic to the semiconductor and are determined purely by the band structure of the material and effective masses of the carriers.

The three bulk processes (SRH, radiative, and Auger recombination) combine to give an effective bulk lifetime which determines the dark current since TPV devices operate with a forward bias. The dark current (due to carrier recombination) diminishes the amount of current the device can produce under illumination and decreases the amount of voltage that can be generated across the device. Increasing the bulk lifetime and reducing the surface recombination velocity are critical factors in improving TPV cells. Understanding these effects in device-quality epitaxial films and in substrates is the emphasis of this research.

The remainder of this thesis is organized as follows. In Chapter 2, the structure and design of a TPV device is discussed, outlining the dependence of the final design on the recombination lifetime. The various components of the lifetime are discussed in detail, as well as other conventional measurement techniques. Chapter 3 describes the RF photoreflectance system used in this research outlining the design, calibration, and capabilities. The bulk and surface properties of epitaxial InGaAsSb films are characterized in Chapter 4, while GaSb and InGaAsSb substrates are characterized in Chapter 5. The results are summarized in

Chapter 6, including suggestions for further work. The software used in this work to record sample lifetimes and to model the bulk recombination mechanisms are presented in Appendices A and B, respectively. Appendix C describes a model for SRH recombination presented as an alternate model for the analysis of the bulk lifetimes of the epitaxial InGaAsSb samples of Chapter 4. The optical constants used in the analyses throughout Chapters 4 and 5 are given in Appendix D for each bandgap considered and the raw decay transients for each substrate analyzed in Chapter 5 can be found in Appendix E.

2. Technical Background

In this chapter, the factors which affect the efficiency of TPV devices are presented, starting with the phenomenological description of the device operation and followed by the role of the minority carrier lifetime and surface recombination in implementing the device. Descriptions of the various recombination mechanisms, including their dependence on carrier concentration and temperature, are presented in detail. Finally, various techniques are described for experimental determination of lifetime, emphasizing the microwave reflectance system since it is the foundation for the RF photoreflectance system developed in this thesis.

2.1. Thermophotovoltaic Devices

The efficient operation of photovoltaic devices, of which TPVs are a subset, depends on three processes. First, a photon impinging on the surface of the device must be absorbed in a manner which produces a free electron-hole pair. Secondly, the carriers must be generated in a region where they have a high probability of diffusing into the depletion region formed at the metallurgical junction of the p- and n-layers of the device; in the vicinity of the junction a built-in electric field separates the minority and majority carriers, accelerating the minority carriers into the opposite layer. While absorption and diffusion occur in all semiconductors, the presence of the electric field permits the separation of the electron-hole pairs which then accumulate at opposite terminals of the device generating an electric potential. Finally, the separated photogenerated carriers must be collected in an external circuit to power the load.

2.1.1. Photon Absorption in Semiconductors

Photons may be absorbed in a semiconductor by lattice absorption, free carrier absorption, defect-to-band edge transitions, and band-to-band transitions. Lattice absorption occurs as the result of photon-phonon interactions whereas free-carrier absorption is an optically induced intra-band electronic transition within an unfilled band. Defect-to-band edge and band-to-band transitions occur when the energy from a photon frees a carrier from an atom in a lattice site – a unionized impurity atom in the former case and a semiconductor atom in the latter. Since only band-to-band and defect-to-band edge absorption result in an increase in carrier concentration, efficient TPV device operation requires that an active layer material is selected in which the occurrence of lattice and free-carrier absorption is minimized.

For photon absorption by lattice vibration to occur, the momentum (h/λ) and energy ($h\nu$) of the photon must be transferred to a phonon. From conservation of momentum, only interactions with phonons of low crystal momentum, k, are possible. This range of momenta is very small compared to the edge of the Brillouin zone edge ($2\pi/a$). Under these conditions, the lattice vibrations correspond to damped harmonic oscillations with the result that the lattice displacement[10] is given by

$$\boldsymbol{r} = \frac{QE/\mu}{(\omega_{TO}^2 - \omega^2) - j\omega\gamma} \tag{2.1}$$

where Q is the effective charge on the atoms in the lattice, $\boldsymbol{E}$ is the electric field of the photon, ω is the angular frequency of the oscillating electric field, μ is the reduced mass of the atoms in the lattice, γ is the damping factor, and ω_{TO} is the transverse optical phonon frequency, which is nearly constant for $k \approx 0$. In compound semiconductors, the periodic displacement of the anion and cation leads to an oscillating polarization $\boldsymbol{P}=Q\boldsymbol{r}N$, where N is the atomic density. Since $\boldsymbol{P}=(\varepsilon-\varepsilon_0)\boldsymbol{E}$, the complex permittivity (ε) can be solved to obtain

$$\varepsilon = \varepsilon_0 + \frac{Q^2 N / \mu}{\omega_{TO}^2 - \omega^2 - j\omega\gamma} \quad , \tag{2.2}$$

where ε_0 is the permittivity of free space. The absorption constant is defined by $\alpha=2\omega\mathbf{Im}(n)/c$ where c is the speed of light in vacuum and n is the index of refraction given by $(\varepsilon/\varepsilon_0)^{1/2}$. The absorption constant peaks for frequencies near ω_{TO} and decreases rapidly on either side. For GaSb and InAs, the values[11] for ω_{TO} are 224 cm^{-1} and 220 cm^{-1}, respectively, which result in phonon absorption being significant for photons with energies near 27 meV. Thus, very little phonon absorption takes place in the near-infrared region.

Free carriers can move over many interatomic distances and have a greater response to external fields than to local fields. Therefore, they may be regarded as a plasma and treated within the Drude free electron model wherein electrons move in random directions. The application of an external electric field imposes a force $-q\boldsymbol{E}$ which gives rise to a drift velocity of the ensemble. However, the electrons do periodically undergo scattering events, which occur on average every τ seconds. The displacement of the carriers can then be described by the equation:

$$m^* \frac{d^2\boldsymbol{r}}{dt^2} + \frac{m^*}{\tau}\frac{d\boldsymbol{r}}{dt} = -q\boldsymbol{E} \tag{2.3}$$

where m^* is the effective mass of the electron, and $\boldsymbol{r}$ is its position. Assuming a time-harmonic dependence for the applied electric field with angular frequency ω yields the following result for the displacement:

$$\boldsymbol{r} = \frac{qE/m^*}{\omega^2 + j\omega/\tau} \quad . \tag{2.4}$$

The periodic displacement of the electrons leads to an oscillating polarization $\boldsymbol{P} = -q\boldsymbol{r}n$, where n is the density of carriers. Solving for the complex permittivity gives

$$\varepsilon = \varepsilon_0 - \frac{q^2 n/m^*}{\omega^2 + j\omega/\tau} = \left(1 - \frac{\omega_p^2}{\omega^2 + j\omega/\tau}\right)\varepsilon_0 \tag{2.5}$$

where $\omega_p^2 = q^2 n/m^* \varepsilon_0$ is defined as the plasma frequency. Under infrared illumination at room temperature in low to moderately doped semiconductors, it can be shown[12] that $\omega\tau >> 1$, resulting in the following expression for the absorption constant:

$$\alpha = \frac{\omega_p^2}{\omega^2 \tau c}\left(1 + \frac{\omega_p^2}{2\omega^2}\right) \quad . \tag{2.6}$$

The absorption constant is inversely proportional to the frequency of the excitation source. Therefore, free-carrier absorption is effective for longer wavelengths only and is a very weak effect for wavelengths shorter than the semiconductor bandgap cutoff wavelength (i.e., $\lambda_c = hc/E_g$).

Neither phonon absorption nor free-carrier absorption results in an increase in the number of free carriers and, hence, does not contribute to conversion of radiant energy into electrical energy and only results in a loss of efficiency. Only band-to-band transitions and defect-to-band edge transitions result in free carriers which can contribute to current generation. However, since dopant atoms are in general nearly completely ionized in typical photovoltaic devices and deep-level impurity concentrations are sufficiently small, defect-to-band edge transitions occur much less frequently than band-to-band transitions. Therefore, only band-to-band transitions are considered in some detail.

Since the momentum of light is much smaller than the momentum of a k-vector at the edge of the Brillouin zone, an electron excited from the valence band to the conduction band of a semiconductor will have approximately the same value of k before and after the transition (referred to as a direct transition). Once in the conduction band, the motion of the electron is governed by external fields, as is the vacancy left behind in the valence band, i.e., the hole. Because of the direct nature, the process occurs predominantly in direct-gap semiconductors. In indirect-gap semiconductors, the difference in k between the top of the valence band and the bottom of the conduction band must be offset by a phonon for momentum conservation (an indirect transition).

The absorption coefficient for band-to-band transitions is proportional to the probability per unit time that the transition will occur. From first order time-dependent perturbation theory[13], the transition probability is

$$W_{if} = \frac{2\pi}{\hbar}\left|H_{if}\right|^2 \rho(E_f) \tag{2.7}$$

where H_{if} is the matrix element connecting the initial and final states and $\rho(E_f)$ is the density of final states. The transition matrix element can be calculated using the Bloch functions of the valence band, $\psi_V = e^{jk_V r}u_V$, and the conduction band, $\psi_C = e^{jk_C r}u_C$, as

$$\begin{aligned} H_{if} &\propto \int \psi_V^* \nabla \psi_C d^3r = \int u_V^* e^{-jk_V \cdot r} \nabla u_C e^{ik_C \cdot r} d^3r \\ &= \int u_V^* \left(\nabla u_C\right) e^{j(k_C - k_V)\cdot r} d^3r + jk_C \int u_V^* u_C e^{j(k_C - k_V)\cdot r} d^3r \quad . \end{aligned} \tag{2.8}$$

The matrix elements evaluate to zero except under the condition $k_C = k_V$ which corresponds to a direct transition. For allowed transitions where the two wavefunctions have opposite parity, the imaginary component of H_{if} vanishes since ∇ is an odd operator, resulting in a matrix element independent of k. Therefore, the energy dependence of the absorption constant is due to the density of states. Above the bandgap, the density of states in the conduction band has a $(E-E_g)^{1/2}$ or $(\hbar\omega-E_g)^{1/2}$ dependence. Thus, band-to-band absorption is only effective for photons with energy greater than the bandgap, and increases for more energetic photons. This dependence is valid when a single pair of parabolic valence and conduction bands participates in the absorption. In reality, the presence of multiple conduction and valence bands and the Coulombic attraction between free electrons and holes (excitons) leads to fine structure superimposed on the simple single-band absorption spectrum.

2.1.2. Thermophotovoltaic Device Design

Free carriers in the valence and conduction bands are responsible for the photogenerated current. The magnitude of the current depends upon the wavelength of the incident light, reflection coefficient of the front surface, electrical properties of the semiconductor material, and geometry of the device.

When a *p-n* junction such as that shown in Figure 2.1 is illuminated by a source having a flux intensity spectrum of $F_0(\lambda)$, carriers will be generated with a concentration distribution given by

$$G(\lambda,x) = \alpha(\lambda)F_0(\lambda)e^{-\alpha(\lambda)x} \tag{2.9}$$

where x is the distance from the incident surface (assuming no reflection) and $\alpha(\lambda)$ is the wavelength-dependent absorption constant. In a properly designed TPV cell, only a small amount of reflection occurs in the useful wavelength range with an anti-reflective (AR) coating on the front surface.

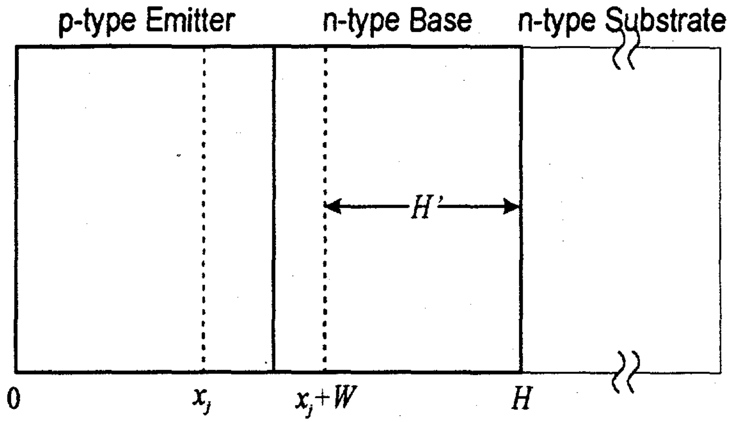

FIGURE 2.1 Dimensions for p-on-n TPV Device Under Analysis

The photogenerated current is described by the one-dimensional steady-state continuity equations under low-level injection conditions as follows:

$$\begin{aligned} G_n - \frac{n_p - n_{p0}}{\tau_n} + \frac{1}{q}\frac{dJ_n}{dx} &= 0 \\ G_p - \frac{p_n - p_{n0}}{\tau_p} - \frac{1}{q}\frac{dJ_p}{dx} &= 0 \end{aligned} \tag{2.10}$$

where G_n (G_p) is the electron (hole) generation rate, n_p (p_n) is the electron (hole) concentration in the p (n) layer, n_{p0} (p_{n0}) is the equilibrium electron (hole) concentration in the p (n) layer, τ_n (τ_p) is the electron (hole) lifetime, and J_n (J_p) is the electron (hole) current density. Assuming the illumination is composed of above-bandgap monochromatic light, band-to-band transitions generate equal numbers of electrons and holes per unit time, or

$G_n = G_p \equiv G$.

To solve for the current densities, the drift-diffusion equations are used which relate the current densities to the minority-carrier concentrations and the electric field, E, as

$$\begin{aligned} J_p &= q\mu_p p_n E - qD_p \frac{dp_n}{dx} \\ J_n &= q\mu_n n_p E + qD_n \frac{dn_p}{dx} \end{aligned} \tag{2.11}$$

where μ_n (μ_p) is the electron (hole) mobility, and D_n (D_p) is the electron (hole) diffusion constant. In a uniformly-doped layer, the absence of a concentration gradient results in no electric field. However, at the metallurgical junction between uniformly-doped *n*- and *p*-layers, a depletion layer forms as the majority carriers are attracted to the oppositely-doped layers due to the diffusion potential, leaving behind unneutralized dopant atoms. The oppositely charged dopant atoms create an electric field in the depletion region.

In the field-free regions of the device, Eqs. (2.9), (2.10), and (2.11) can be combined to give

$$\begin{aligned} D_p \frac{d^2 p_n}{dx^2} + \alpha F_0 e^{-\alpha x} - \frac{p_n - p_{n0}}{\tau_p} &= 0 \\ D_n \frac{d^2 n_p}{dx^2} + \alpha F_0 e^{-\alpha x} - \frac{n_p - n_{p0}}{\tau_n} &= 0 \end{aligned} \tag{2.12}$$

where a monochromatic light source has been assumed, thereby removing the wavelength dependence of α and F_0. If the light is incident on the *p*-layer, i.e., the emitter, surface recombination at the front gives the following boundary condition at $x=0$:

$$D_n \frac{d(n_p - n_{p0})}{dx} = S_n (n_p - n_{p0}) \tag{2.13}$$

where S_n is the surface recombination velocity for electrons. At the edge of the depletion layer ($x=x_j$), the electric field sweeps away excess carriers causing n_p-$n_{p0} \approx 0$. The electron concentration can be solved for under these conditions and the electron current density can be obtained[14] from Eq. (2.11) using the electron concentration to give

$$J_n = \frac{q\alpha F_0 L_n}{\alpha^2 L_n^2 - 1} \times \left[\frac{\left(\frac{S_n L_n}{D_n} + \alpha L_n\right) - e^{-\alpha x_j}\left(\frac{S_n L_n}{D_n}\cosh\frac{x_j}{L_n} + \sinh\frac{x_j}{L_n}\right)}{\left(\frac{S_n L_n}{D_n}\right)\sinh\frac{x_j}{L_n} + \cosh\frac{x_j}{L_n}} - \alpha L_n e^{-\alpha x_j} \right] \tag{2.14}$$

where L_n is the electron diffusion length given by $L_n^2 = D_n \tau_n$.

If the emitter is sufficiently thin to permit absorption of a significant fraction of the light in the base, excess holes are generated in the base. The concentration of holes are subject to the following boundary conditions: p_n-$p_{n0} \approx 0$ at the edge of the depletion region in the base ($x=x_j+W$) due to the electric field in the depletion region, and surface recombination at the back surface of the base ($x=H$) requires that

$$D_p \frac{d(p_n - p_{n0})}{dx} = -S_p (p_n - p_{n0}) \tag{2.15}$$

where S_p is the surface recombination velocity for holes. Solving for the hole concentration in the base under these conditions and the hole current density from Eq. (2.11) gives[14]

$$J_p = \frac{q\alpha F_0 L_p}{\alpha^2 L_p^2 - 1} e^{-\alpha(x_j+W)} \times \left[\alpha L_p - \frac{\frac{S_p L_p}{D_p}\left(\cosh\frac{H'}{L_p} - e^{-\alpha H'}\right) + \sinh\frac{H'}{L_p} + \alpha L_p e^{-\alpha H'}}{\left(\frac{S_p L_p}{D_p}\right)\sinh\frac{H'}{L_p} + \cosh\frac{H'}{L_p}} \right] \tag{2.16}$$

where H' is the thickness of the neutral part of the base and L_p is the diffusion length of holes given by $L_p^2 = D_p \tau_p$. In the derivations for the electron and hole current densities, the mobility, doping, and lifetime are assumed to be uniform throughout the emitter and base. The normalized electron and hole currents are plotted in Figure 2.2 with the material parameters as shown (typical of those found in InGaAsSb TPV devices). In this example J_p decreases by 28% and J_n (four orders of magnitude greater than J_p in this case) decreases by 88% for large values of S. Thus, it is important to minimize the surface recombination velocities, especially on the front surface.

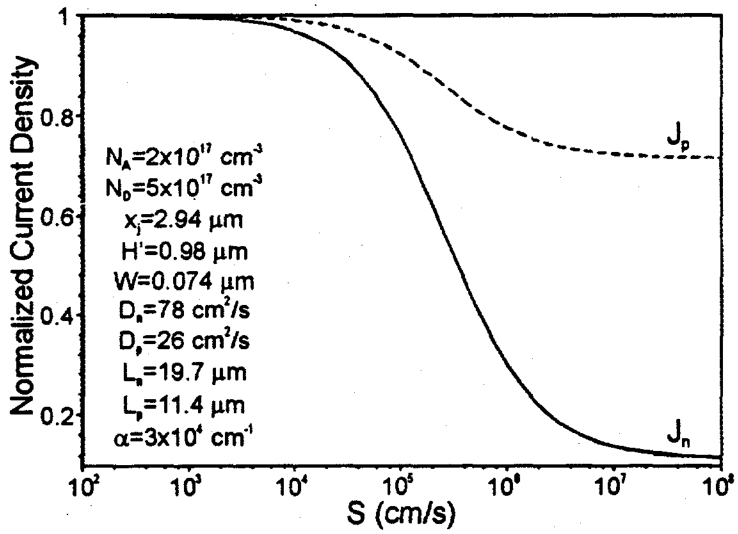

FIGURE 2.2 Normalized Electron and Hole Current Densities for a Typical TPV Device

Finally, generation within the depletion region must be considered. Since a high electric field exists in this region, any generated carriers generally will reach the emitter and base regions before recombination can occur. Thus, the generated-carrier flux density will be equal to the flux density of photons absorbed, giving the following current density:

$$J_{dr} = qF_0 e^{-\alpha x_j}\left(1 - e^{-\alpha W}\right) \quad . \tag{2.17}$$

The total photocurrent measured at the terminals of the device is given by the sum of the electron, hole, and depletion-region current. A figure of merit for photovoltaic devices is the spectral response, defined as the total photocurrent divided by qF_0, which gives the conversion efficiency or fraction of incident photons that contribute to external current.

Several factors must be considered when attempting to maximize the spectral response, such as whether most of the absorption occurs in the emitter or base. If a significant fraction of the photons are to be absorbed in the emitter, minimizing the surface recombination velocity in the emitter is necessary. In addition, maximizing the αL_n product such that $\alpha L_n >> 1$, i.e., maximizing the electron lifetime, ensures that J_n is maximized. Under these conditions, the expression in Eq. (2.14) reduces to

$$J_n \approx qF_0\left[\operatorname{sech}\frac{x_j}{L_n} - e^{-\alpha x_j}\left(\frac{\tanh\frac{x_j}{L_n}}{\alpha L_n} + 1\right)\right] \quad . \tag{2.18}$$

Furthermore, the generated carriers must be able to diffuse through the emitter to the depletion region in order to be collected, requiring that $x_j < L_n$. This constraint imposes an upper limit to the thickness of the neutral emitter subject to the diffusion length of electrons.

If this restriction is observed, the electron current density can be reduced to

$$J_n \approx qF_0\left[1-\frac{x_j^2}{L_n^2}-e^{-\alpha x_j}\right] \quad . \tag{2.19}$$

While maximizing J_n requires that αx_j>>1, i.e., all absorption occurs in the emitter, photons that pass through the emitter can be absorbed in the depletion region or base. Under these conditions, maximization of J_p requires the photons to be absorbed before arriving at the back of the base, i.e., $\alpha H'$>>1, and the generated holes to diffuse to the depletion region for collection, i.e., αL_p>>1. These requirements, and assuming the depth of the neutral base is less than the diffusion length of holes, i.e., $H'<L_p$, reduce the expression in Eq. (2.16) to

$$J_p \approx qF_0e^{-\alpha(x_j+W)}\left[1-\frac{\frac{S_pL_p}{D_p}\left(1+\frac{H'^2}{L_p^2}\right)+\frac{H'}{L_p}}{\frac{\alpha H'S_pL_p}{D_p}+\alpha L_p\left(1+\frac{H'^2}{L_p^2}\right)}\right] \quad . \tag{2.20}$$

In the limits of high and low surface recombination velocity at the back of the base,

$$\begin{aligned} J_p &\rightarrow qF_0e^{-\alpha(x_j+W)}\left[1-\frac{1}{\alpha H'}-\frac{\alpha H'}{\alpha^2L_p^2}\right] \quad \text{for } S_p \rightarrow \infty \text{ and} \\ J_p &\rightarrow qF_0e^{-\alpha(x_j+W)}\left[1-\frac{\alpha H'}{\alpha^2L_p^2+\alpha^2H'^2}\right] \quad \text{for } S_p \rightarrow 0 \end{aligned} \tag{2.21}$$

which demonstrate the relative insensitivity of J_p to S_p under the conditions above.

In order to achieve a maximum conversion efficiency, the surface recombination velocity of the front surface must be minimized and the diffusion lengths maximized (i.e., the recombination lifetimes maximized in the emitter and base regions). In addition to maximizing the spectral response, the output power should also be maximized.

The power that can be delivered from a photovoltaic cell depends not only on the efficiency with which incident power can be converted to electrical power, but on the amount of leakage inherent in a reverse-biased *p-n* junction. Furthermore, additional losses will be incurred from I^2R losses of the parasitic series resistances of ohmic contacts and grid metallization. The expressions for the output current and power are given[15] by

$$I = I_S\left(e^{\frac{q(V-IR_s)}{kT}} - 1\right) - I_L$$

$$P = I\left[\frac{kT}{q}\ln\left(\frac{I+I_L}{I_S} + 1\right) + IR_S\right] \qquad (2.22)$$

where I_S is the diode saturation current, R_S is the series resistance, k is Boltzmann's constant, T is the junction temperature, and I_L is the photocurrent. Clearly, minimizing I_S results in greater output current and power. Assuming diffusion-limited current flow, the saturation current can be expressed as

$$I_S = qN_CN_V\left(\frac{1}{N_A}\sqrt{\frac{D_n}{\tau_n}} + \frac{1}{N_D}\sqrt{\frac{D_p}{\tau_p}}\right)e^{-\frac{E_g}{kT}} \qquad (2.23)$$

where N_C and N_V are the density of states in the conduction and valence bands, respectively, E_g is the energy bandgap, and N_A and N_D are the doping concentration in the emitter and base, respectively. Hence, I_S is minimized as a result of maximizing the recombination lifetime in the emitter and base regions.

2.2. Recombination Processes

The efficiency of thermophotovoltaic devices depends on the various recombination mechanisms. An understanding of the physics of these processes provides guidelines for the selection and preparation of semiconductor materials for the device.

2.2.1. Radiative Recombination

Radiative recombination is the inverse process of direct band-to-band photon absorption and, therefore, has the same dependence on band structure. Hence, the probability for this event to occur under thermal equilibrium conditions can be derived from the sum of the probabilities of photon absorption for all electron-hole pairs having an energy separation equal to the photon energy. However, a much simpler approach proposed by van Roosbroeck and Shockley[16] is to start with the measured optical absorption constant, corrected for free-carrier absorption, which yields the strength of interaction between electron-hole pairs at a given energy separation. Combining the corrected absorption constant, α_i, with the Plank distribution for photon density at thermal equilibrium gives the radiative generation rate, G_r, which is the same as the spontaneous radiative recombination rate in thermal equilibrium, as

$$G_r = \frac{8\pi n_R^2}{h^3 c^2} \int_0^\infty \frac{\alpha_i \cdot (\hbar\omega)^2 d(\hbar\omega)}{e^{\frac{\hbar\omega}{kT}} - 1} \approx \frac{8\pi n_R^2}{h^3 c^2} \int_0^\infty \alpha_i \cdot (\hbar\omega)^2 e^{-\frac{\hbar\omega}{kT}} d(\hbar\omega) \qquad (2.24)$$

where n_R is the index of refraction, and c is the speed of light. The approximation in the right-hand-side of the expression is the result of imposing that $E_g >> kT$ in semiconductors of interest.

Radiative recombination can be decomposed into spontaneous and stimulated emission components, i.e., $r_r = r_{sp} + r_{st}$ in general and $R_r = R_{sp} + R_{st} = G_r$ in thermal equilibrium. Spontaneous emission occurs as a result of the "lifetime" of a metastable excited state, whereas stimulated emission is the result of the interaction between the electric and magnetic fields of a photon and the wavefunction of an excited electron. In thermal equilibrium the ratio of spontaneous to stimulated rates at a given photon energy[17] is $e^{\hbar\omega/kT}-1$.

When thermal equilibrium is disturbed, the radiative recombination components are modified with the factor np/n_i^2 for non-degenerate cases, neglecting the effect of photon recycling. The total recombination rate is

$$r_r = r_{sp} + r_{st} = \left(R_{sp} + R_{st}\right)\frac{np}{n_i^2} = G_r \frac{np}{n_i^2} \quad . \tag{2.25}$$

Therefore, assuming no spatial dependence, the continuity equation gives

$$\begin{aligned} \frac{dn}{dt} &= g_r - r_r = -G_r \frac{np - n_i^2}{n_i^2} = -G_r \frac{n_0 p' + p_0 n' + n' p'}{n_i^2} \\ &= -G_r \frac{n'\left(n_0 + p_0 + n'\right)}{n_i^2} \end{aligned} \tag{2.26}$$

where the simplification that $n'=p'$ has been employed in the last step. Thus, the radiative recombination lifetime can be written as

$$\tau_R = \frac{n_i^2}{G_r\left(n_0 + p_0 + n'\right)} \tag{2.27}$$

which exhibits an inverse dependence on carrier concentration in high-level injection, becoming constant in low-level injection.

When the temperature of the semiconductor is increased, the number of equilibrium photons increases at all frequencies. This causes a change in G_r which depends on the distribution of photons with energy above the bandgap. Blakemore[18] gives an approximate temperature dependence proportional to $e^{-(Eg+\delta)/kT}$ where δ is a small value compared to the bandgap. Hence an increase in G_r is expected with temperature resulting in a radiative lifetime proportional to $T^{3}e^{\delta/kT}$ which has an inverse temperature dependence at low temperatures and a direct dependence at room temperature.

2.2.2. Auger Recombination

Auger recombination occurs as the energy and momentum of two carriers, an electron in the conduction band and a hole in the valence band, are transferred to a third carrier, another electron or hole. This process is the inverse of the impact ionization process, which can be split into two types: electron-electron collisions and hole-hole collisions. At equilibrium, their generation rates, G_{ee} and G_{hh}, are equal to the Auger recombination rates, R_{ee} and R_{hh}. Since the third carrier can acquire a continuous range of momenta, unlike the relatively small discrete momentum of a photon, this process is not limited to direct transitions. In semiconductors with heavy holes ($m_C/m_V<1$), R_{ee} is typically the dominant process. However, when the material is doped strongly p-type, the greater hole concentration results in R_{hh} being dominant.

In order to evaluate the equilibrium recombination rate, the nature and occupancy of the valence and conduction bands must be known. Typically, Bloch functions are assumed for the wavefunctions in the valence and conduction bands and their occupancy is described by the Fermi-Dirac distribution function. The interaction between the recombining particles is Coulombic in nature. In degenerate semiconductors, however, when the doping level approaches or exceeds the density of states the Coulomb potential is screened due to the effect of the high concentration of majority carriers. Potential screening will not be considered here, since TPV materials are not so heavily doped in general.

The transition probability is described in terms of matrix elements of the interaction Hamiltonian in perturbation theory. The sum of the matrix elements is taken over all permissible initial and final states, weighted by the respective occupancy probabilities. The resulting thermal equilibrium generation rate due to *e-e* processes is given by Beattie and Landsberg[19] as

$$G_{ee} = \frac{8(2\pi)^{5/2} q^4 m_C \left|F_1 F_2\right|^2 n_0 \left(kT/E_g\right)^{3/2}}{h^3 \varepsilon^2 (1+\zeta)^{1/2} (1+2\zeta)} e^{-\frac{1+2\zeta}{1+\zeta}\frac{E_g}{kT}} \tag{2.28}$$

where $\zeta = m_C/m_V$, F_1 and F_2 are the overlap integrals of the periodic parts of the Bloch functions, u_C and u_V, and given by

$$F_1 = \int u_C^* u_V d^3r \,, \quad F_2 = \int u_C^* u_C d^3r \quad . \tag{2.29}$$

The overlap integrals contain the information of the periodic potential of the lattice and is, therefore, calculated for each semiconductor. A similar expression can be written for *h-h* processes as

$$G_{hh} = \frac{8(2\pi)^{5/2} q^4 m_C \left|F_1 F_2\right|^2 p_0 \left(kT/E_g\right)^{3/2}}{h^3 \varepsilon^2 (1+1/\zeta)^{1/2} (1+2/\zeta)} e^{-\frac{2+\zeta}{1+\zeta}\frac{E_g}{kT}} \quad . \tag{2.30}$$

Since *e-e* recombination involves two electrons and one hole, the recombination rate in a non-equilibrium state should be proportional to n^2p. Similarly, *h-h* recombination should be proportional to p^2n. Thus,

$$r_{ee} = G_{ee}\frac{n^2 p}{n_0^2 p_0} \quad \text{and} \quad r_{hh} = G_{hh}\frac{p^2 n}{p_0^2 n_0} \quad . \tag{2.31}$$

The generation rate of impact ionization depends on the number of energetic carriers so that

$$g_{ee} = G_{ee}\frac{n}{n_0} \quad \text{and} \quad g_{hh} = G_{hh}\frac{p}{p_0} \quad . \tag{2.32}$$

Therefore, in the case of spatially independent recombination, the continuity equation can be written when both processes dominate as

$$\frac{dn}{dt} = g_{ee} + g_{hh} - r_{ee} - r_{hh} = -\frac{\left(np - n_i^2\right)\left(G_{ee}np_0 + G_{hh}pn_0\right)}{n_i^4} \quad . \tag{2.33}$$

If one process dominates, e.g., *n-n* recombination, it is convenient to rewrite the recombination in terms of G_{ee}. In so doing, the continuity equation becomes

$$\begin{aligned}\frac{dn}{dt} &= -\frac{\left(np - n_i^2\right)\left(G_{ee}n/n_0 + G_{hh}p/p_0\right)}{n_i^2} \\ &= -\frac{n_0 + p_0 + n'}{n_i^2}\frac{G_{ee}}{n_0}\left[n_0 + n' + \left(p_0 + n'\right)\frac{G_{hh}/p_0}{G_{nn}/n_0}\right] \\ &= -n'\left\{\frac{n_0 + p_0 + n'}{n_i^2}\frac{G_{ee}}{n_0}\left[n_0 + n' + \left(p_0 + n'\right)\frac{(1+\zeta)^{1/2}(1+2\zeta)}{(1+1/\zeta)^{1/2}(1+2/\zeta)}e^{-\frac{1-\zeta}{1+\zeta}\frac{E_g}{kT}}\right]\right\} \\ &= -n'\left\{\frac{n_0 + p_0 + n'}{2n_i^2\tau_i}\left[n_0 + n' + \left(p_0 + n'\right)\beta\right]\right\}\end{aligned} \tag{2.33}$$

where the quantity in curly braces is identified as the reciprocal of the Auger lifetime, with τ_i defined as the intrinsic Auger lifetime given by

$$\tau_i = \frac{h^3\varepsilon^2(1+\zeta)^{1/2}(1+2\zeta)}{16(2\pi)^{5/2}q^4 m_C |F_1F_2|^2 (kT/E_g)^{3/2}} e^{\frac{1+2\zeta}{1+\zeta}\frac{E_g}{kT}}$$
$$= \frac{3.8\times10^{-18}\varepsilon^2(1+\zeta)^{1/2}(1+2\zeta)}{\frac{m_C}{m_0}|F_1F_2|^2(kT/E_g)^{3/2}} e^{\frac{1+2\zeta}{1+\zeta}\frac{E_g}{kT}} \quad . \tag{2.34}$$

Under high-level injection, n' is much greater than n_0 or p_0 and the high-level Auger lifetime is given by

$$\tau_A \to \frac{2n_i^2\tau_i}{n'^2} \tag{2.35}$$

which exhibits an inverse squared dependence on carrier concentration.

The bandgap is a weak function of temperature so that the temperature dependence of the Auger lifetime on bandgap can be neglected. From Eq. (2.34), the intrinsic Auger lifetime dependence is dominated by the exponential term, which has an inverse dependence on temperature. Taking into account the $T^3e^{-Eg/kT}$ dependence of n_i^2, the Auger lifetime temperature dependence is

$$\tau_A(T) \propto T^{3/2} e^{\frac{\zeta}{1+\zeta}\frac{E_g}{kT}} \quad . \tag{2.36}$$

Since $m_C << m_V$ in the materials considered in this work, $\zeta << 1$ giving a $T^{3/2}$ dependence for the Auger lifetime.

2.2.3. Shockley-Read-Hall Recombination

An ideal intrinsic semiconductor consists of a crystal lattice with semiconductor atoms situated at very regular intervals. Extrinsic semiconductors contain a controlled concentration of dopant atoms distributed randomly throughout the lattice. However, even under the best growth and preparation conditions, a finite level of defects exists – missing atoms, dislocations, impurity atoms, or anti-site atoms. The presence of relatively small concentrations, N_t, of defects can be modeled as discrete energy levels, E_t, within the semiconductor bandgap. These additional energy levels modulate the concentration of free carriers and the rate at which excess carriers recombine.

An empty defect site participates in recombination by the capture of one type of carrier, and in the full state, by the capture of the opposite type of carrier. The ability, or capture cross-section (σ), for a defect to capture a particular carrier depends upon its charge state, which in turn depends on whether it is acceptor- or donor-like. An acceptor-like defect is negatively charged when full, and neutral when ionized; therefore, due to Coulomb attraction $\sigma_p > \sigma_n$. Conversely, a donor-like defect is neutral when full and positively charged when ionized making $\sigma_n > \sigma_p$.

The rate for electron capture from the conduction band is proportional to the concentration of free electrons, the density of empty defect sites, and the average capture coefficient for electrons, $\langle c_n \rangle$. Simultaneously, the defect emits electrons back to the conduction band at a rate proportional to the density of full defect sites, the density of empty states in the conduction band, and the emission rate. The net electron capture rate is given by the difference between the capture and emission rates from the conduction band. An analogous relationship holds for hole capture. Since recombination requires capture of both carriers, the recombination rate, U, combines both rates and can be expressed[20] as

$$U = \frac{\sigma_p \sigma_n v_{th}\left(pn - n_i^2\right)N_t}{\sigma_n\left(n + n_i e^{\frac{E_t - E_i}{kT}}\right) + \sigma_p\left(p + n_i e^{-\frac{E_t - E_i}{kT}}\right)} \tag{2.37}$$

where p and n are the electron and hole concentrations, n_i is the intrinsic concentration, E_i is the intrinsic Fermi level, and v_{th} is the carrier thermal velocity given by $(3kT/m^*)^{1/2}$. The most effective recombination centers have E_t located near E_i, since at this location the net electron and hole capture rates are nearly equal. As the defect energy moves closer to either band-edge, the capture of one carrier type becomes the dominant process and the defect effectively becomes a trap for that carrier.

For defects with energies near mid-gap and with equal capture cross-sections, the recombination rate reduces to

$$U = \frac{\sigma v_{th} N_t\left(pn - n_i^2\right)}{n + p + n_i} \quad . \tag{2.38}$$

Under low-level optical injection, the excess carrier concentration ($n'=p'$) is much smaller than the majority carrier concentration. Since $p=p_0+p'$ and $n=n_0+n'$, $pn-n_i^2 \approx p_0 n'$ in p-type material and $n_0 p'$ in n-type material and the resulting recombination rates are

$$U = \begin{cases} \sigma_n v_{th} N_t n' \text{ or } n'/\tau_n, & \text{p-type} \\ \sigma_p v_{th} N_t p' \text{ or } p'/\tau_p, & \text{n-type} \end{cases} \quad . \tag{2.39}$$

Under high-level injection, the excess carrier concentration becomes greater than the majority carrier concentration so that $pn-n_i^2 \approx p'n'$, and even without requiring equal capture cross-sections, the expression in (2.37) reduces to

$$U = \frac{\sigma_p \sigma_n v_{th} N_t n'^2}{n'\left(\sigma_p + \sigma_n\right)} = \frac{n'}{\dfrac{1}{\sigma_n v_{th} N_t} + \dfrac{1}{\sigma_p v_{th} N_t}} = \frac{n'}{\tau_n + \tau_p} \quad . \tag{2.40}$$

Therefore, Shockley-Read-Hall (SRH) recombination is characterized by a low-level lifetime (τ_n or τ_p) that increases to τ_n+τ_p in high-level injection. The largest contribution to temperature dependence of the SRH lifetime in either extreme of injection (Eq. (2.39) or (2.40)) is due to the σv_{th} product assuming the defect occupancy (N_t) is relatively insensitive to temperature changes, which is generally true for recombination centers with energy close to midgap. Thus, the SRH lifetime is expected to have a $T^{-1/2}$ dependence when the capture cross-section is independent of temperature.

2.2.4. Surface Effects in Epitaxial and Substrate Materials

Shockley[21] associated electron-hole recombination at the surface of crystals with localized surface flaws based upon experiments on minority carrier motion. The description of the process follows that of Shockley-Read-Hall recombination. Therefore, the rate depends upon the position of the surface flaw within the bandgap relative to the Fermi energy, its occupancy, and the presence of a surface barrier. The properties of the surface states are dependent upon the condition of the surface (e.g., degree of polish) as well as its chemical state (e.g., degree of passivation).

Recombination at a surface results in a flow of holes and electrons towards the surface as long as excess carriers are present, creating a surface depletion layer. The rate of the recombination, and the recombination current density, is proportional to the surface recombination velocity and the density of excess carriers at the surface. A poor surface with $S \gg D/W$, where D is the diffusion constant and W is the thickness of the active layer, corresponds to a perfect sink for excess carriers, whereas when S=0 the surface is a perfect reflector. Since S is the velocity at which minority carriers approach the surface, the upper limit is given by the unilateral mean velocity[22] $(kT/2\pi m^*)^{1/2}$ which is 1.38×10^7 cm/s in 0.55 eV InGaAsSb lattice-matched to GaSb.

By analogy with Equation (2.38), the rate of recombination per unit surface area due to N_{rs} recombination centers per unit area can be written[23] as

$$U_s = \frac{S_{n0}S_{p0}\left(p_s n_s - n_i^2\right)}{S_{n0}(n_1 + n_s) + S_{p0}(p_1 + p_s)} \tag{2.41}$$

where n_1 and p_1 are the equilibrium electron and hole concentration with the Fermi level located at the trap energy level, n_s and p_s are the carrier densities at the surface, and assuming A_n and A_p are the capture cross-sections at the surface, the capture rates are given by

$$S_{p0} = A_p v_{th} N_{rs} \quad \text{and} \quad S_{n0} = A_n v_{th} N_{rs} \quad . \tag{2.42}$$

Defining $n_s = n_{s0} + n_s'$ and $p_s = p_{s0} + p_s'$, where n_{s0} and p_{s0} are the equilibrium carrier concentrations and n_s' and p_s' are the excess carrier concentrations at the surface, under low-level injection conditions Equation (2.41) can be rewritten as

$$U_s = \frac{(n_{s0} + p_{s0})n_s' S_{n0} S_{p0}}{(n_1 + n_s)S_{n0} + (p_1 + p_s)S_{p0}} \quad . \tag{2.43}$$

Furthermore, with $u_0 = \frac{1}{2}\ln(S_{n0}/S_{p0})$, $u_r = \ln(n_1/n_i) = \ln(n_i/p_1)$, and $u_s = \ln(n_s/n_i) = \ln(n_i/p_s)$ the surface recombination velocity in low-level injection can be expressed as

$$S = \frac{U_s}{n_s'} = \frac{(n_{s0} + p_{s0})\sqrt{S_{p0}S_{n0}}}{2n_i\left[\cosh(u_r - u_0) + \cosh(u_s - u_0)\right]} \quad , \tag{2.44}$$

which is maximized when $u_s=u_0$, i.e., when $S_{n0}/S_{p0}=A_n/A_p=(n_s/n_i)^2=n_s/p_s$. The physical implication of this is that since the recombination process requires capture of both carrier types, the SRV is maximum when the ratio of the concentrations of each carrier type matches the ratio of the respective capture cross-sections.

Under low-level injection in a p-type layer, for example, Equation (2.43) gives $S=S_{n0}$. In high-level injection the SRV is obtained from Equation (2.41) when $n_s=p_s=n_s'$; taking the limit as n_s' becomes much greater than the other quantities in the equation gives

$$S = \frac{S_{p0}S_{n0}}{S_{p0} + S_{n0}} = \frac{1}{1/S_{n0} + 1/S_{p0}} \quad . \tag{2.45}$$

Thus, in low-level injection the SRV is limited by minority carrier capture, while in high-level injection, the SRV is less than the values of S_{n0} and S_{p0}, which can be interpreted in a manner analogous to that of the high-level SRH lifetime, i.e., since the surface lifetime is inversely proportional to S, $\tau_S=\tau_{Sn}+\tau_{Sp}$. The temperature dependence can be inferred from the Av_{th} product which results in a $T^{1/2}$ dependence for S if the capture cross-sections are assumed to be temperature independent.

2.2.5. Trapping

When a semiconductor contains a large concentration of defects, such that the trap density is no longer insignificant compared to the background doping, the assumption that equal numbers of electrons and holes are generated with each photon is no longer valid. This is due to the preferential trapping of one carrier type, since the capture rate for the carrier overwhelms that of the other type. Once captured, the carrier is subsequently re-emitted to the conduction or valence band where recombination may then follow via mechanisms of the preceding sections. In the case of electron capture, this process results in an effective lifetime given[24] by

$$\tau_n' = \frac{\tau_n\left(1+b+b\dfrac{\tau_2}{\tau_1}\right)}{1+b} \quad , \tag{2.46}$$

where $b=\mu_n/\mu_p$, τ_n is the recombination lifetime, τ_1 is the average time an electron spends in the conduction band before trap capture, and τ_2 is the average time an electron spends in the trap. The result is an effective lifetime that can be much longer than the recombination lifetime. The effect of trapping can be minimized[24] by providing a constant excess carrier concentration, with a steady-state illumination for example, which serves to fill traps and, thus, reduces their effect on transient decay measurements.

2.3. Survey of Experimental Techniques for Lifetime Measurement

Experimental determination of carrier lifetime in single-layer semiconductor samples can be achieved by observation of one of three effects: (1) excess carrier concentration results in increased sample conductivity, (2) carriers that recombine radiatively emit photons at the energy of the bandgap, or (3) the presence of large numbers of excess carriers enhance free-carrier absorption. Systems have been developed to monitor the relaxation of these effects after a sample has been excited to generate significant excess carriers. A variety of measurement techniques can be found in recent textbooks[25, 26]. The microwave reflectance technique is described in detail in the next section (2.4.1).

2.3.1. Conductivity Measurements

Early measurements of the majority carrier lifetime were based on the photoconductivity (PC) effect[27] where the change in sample conductivity following uniform illumination by a pulse of light is measured directly as the voltage drop across the length of the sample. Measurements by this technique depend upon the ability to make adequate ohmic contacts to the material and a light source with a decay faster than the lifetime of the sample. The main drawback is the need to deposit and anneal metal contacts completely over opposite faces of the sample, which is not desirable for samples early in the process cycle. Furthermore, use of annealed contacts requires some temperature cycling of the sample that can vary the sample lifetime, thereby increasing experimental error. However, the technique is simple to implement, requires little calibration, and is still in use[28].

A similar technique based on the photoelectromagnetic (PEM) effect has a magnetic field aligned orthogonally to both the current path and the plane of constant incident light; the requirement here is that the light be absorbed close to the surface. As the photogenerated carriers diffuse into the sample, the carriers are deflected in opposite directions according to their charge giving rise to a short-circuit current. Due to the dependence on diffusion of minority carriers, PEM measures minority carrier lifetime. Kurnick and Zitter[29] demonstrated that PEM measurement has the advantage over PC measurement in that the SRV can be measured by varying the strength of the magnetic field. However, PEM short-circuit currents are generally much smaller[30] than those of PC measurements and also require ohmic contacts.

2.3.2. Photon Emission Measurements

Measurement of the luminescence emitted by samples has the advantages of being contactless and easily adaptable for measurement of relatively short lifetimes. Time resolved photoluminescence (TRPL) is most useful for materials that are strong light emitters, i.e., those demonstrating efficient radiative recombination. In these systems[31, 32], injection is achieved by pulsed lasers and the photons emitted from the sample near the bandgap energy are focused into a monochromater for detection by a photomultiplier tube. Alternatively, injection can take place via a pulsed electron beam in a cathodoluminescence system that has the added benefit of providing spatial images[33, 34].

Even though the signal measured is due to radiative recombination, the decay of the signal is governed by the effective minority carrier lifetime due to radiative, non-radiative, and surface recombination.

2.3.3. Absorption Measurements

The carrier concentration is enhanced when above bandgap light is incident on a semiconducting sample. In this excited state, the excess carriers result in increased free-carrier absorption that can be monitored with a continuous-wave (CW) below-bandgap (BBG) light source without the need for contacting the sample. The wavelength of the BBG source is selected to maximize free-carrier absorption ($\propto\lambda^2$) and to minimize lattice absorption, which is stronger at long wavelengths. Additional constraints can be placed if a minimum spot-size is required to achieve the desired spatial resolution.

Free-carrier absorption has been employed[35] to study recombination over a wide range of injection levels. The geometry of the measurement system controls the direction along which the lifetime can be spatially mapped. When the BBG probe beam is incident on a cross-sectioned sample perpendicular to the excitation pulse (normal to the face of the sample) a depth-resolved profile is obtained. When the probe beam is parallel to the excitation pulse, the lifetime can be mapped across the surface of the sample.

2.4. Non-Contacting Photoconductivity Measurement Systems

In this section, systems based on photoconductivity measurement of recombination lifetime are considered. In particular, work done previously using microwave reflectance and RF photoreflectance is discussed.

2.4.1. Microwave Reflectance

Microwave reflectance is a conductivity measurement that does not require contacts. In this system, the excess carriers are generated by a fast-decaying pulse of above-bandgap light. The concentration of excess carriers is probed using the reflection of CW microwave energy impinging on the sample that depends on the sample conductivity, sample thickness, and the depth of penetration, or skin-depth (δ) of the microwave energy.

The microwave circuit implementation depends upon the frequency being used. In the case of millimeter wavelengths, the sample is placed across the open end of a waveguide[36,37]. At lower frequencies around 10 GHz, a horn is typically used[38], and at 1-4 GHz coaxial or stripline transmission lines are used. In either case, the detector in the system measures the reflected power. In the case of a rectangular waveguide, the reflection coefficient of a sample is given[39] by

$$\Gamma(\sigma)=\frac{K_1-K_2\coth K_2L}{K_1+K_2\coth K_2L},\quad \text{where } K_1^2=\left(\frac{\pi}{a}\right)^2-\left(\frac{\omega}{c}\right)^2 \quad , \qquad (2.47)$$
$$K_2^2=\left(\frac{\pi}{a}\right)^2-\frac{\varepsilon}{\varepsilon_0}\left(\frac{\omega}{c}\right)^2+\frac{j\omega\sigma}{\varepsilon_0c^2} \quad ,$$

L is the sample thickness, ε is the sample permittivity, ε_0 is the free-space permittivity, ω is the microwave frequency, c is the speed of light, σ is the sample conductivity, and a is the wider dimension of the rectangular waveguide. The reflected power is not linearly dependent on the sample conductivity; therefore, it is necessary to ensure that the injection level is not so high as to violate the condition under which the dependence can be considered linear, i.e., $\Delta\sigma \ll \sigma$. If higher injection levels are desired, the transient must be fit with Eq. (2.47) to limit the error in measured lifetime. Furthermore, under the conditions $K_1 \ll K_2$ or $K_1 \gg K_2$, corresponding to high and low conductivity samples, respectively, Γ loses sensitivity to changes in sample conductivity. The range of sample conductivity over which an 8.6 GHz microwave reflectance system is sensitive has been estimated[40] to be $10^{-5}<\sigma<10^{-1}\ \Omega^{-1}\text{cm}^{-1}$.

Microwave reflectance systems have been used to examine ion implantation damage in SI-GaAs[41,42], evaluation of defect-free zones (DFZ), comparison of liquid-encapsulated Czochralski-grown (LEC) and horizontal gradient freeze-grown (HGF) SI-GaAs[43], heat treatment and surface passivation in Si[44], and lifetime mapping[45,46]. A few of the experiments and results are worth discussing.

In the work by Gutmann[41] *et al.*, the reflected pulse amplitude and transient decay were analyzed. The energy from a Ka band CW microwave generator was focused onto the sample using a tapered-tip antenna with a lateral resolution of 20 mils. The reflected power was measured using a square-law crystal detector through a 3 dB hybrid coupler. The samples were illuminated with a 25 W GaAs laser operating at 904 nm, a 25 W AlGaAs laser operating at 850 nm, and a 30 W/cm^2 xenon flash lamp with peak emission at 550 nm having pulse widths of 150 ns, 150 ns, and 1 µs, respectively. The different wavelengths permitted probing of recombination and trapping at different depths. Furthermore, the energy from the GaAs laser is below the bandgap of GaAs and, therefore, serves primarily to observe transitions from traps with energies within the bandgap. The samples consisted of Cr-doped SI LEC GaAs with and without ion-implanted channels. Experimentally, larger pulse responses were obtained with the AlGaAs laser on implanted samples and with the GaAs laser on un-implanted wafers. Additionally, the long decay time with the AlGaAs laser decreased in response to a constant background light source.

In the work by Heimlich[43], the peak amplitude of the microwave photoreflectance signal was measured on SI LEC GaAs with and without implanted channels and HGF GaAs from 130 to 298 K. For undoped SI GaAs, the peak amplitude measured on unimplanted samples with both a GaAs and an AlGaAs laser was found to increase monotonically with $1/T$, while that measured on implanted samples with an AlGaAs laser first decreases near 200 K and then increases for lower temperatures. Based on a two-level model it was concluded that the former effect is due to the temperature dynamics of the EL2 (a well characterized defect level in GaAs) electron capture cross section. The increased initial decay time measured with the GaAs laser at temperatures below 150 K was attributed to the EL2 capture cross section and the thermal velocity of electrons. On implanted wafers, the damage introduces another defect (trap) level within the bandgap. The observation of a long time constant decay on the implanted side of the sample whose amplitude relative to the peak amplitude decreased with decreasing temperature confirms the presence of trapping. In contrast, while the peak amplitude and initial decay times from LEC samples were spatially uniform, the peak amplitude was found to vary by as much as a factor of 20 over the surface of HGF samples that are known to have low dislocation densities. The large spatial variation was attributed to fluctuations in the trap energy level; no long decays were observed with the HGF samples. However, the temperature scans contain the same characteristics as obtained with LEC samples.

In another study[47], the surface recombination velocity of oxidized n-type 10 Ω-cm Czochralski-grown (CZ) Si wafers was measured using the relative amplitude of the long decay time "tail" of the transient using a commercial system[48] (Lifetech-88®) from SEMITEX Co., Ltd. operating at 9.6 GHz with a laser wavelength of 830 nm. It was shown that with adequate knowledge of the diffusion constant, SRVs can be measured within the range from several hundred to tens of thousands cm/s for samples with bulk lifetime between 1 μs and 1 ms. The Si samples were measured post oxidation and then 30 minutes, 24 hours, and 200 hours after an oxide strip. The measured SRV increased from ~1 cm/s after oxidation to ~1000 cm/s 30 minutes following the oxide strip. After 24 hours in an air ambient, the SRV increased to 3000 cm/s and to 7000 cm/s after 200 hours. However, the bulk lifetime was found to decrease from 3 ms to 450 μs after the strip and then increase to 1 ms 24 hours later, and then to 10 ms 200 hours later. The change in measured bulk lifetime is due to the limitation of the analysis technique; i.e., estimating bulk lifetime by subtracting similar values of surface and effective lifetimes.

2.4.2. RF Photoreflectance

Radio-frequency photoreflectance systems are an extension of microwave reflectance systems designed to perform recombination lifetime measurements on low resistivity samples. The principle of operation is the same, but in order to maintain adequate sensitivity when measuring such samples, the system impedance must be decreased to be as close to that of the sample as possible which requires moving from a waveguide based system to one with a lower impedance transmission line. Since the loss in a transmission line increases with frequency, the probe frequency must also be reduced.

Yablonivitch and Gmitter[49] described an RF photoreflectance system operating at 70 MHz and 500 MHz using either a strobe lamp or a Q-switched doubled Nd:YAG laser at injection levels exceeding 10^{15} cm^{-3}. Organometallic chemical vapor deposition (OMCVD), liquid-phase epitaxy (LPE), and molecular-beam epitaxy (MBE) GaAs samples were studied using this system. The SRH lifetime was found to be 1-2 μs in OMCVD material, 0.5-1 μs in LPE material, and 0.25-0.5 μs in MBE material which gave trap densities on the order of 10^{14} cm^{-3}. The best surface passivation was obtained with AlGaAs caps on both surfaces, having an SRV on the order of 10^3 cm/s, while chemical treatment in NH_4S resulted in an SRV around 10^4 cm/s compared to the mid-10^5 cm/s value obtained with a native oxide surface. In comparison, $In_{0.53}Ga_{0.47}As$ samples grown with InP caps had SRVs on the order of 10 cm/s, while those treated chemically with NaOH had SRVs on the order of 100 cm/s compared to the 10^4 cm/s value obtained with a native oxide surface. Finally, chemically oxidized <111> float-zone Si measured in HF resulted in an SRV of 0.22 cm/s compared to thermally oxidized samples at 100 cm/s and 10^4 cm/s for samples with a native oxide surface.

Ahrenkiel *et al.* have done extensive work with the application of RF photoreflectance systems operating at ~430 MHz in a bridge configuration using Si[50] and InGaAs[51] materials. Metallurgical grade silicon spheres 1 mm in diameter, used in the fabrication of solar cells, were measured after repeated solidification and surface removal cycles; this process has the property of purifying the spheres. Due to the high boron doping levels, microwave reflectance is unsuitable for the reasons mentioned above. Being a contactless measurement, many spheres placed in a small glass vial can be measured at a time. An order of magnitude lifetime improvement was obtained after 5 purification cycles which was correlated to a 15% improvement in the open-circuit voltage (V_{OC}) and 43% improvement in short-circuit current (I_{SC}) measured on photovoltaic cells fabricated with the Si spheres. In addition, a long decay-time tail was observed which, by varying the injection level, was determined to be due to the presence of shallow traps. In the InGaAs material system, the effect of atomic ordering was investigated. The presence of ordering on {111} planes, which leads to charge separation at the domain interfaces, was verified using transmission electron diffraction measurements where intensity fluctuations were observed. The strength of the ordering was found to vary with growth conditions and substrate miscut. Using undoped doubly-capped InGaAs grown by OMVPE on Fe-doped InP cut 2° toward the (110) direction, a fast initial decay ~ 350 ns followed by a 30 μs tail was found on the ordered samples, whereas the disordered samples were characterized by a long initial decay on the order of 10 μs followed by a faster 3 μs decay. At higher injection levels, the transient from the ordered sample rises relatively slowly and saturates prior to the 350 ns initial decay that is attributed to well filling and redistribution of charge among the potential wells formed by the band offsets present at the interfaces of the domains. The 350 ns decay is attributed to the emission rate from the various wells and was found to vary with growth temperature, i.e., degree of ordering.

3. RF Photoreflectance System Design and Calibration

GaSb commercially available[52] in both n- and p-types with carrier concentrations as low as 3-5×10^{16} cm^{3} is used as the substrate material in epitaxially-grown antimonide-based TPV devices. With quaternary InGaAsSb as the active layer, III-V ratios can be selected to achieve bandgaps in the 0.50 to 0.7 eV region while still maintaining good lattice-constant matching to the GaSb substrate. With electron mobilities typically exceeding 1000 cm^{2}/V·s, the substrate resistivity can be as high as 0.2 Ω-cm, giving a skin depth of 120 μm for the microwave frequency of 36 GHz used previously at Rensselaer Polytechnic Institute (RPI) for Si, GaAs, and InP. Since the thickness of typical substrates (500 μm) is larger than the skin depth, the sheet resistance of the substrate is determined by the skin depth and is approximately 17 Ω/□. This low sheet resistance is 3.4% of the impedance of the rectangular waveguides (500 Ω) that are used in microwave reflectance systems; moreover, the effect of doped epi-layers only reduces the sheet resistance. Because of the low relative impedance, there is little sensitivity to changes in conductivity of GaSb-based samples with this type of system. In order to maximize the responsivity on such samples, a system with a lower characteristic impedance and lower frequency is required.

In this chapter, the criteria used in the design of the RF photoreflectance system are presented. The RF electronics and laser are described in detail in separate sections along with the expected signal characteristics and calibrations which are performed to ensure repeatability of measurement. The chapter concludes with the capability of the system.

3.1. System Design Fundamentals for GaSb-based Materials

A 50 Ω characteristic impedance was selected for the RF photoreflectance system because of the wide availability of components and cables at this impedance. The frequency of the system needs to be high enough to observe decay times comparable to the lowest carrier lifetimes of interest, with a period no greater than half of the lifetime. The upper limit is determined by the parasitic losses in conductors, which increase with the square-root of the frequency, and the maximum usable frequency of the components used. A frequency around 500 MHz permits measurement of lifetimes as low as 4 ns with a sheet resistance of 5.8 mΩ/□ in Cu conductors. In addition, at this frequency the skin depth in Sb-based samples grown on GaSb substrates doped in the mid-10^{16} cm^{-3} range is 1 mm, giving a thickness-limited sheet resistance of 4.2 Ω/□.

Another requirement is an efficient means of coupling the RF energy into the sample. Radiative coupling requires at least a quarter-wave antenna, which at this frequency would be 15 cm and is much larger than the size of the samples. Instead, inductive coupling was chosen using inductors with dimensions much less than the 60 cm wavelength. The lower limit on the inductor size is determined by the capability of the fabrication technique.

3.2. RF Design

The photoreflectance system is designed to detect changes in sample conductivity by sensing the changes in the amplitude and phase of the reflected signal through the use of a homodyne detector. A schematic of the RF system is shown in Figure 3.1. The Boonton

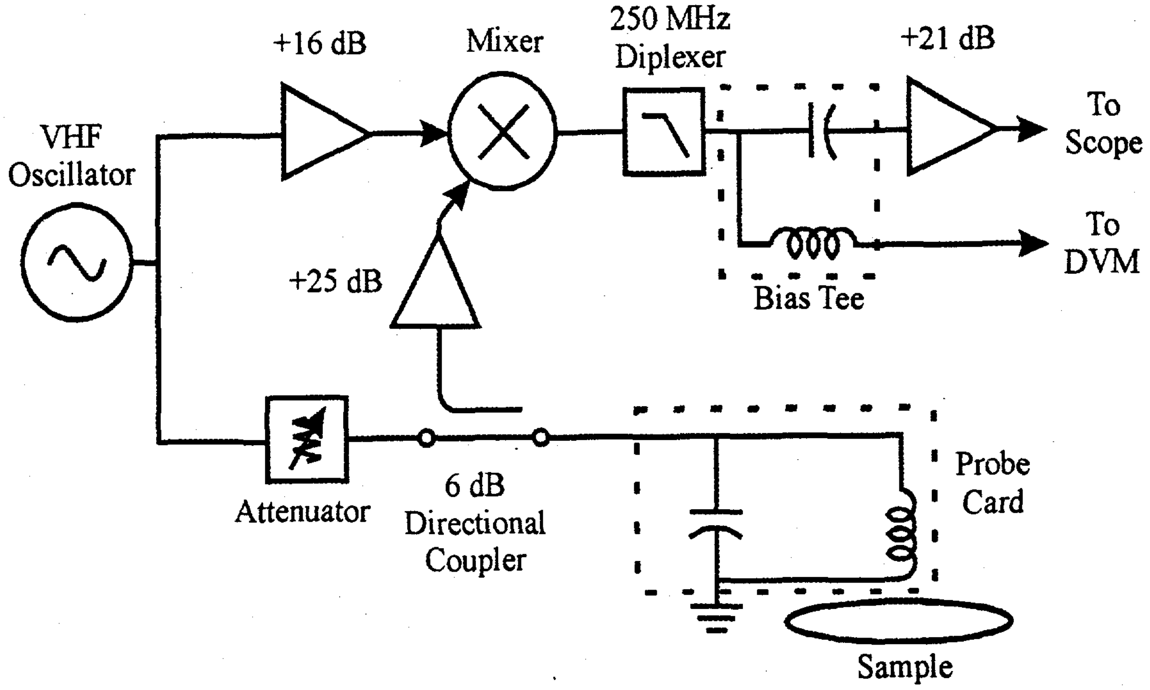

FIGURE 3.1 RF Photoreflectance System Schematic

Radio Co. 3200A VHF oscillator provides a continuous-wave (CW) signal set to 410 MHz at up to 170 mV_{rms} signal voltage or 0.58 mW (-2.4 dBm) into a 50 Ω load. The signal is split with a coaxial Tee and fed to a Minicircuits ZHL-1A, 2-500 MHz, 16 dB amplifier for use as the local oscillator (LO) and a variable attenuator to serve as the RF signal. The purpose of the attenuator is to provide isolation to the local oscillator from changes in loading due to the reflected signal. The 16 dB amplifier is needed to achieve a minimum of 20 mW (13 dBm) power on the local oscillator input of the Minicircuits ZAY-2, 10-1000 MHz, double-balanced mixer required for the specified minimum conversion loss of 6.9 dB.

After the attenuator in the signal path, the signal is sent to the probe card through a directional coupler that is used to direct the reflected signal into the Hewlett-Packard HP84470, 0.1-1300 MHz, 25 dB amplifier. This amplifier is necessary to offset the 6 dB loss the signal experiences through each pass of the coupler (a total loss of 12 dB).

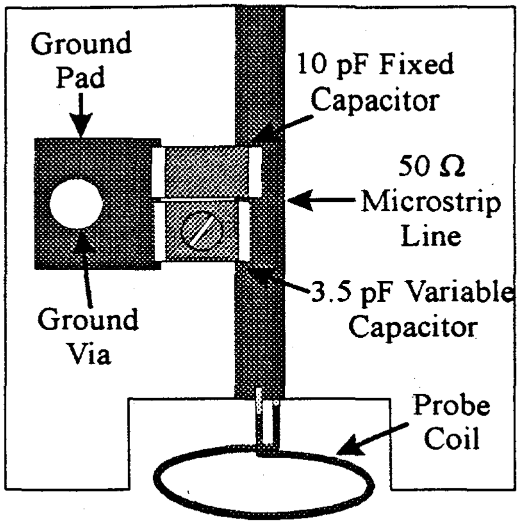

FIGURE 3.2 Front Side of Probe Card

The probe card consists of a parallel-connected capacitor and coil (inductor) mounted on a 0.02 inch thick Duroid microwave substrate with 50 Ω microstrip transmission lines. This material has a low loss-tangent and a dielectric constant (ε_r) of 2.2. The front side of the probe card is shown in Figure 3.2 and the back side is a solid copper ground plane with a copper via connecting the front side ground pad to the back side ground plane. The probe card is mounted in the system with a coaxial launcher in which the center conductor of the coaxial connector contacts the microstrip line and the outer conductor contacts the ground plane on the back of the card. With the 3.5 pF variable capacitor included in the circuit, the unloaded resonance of the card can be adjusted from 360 to 410 MHz.

The probe coil is made from 18 AWG (0.07 inch diameter) enamel-coated wire typical of that used in winding RF inductors. The coil is wound around a 4 mm diameter form having a circular cross-section. When the coil is in the vicinity of a sample, eddy currents are induced in the sample with the sheet resistance of the sample impeding its flow. Taken together, a transformer is formed with the coil as the primary, the eddy currents as the secondary, and the sheet resistance as a load in the secondary. Although 2-, 3-, and 5-turn coils and larger diameter coils have been fabricated, a 4 mm 1-turn planar coil is used to obtain a maximum coupling of the RF signal to the photogenerated carriers in the sample and because the lower inductance and parasitic capacitance allows the circuit to resonate at 410 MHz with the capacitor values given above.

The amplified signal (≤ 1.4 mW or 1.4 dBm) reflected from the probe card is fed to the RF input of the mixer for frequency mixing with the 24 mW (13.8 dBm) signal at the LO port. Since both signals are at the same frequency, the output of the mixer is ideally given by

$$V_{IF} = \alpha V_{RF}\left(\cos\varphi - \cos(2\omega t + \varphi)\right) \tag{3.1}$$

where V_{RF} is the magnitude of the signal at the RF port, ω is the angular frequency, φ is the phase difference between the signals at the LO and RF port, and α is the conversion loss factor, which for this mixer at 410 MHz is 6.9 dB or 0.45. If all of the signal is reflected from the probe card and arrives at the RF port in phase with the LO signal, there should be a DC voltage of 186 mV and a 168 mV_p (0.28 mW or -5.5 dBm) signal at 820 MHz at the IF port.

Since the useful information (i.e., the magnitude and phase of the reflected signal) is present in the DC part of the signal, a 250 MHz diplexer is used to filter the 820 MHz signal. The diplexer consists of a low input impedance 5th-order 1 dB ripple Chebyshev 250 MHz low-pass and high-pass filter connected to the input via a 3 dB splitter as shown schematically in Figure 3.3. Since Chebyshev filters are very sensitive to component values, variable capacitors were placed in both sections to achieve the values of the most critical

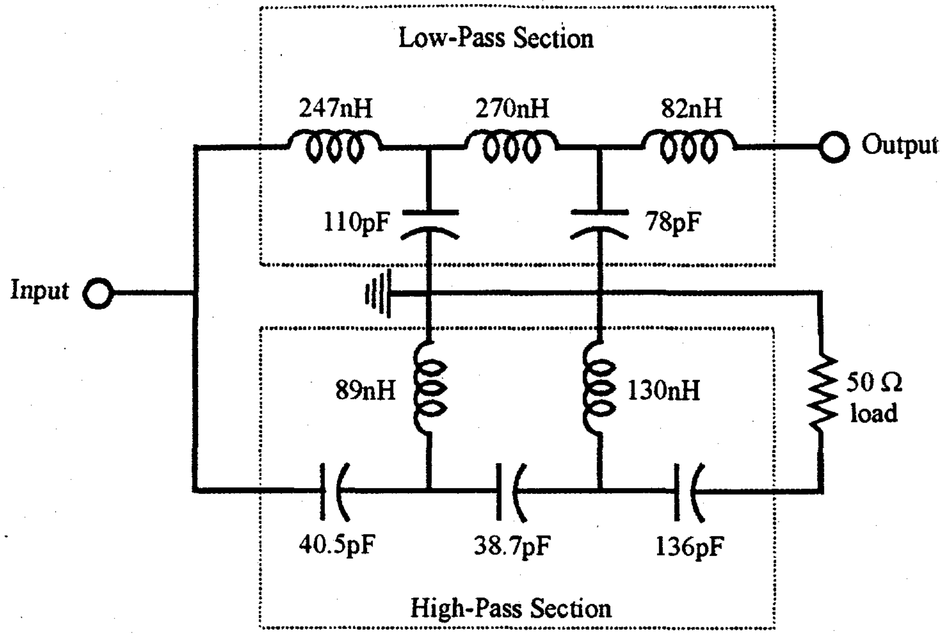

FIGURE 3.3 Schematic of 250 MHz Diplexer

capacitors and provide an optimum match to the ideal transfer function and reflection coefficient shown in Figure 3.4. The diplexer is designed to pass the signals below 250 MHz, providing a response time of 4 ns, with minimum attenuation through the low-pass section while diverting higher frequencies through the high-pass section into a 50 Ω dummy load. Therefore, reflection is minimized for all signals from the input which would mix with other signals in the mixer and distort the final signal. To minimize losses, the diplexer is fabricated on Duroid microwave substrate with microstrip transmission lines as shown in Figure 3.5, mounted on a brass block, and connected to the system with coaxial launchers.

Under unilluminated conditions, the output of the diplexer is a DC voltage. However, when illuminated by a short pulse of light, the output consists of the DC voltage with a decay transient that corresponds to the decay of photogenerated carriers. In order to amplify the transient, a bias Tee is used to divert the DC voltage into a 50 Ω terminated voltmeter, while passing the relatively small transient into the Minicircuits ZHL-6A 2.5 KHz-500MHz 21 dB amplifier. This amplifier was selected because of the low-frequency coverage necessary to accurately measure decay times > 1 μs. Signals from the mixer in the frequency range of 2.5 KHz through 250 MHz are amplified to yield a maximum output signal of 1.88 V_p (35.5 mW or 15.5 dBm).

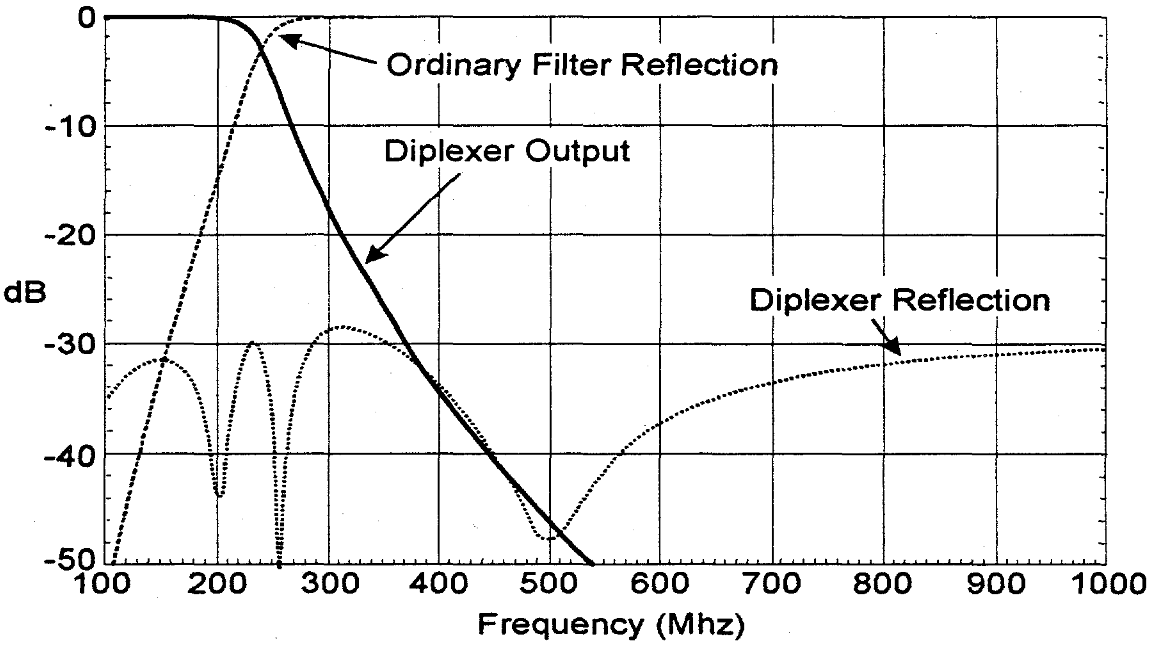

FIGURE 3.4 Simulated Response of Diplexer Compared to Low-pass Filter

The output of the 21 dB amplifier is fed to the 50 Ω terminated input of a Hewlett-Packard HP54616C, 2 GSa/s, 500 MHz bandwidth, 8-bit digital storage oscilloscope. The most sensitive scale of this unit is 2 mV/div with a resolution of 0.08 mV that establishes the lower limit on measurable signal amplitude to practically 0.8 mV. However, due to electronic noise generated within the components and from external sources (~1 mV), the minimum signal amplitude from which a decay is measurable is 3 mV. Thus, the dynamic range of the system is 56 dB.

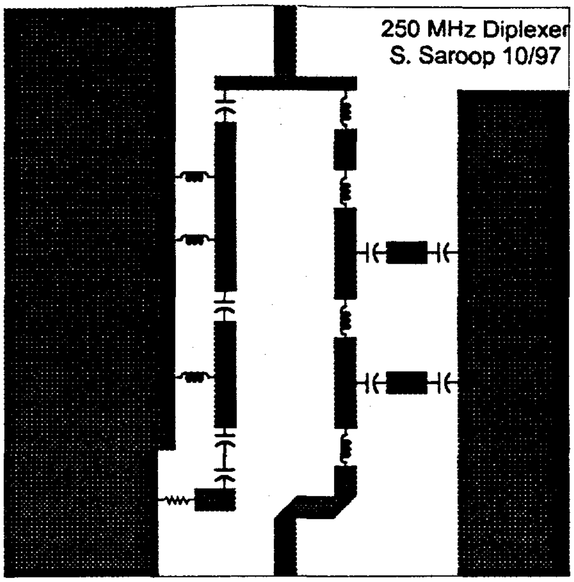

FIGURE 3.5 Diplexer Front Side Pattern

3.3. Laser Selection

In measuring recombination lifetimes by photogeneration techniques, a pulse of light with an optical decay time less than the lowest desired recombination lifetime is required. In addition, since the absorption constant is a function of wavelength, a monochromatic source of light with a wavelength such that near-complete optical absorption occurs in the active layer of the material being investigated should be employed. Therefore, the thickness of the material sets an upper limit on the wavelength and is very close to the bandgap photon wavelength. The lower limit is determined by the condition of the sample surface and the system sensitivity. Since shorter wavelengths are absorbed closer to the surface, poor surfaces yield low values of surface lifetimes. Thus, the result is less total photogenerated carriers at the end of the optical pulse, and lower signal amplitudes.

The light source employed in the photoreflectance system is a Laser Photonics YQL-102+ Q-switched Nd:YAG laser with a fundamental wavelength of 1064 nm and up to 200 mJ per pulse at a repetition rate of 20 Hz and a beam diameter of 6 mm. Additional frequency-doubling and quadrupling crystals may be added or removed to give 532 nm pulses at up to 100 mJ/pulse or 266 nm pulses at up to 30 mJ/pulse. The laser output power is continuously variable through a built-in pair of rotating polarizers that can achieve attenuation ratios of 40:1 for 1064 nm and 532 nm, and 80:1 for 266 nm.

The temporal shape of the pulses was measured using an Electro-Optics Technology ET-3000 InGaAs photovoltaic detector with a response time of under 200 ps for visible and IR energy, and an ET-2020 Si PIN diode detector for UV energy with a response time of 1.5 ns. Figure 3.6 shows the detector signal measured at the fundamental wavelength. The exponential risetimes, decay times, and full-width half-maxima (FWHM) are given in Table 3.1 for each wavelength measured at both the laser output and the fiber output.

The pulse energy was measured with Scientech P05 and SP25 pyroelectric detectors. The P05 has a 5 mm aperture, a noise-equivalent power of 3 nJ, and is a very sensitive detector to 200 nm through 10 μm radiation; however, the maximum pulse energy is limited

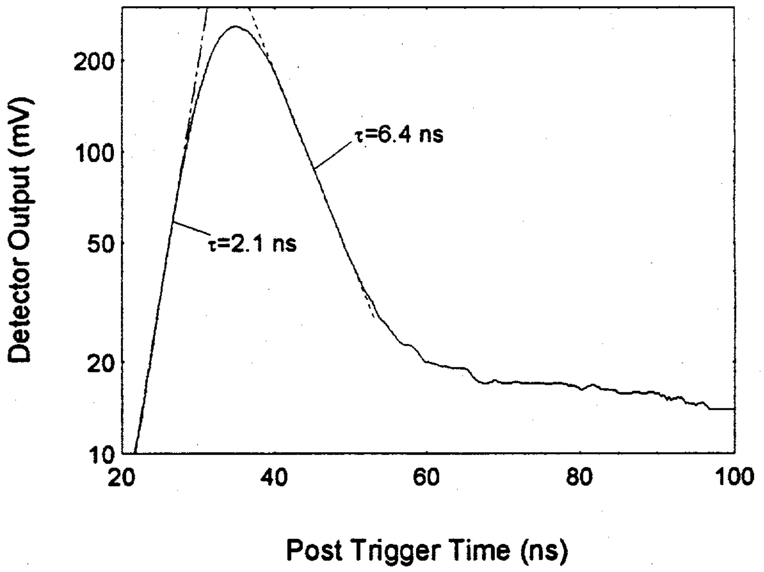

FIGURE 3.6 1064 nm Optical Pulse Shape

Table 3.1 Measured Optical Pulse Characteristics

Wavelength (nm)	Risetime (ns)		Decay Time (ns)		FWHM (ns)	
	Laser	Fiber	Laser	Fiber	Laser	Fiber
1064	2	4	6	7	13	11
532	2	2	5	5	10	11
266	2	3	5	8	13	13

to 1.5 mJ in 10 ns. The SP25 is a 25 mm detector with the same spectral sensitivity, but has a higher noise floor that limits energy measurement from 0.21 mJ up to 8.5 mJ (due to a damage threshold of 30 mJ/cm^2 with a 6 mm beam diameter). In order to measure higher pulse energies, a pair of quartz slides were used as beam splitters. The reflection coefficients of the pair at each wavelength were measured to be 0.0076 at 1.06 μm, 0.0030 at 532 nm, and 0.0059 at 266 nm (at <8 mJ pulse energy). The values were then used to scale the energy read by the sensitive P05 detector to obtain real-time power readings during the RF photoreflectance measurement process. By this method, the laser has demonstrated better than 3% stability in energy, compatible with the manufacturer's specifications.

The upper limit of pulse energy is due to the damage threshold of the fiber optic cable and its loss. The damage threshold of the 600 μm diameter silica fiber being used (for 1064 nm and 532 nm operation) was empirically determined to be 6.2 mJ at 1064 nm, as measured from the output of a manually cleaved and polished fiber and is the maximum energy that can be delivered to a sample. This measurement was obtained with an optimum coupling to the fiber of 0.3. The coupling can be continuously decreased to ~0.003 by increasing the distance of the input of the fiber from the focal plane of the coupling lens, and is limited only by the length of the coupler.

3.4. Calibration

The response of the RF subsystem to sample conductivity is calibrated using five VLSI© Si resistivity standard wafers having calibrated resistivities (ρ) of 0.00173, 0.0105, 0.0296, 0.103, and 0.320 Ω-cm. At 410 MHz, using $\delta = \sqrt{2/\omega \mu_0 \sigma}$ for the skin depth, where μ_0 is the sample permeability and σ is the conductivity (=1/ρ), the sheet resistances (R_S) of these standards are 0.168, 0.412, 0.692, 2.12, and 6.27 Ω/□, respectively. For the two highest resistivity samples, the skin depth is greater than the thickness (500 μm), yielding thickness-limited values for R_S. A half-inch thick brass block serves as a final calibration standard with a skin depth-limited sheet resistance of 0.010 Ω/□ at 410 MHz.

First, the reflection coefficient of the probe card with the various standards against the probe coil is measured with a Hewlett-Packard HP8510C Network Analyzer, which has the capability of measuring the S-parameters of either one- or two-port networks from 45 MHz to 40 GHz. The enamel coating of the probe coil wire provides electrical isolation from the floating samples. The network analyzer is calibrated using factory calibrated opens, shorts, and 50 Ω terminations to a reference plane located at the coaxial connector. The effect of the launcher of the probe card is nulled by the application of an electrical length offset. The reflection coefficient (Γ) was measured from 50-1000 MHz in 2.375 MHz increments; the values measured at 410 MHz are presented in Table 3.2 along with the DC voltage measured with the sample against the probe card in the RF photoreflectance system.

The DC voltage was measured using a 50 Ω terminated Hewlett-Packard Digital Voltmeter at the bias Tee with the probe card installed in the photoreflectance system and each standard placed against the coil in dark conditions. A phase offset between the LO and

Table 3.2. Reflection Coefficients of Standards Measured with Baseline Probe Card at 410 MHz

Sample	Sheet Resistance ($\Omega/\square$)	$\lvert\Gamma\rvert$	$\angle\Gamma$ degrees	V_{DC} (mV)
Brass	0.0102	0.912	74.7	-61.5
R002	0.168	0.768	67.1	-11.6
R01	0.412	0.685	48.9	33.4
R03	0.692	0.627	38.4	53.6
R1	2.12	0.622	11.9	92.3
R3	6.27	0.754	-1.89	124.5
Air	377	0.918	-1.65	145

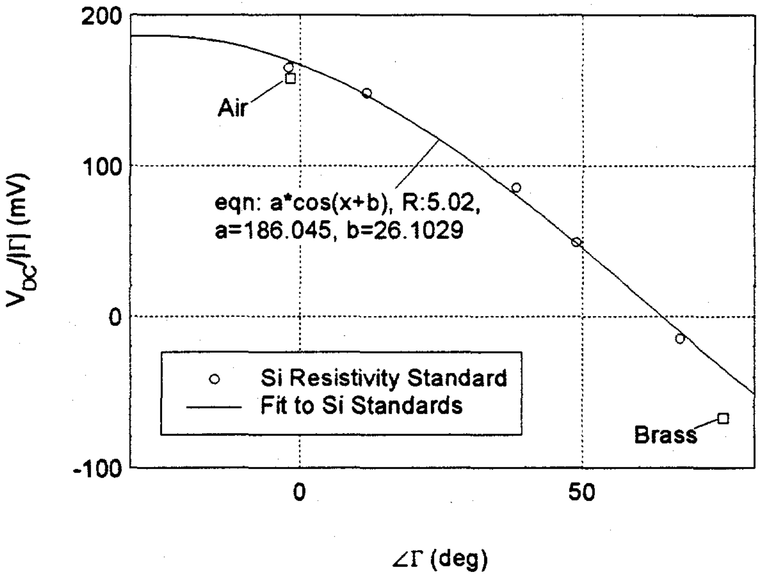

FIGURE 3.7 Normalized DC Voltage vs. Phase Angle

RF signals arriving at the mixer arises due to differences in cable lengths. This phase offset is in addition to the phase shifts ($\angle\Gamma$) measured at the probe card in Table 3.2. The DC voltage is given by $|\Gamma|\cos\phi_{tot}$, where ϕ_{tot} is the total phase shift. Therefore, by normalizing the DC voltage with $|\Gamma|$ and plotting versus the phase angle measured at the probe card, as in Figure 3.7, it is possible to determine the phase offset by fitting to $\cos(\phi+\phi_{offset})$. The five Si resistivity standards, having the same permittivity, fit a cosine curve well. However, the values for air and brass deviate slightly from the curve. From the fit, the phase offset is 26.1° at 410MHz. The amplitude of the cosine fit, 186 mV, agrees perfectly with the calculated maximum signal amplitude present at the output of the mixer.

The Γ as a function of frequency measured with the brass sample was used to calculate model parameters for the probe card with Z_L proportional to $1+j$ using the optimization routines in Optotek Ltd.'s MMICAD for Windows 1.10, yielding the circuit in Figure 3.8. The model contains stray capacitances and frequency dependent parasitic resistances ($\propto f^{1/2}$) as well as coupling effects for the coil, where k is the coupling coefficient representing the degree of the magnetic coupling to the sample. Using the circuit element values obtained from fitting to the brass sample, the fitting of the measured Γ of the

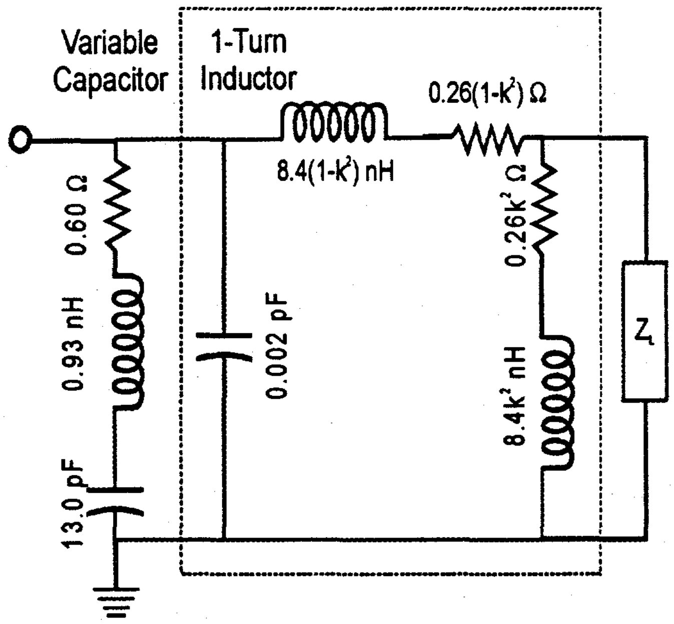

FIGURE 3.8 Probe Card Circuit Model (Element Values Obtained with Brass Sample)

remaining standards results in values of ρ_L (Z_L) and k.

The results of the fitting are shown in Table 3.3 and Figure 3.9. The coupling coefficient is approximately 0.7, while ρ_L increases approximately linearly with the sample resistivity with an impedance transformation of ~4.43 for each sample excluding the highest resistivity sample. This indicates that the RF probe responds linearly for samples with sheet resistances as low as 0.01 Ω/□, which corresponds to carrier concentrations as high as 8.9×10^{20} cm^{-3} with a mobility of 1000 $\mathrm{cm}^2/\mathrm{V}\cdot\mathrm{s}$ in a 7 μm active layer or 1.3×10^{19} cm^{-3} (or 6.3×10^{17} cm^{-2}) in a 500 μm-thick substrate. The upper range of the RF probe and system linearity is at least 2.1 Ω/□, corresponding to a carrier concentration of 4.3×10^{18} cm^{-3} for such an active layer or 6.0×10^{16} cm^{-3} (or 3.0×10^{15} cm^{-2}) for a 500 μm-thick substrate. Using a probe coil with a greater number of turns results in a different dynamic range, impedance transformation, and coupling coefficient.

Table 3.3 Calculated Resistivity and Impedance of Standards at 410 MHz

Sample	Resistivity (Ω-cm)	RF Skin Depth δ(μm)	Sheet Resistance (Ω/□)	Model Z_L (Ω)	ρ_L=Re(Z_L× δ) (Ω-cm)	k
Brass	6.40×10^{-6}	6.27	0.0102	0.120(1+j)	7.51×10^{-5}	0.712
R002	0.00173	103	0.168	1.29(1+j)	1.33×10^{-2}	0.693
R01	0.0105	255	0.412	2.55(1+j)	6.26×10^{-2}	0.664
R03	0.0296	427	0.692	4.45(1+j)	0.190	0.670
R1	0.103	487*	2.12	12.5(1+j)	0.608	0.702
R3	0.320	510*	6.27	2.84(1+j)	0.145	0.483

* Sample-thickness limited

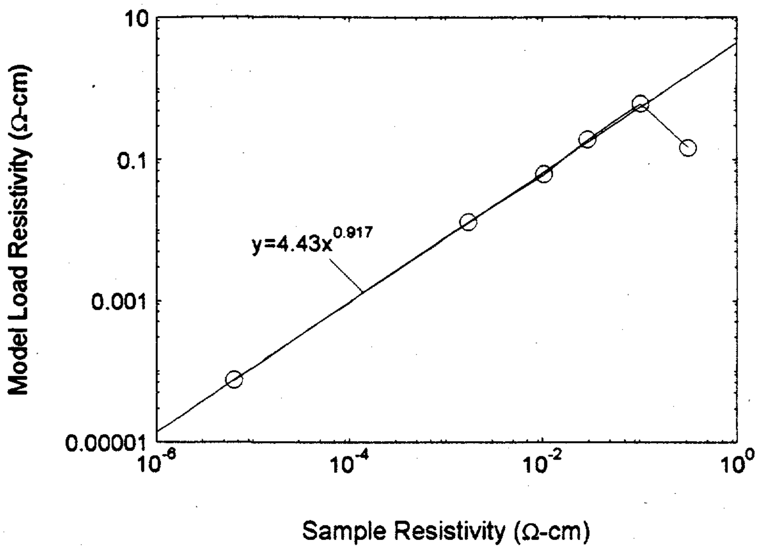

FIGURE 3.9 Load Impedance of Resistivity Standards from Fit to RF Probe Card Model

3.5. Transient Response

Under illumination by a pulsed laser, a transient signal is observed on the oscilloscope. After averaging over a sufficient number of pulses to maximize the signal to noise ratio, the signal is digitized and sent to a computer via the General Purpose Interface Bus (GPIB) for analysis. Plotting the transient response on a log scale allows the decay time of this signal to be readily extracted, as depicted in Figure 3.10. Superimposed on the transient are least-squares fit lines along with their respective exponential decay times. These fit lines give the initial decay time and long decay time, as well as any additional decays observed. Also of importance is the long decay amplitude, defined as a percentage of the pulse height when the long decay is extrapolated to the peak position. Repeatability measurements show that decay times can be measured with a ±0.9 ns uncertainty. However, for signals close to the noise limit (3 mV), the measured uncertainty increases to ±3.6 ns.

The long decay response is calibrated using a bulk GaSb sample because the large pulse height and long decay amplitude provides many orders of magnitude over which the

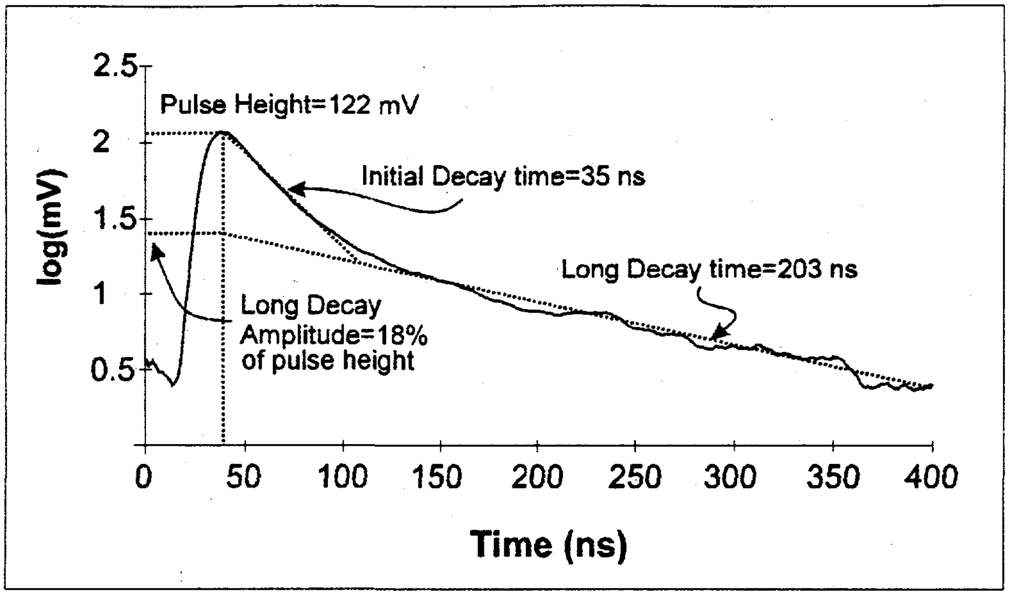

FIGURE 3.10. Typical RF Photoreflectance Decay Transient

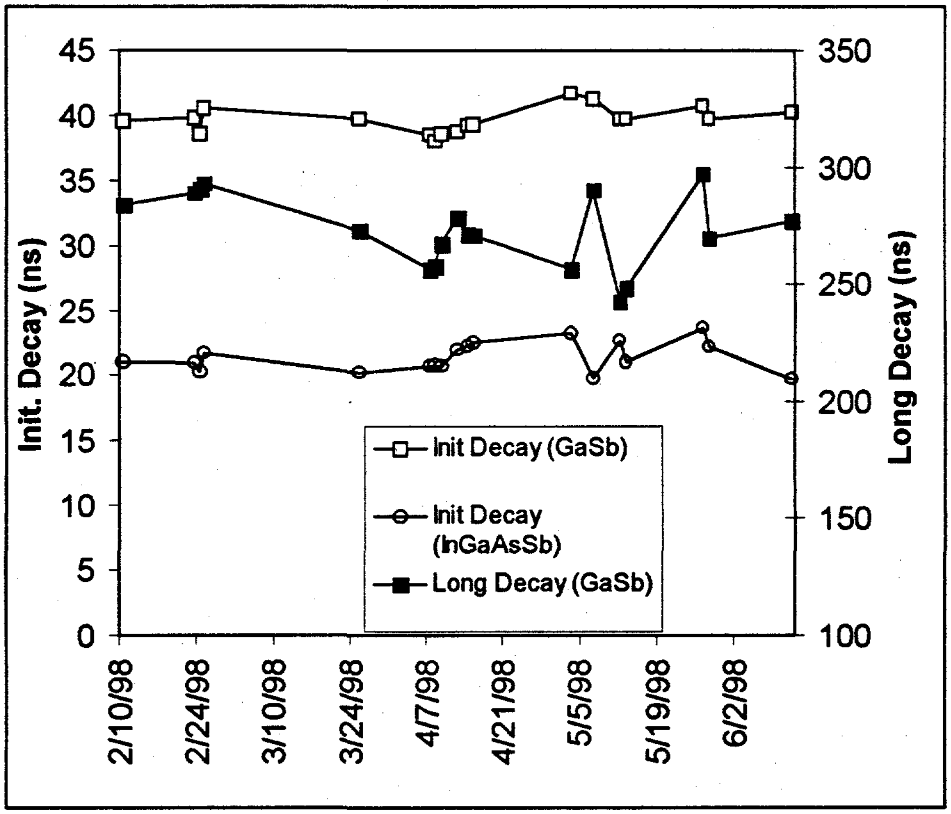

FIGURE 3.11. RF Photoreflectance Calibration with GaSb and InGaAsSb

long decay can be fit. The short decay response is calibrated with an AlGaAsSb capped InGaAsSb TPV structure (97-548) because the low long decay amplitude permits accurate measurement of the initial decay. The initial decay for both samples and the long decay for the GaSb sample are shown in Figure 3.11. Over the course of 5 months, the decay times fell within ±10% of the mean value, indicating excellent system stability.

Measurements on undoped and low doped ($p=1.5\times10^{16}$ cm^{-3}) 0.73 eV InGaAs on InP samples yield long decay times of 290 and 330 ns, respectively. Both samples show SRH behavior with initial decays of 100 ns at full laser intensity, decreasing to 20 ns at 8% intensity. This data was recently confirmed by Ahrenkiel *et al.*[53], with lifetime measurements taken on similar samples as a function of doping. At this doping level, the reported lifetime was on the order of 300 ns, and SRH recombination was found to dominate. This external comparison, while not an absolute calibration, provides a good verification of the present setup.

3.6. System Transient Capability

The measured decay times are a function of the carrier recombination rate, the laser pulse decay time, and the RF system response time. From Table 3.1, the risetime and decay time of the laser are 4 and 7 ns, respectively, at 1064 nm as measured from the output of the fiber. The RF system response time is determined primarily from the 5th order diplexer with a 250 MHz cutoff frequency.

The laser pulse ($p(t)$) is modeled empirically with an equation which, when plotted on a log-scale, has asymptotes determined by the laser pulse rise and decay times as follows:

$$p(t) = Ae^{-a\sqrt{1+\left(\frac{t-m}{b}\right)^2}+\frac{t-m}{c}} \tag{3.2}$$

where a, b, and c are fitting parameters that give the required pulse shape, and m is the time at which the pulse peak occurs after the trigger set on the oscilloscope. The value of A is obtained by integrating over time and setting the result to the number of photons per pulse. Fitting the above equation to the measured optical pulse shape (Figure 3.6) at 1 mJ/pulse (5.36×10^{15} photons/pulse), the values of 0.393, 2 ns, 18.7 ns, 20.6 ns, and 5.51×10^{23} are obtained for a, b, c, m, and A, respectively.

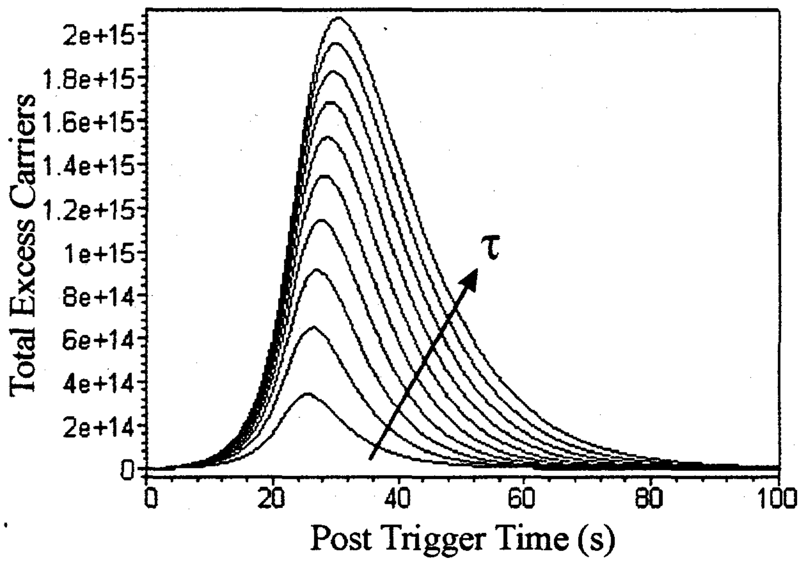

FIGURE 3.12 Simulated RF Photoresponse for Samples with Lifetime τ=1, 2, 3, 4, 5, 6, 7, 8, 9, and 10 ns

The response of the diplexer ($H(s)$) can be modeled as a 5th order low-pass filter to a first order approximation, i.e., $H(s)=1/(1+s/\omega_0)^5$ where $\omega_0=2\pi\times250\times10^6$ rad/s, which dominates the transient response of the RF circuitry. Therefore, the response of the RF photoreflectance system can be simulated for samples with various lifetimes by taking the inverse Laplace transform of the product of the transfer functions of the optical pulse, the filter, and an exponential with decay time equal to the sample lifetime as shown in Figure 3.12. As expected, the greater the sample lifetime, the greater the number of total carriers generated, which demonstrates that the pulse height can be used qualitatively as a measure of the sample lifetime.

The peak of the RF photoreflectance transient is delayed by an increasing amount as the bulk lifetime increases. The time difference (t_d) between the RF transient peak and the optical pulse peak is shown in Figure 3.13 for bulk lifetimes from 1 to 50 ns. Superimposed on the figure is a fit of a cubic root ($4.57x^{1/3}$) to the delay times that can be used to approximate the time delay of the RF transient peak to within 1 ns. Knowledge of the delay is necessary in extracting instantaneous decay times of the non-exponential simulated decay transients.

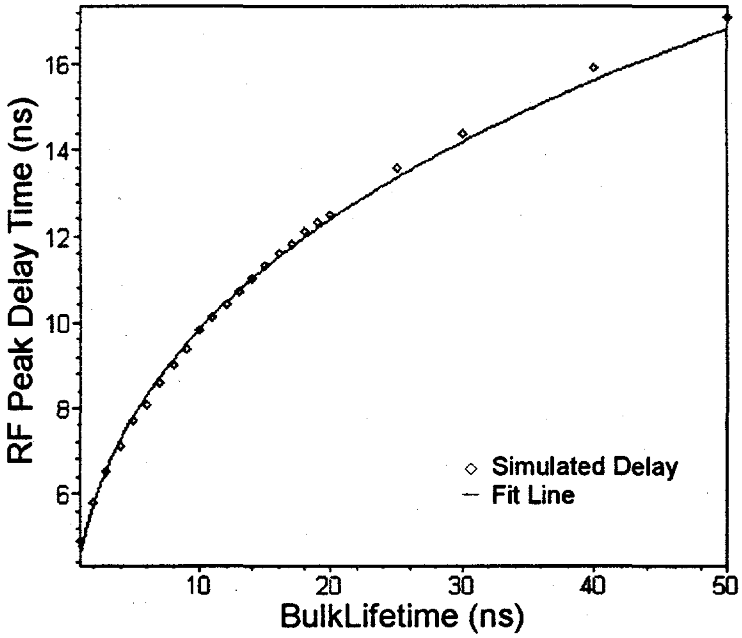

FIGURE 3.13 Simulated Delay of RF Photoreflectance Transient Peak Time Following Optical Pulse Peak

Measuring the inverse of the slope of the photoresponse curves on a log scale gives an instantaneous decay time that can be compared to the sample lifetime. The decay times measured at a time when the transient becomes exponential (>$2t_d$) are greater than the sample lifetime as a result of the finite optical pulse decay time and system response time. The difference between the two values are shown in Figure 3.14, and shows that lifetimes as low as 12 ns can be measured to an accuracy within 1 ns.

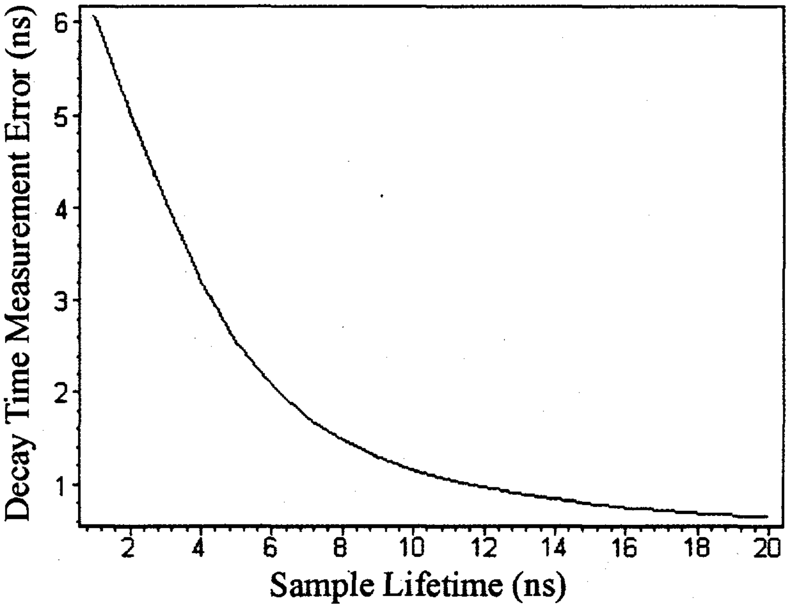

FIGURE 3.14 Simulated RF Photoreflectance Measurement Error

3.7. Summary

The active layer in TPV devices is generally composed of a III-V semiconductor having a bandgap < 1 eV. Such samples tend to have low sheet resistances due to the higher intrinsic carrier concentration and the presence of native defects compared to wider bandgap materials. The RF photoreflectance system is capable of measuring decay times in high conductivity samples and complements the capability of the microwave reflectance system discussed in section 2.4.1. The capabilities of the RF photoreflectance system are summarized in Table 3.4.

Table 3.4 RF Photoreflectance System Parameters

Parameter		Range
Operating RF Frequency		377 to 410 MHz
Optical Wavelength		266, 532, or 1064 nm
Optical Pulse Energy	1064 nm	390 nJ to 6.2 mJ
	532 nm	1 μJ to 6.2 mJ
	266 nm	510 nJ to 510 μJ
Pulse Amplitude Dynamic Range		3 mV to 1.88 V
Measurable Decay Time		12 ns to 4 ms
Decay Time Repeatability		±10%
Spatial Resolution		4 mm
Sample Sheet Resistance (@ 410 MHz)		0.1 to >2.1 Ω/□
Detectable Range of Injection Levels (in GaSb with p_0=2×10^{16} cm^{-3}=10^{15} cm^{-2})		5×10^{13} - 7×10^{16} cm^{-2}

The excitation levels obtainable with the system are determined by the pulse energy and wavelength, the spot-size of the beam on the sample, and the sample reflectivity at the given wavelength. For example, using a reflectivity (R) of 0.38 in GaSb[72] at 1064 nm, a 1 mJ pulse containing 5.36×10^{15} photons/pulse results in 3.32×10^{15} pairs of carriers generated per pulse, assuming all photons absorbed result in an electron-hole pair. The diameter of the approximately circular beam incident on the sample was measured to be 6 mm using a phosphor-coated IR detector, resulting in $1.90(1-R)\times10^{16}$ *e-h* pairs/cm^2.

The injection level can be determined from knowledge of the sample sheet resistance and the dependence of DC voltage on sample sheet resistance from Table 3.2. For example, the DC voltage from the commercial 500 μm-thick p-type GaSb substrate of 120 mV gives a sample sheet resistance of 6 Ω/□, corresponding to an equilibrium carrier concentration of 2.1×10^{16} cm^{-3} or 1.1×10^{15} cm^{-2} assuming a mobility of 1000 cm^2/V·s. The pulse amplitude of 600 mV measured with a 1 mJ pulse must be divided by the 21 dB gain of the final amplifier, thus giving a voltage drop of 53 mV that corresponds to a transient sheet resistance of 1.2 Ω/□. The transient sheet resistance is due to the background doping and the excess carrier concentration as a function of depth, which is assumed to decay exponentially from the surface. The integrated carrier concentration is then given by

$$N = \int_0^W (n_0 + \alpha N_{ph} e^{-\alpha x})dx \xrightarrow[W>>\alpha]{} n_0 W + N_{ph} \tag{3.3}$$

where α is the absorption constant, W is the sample thickness, n_0 is the equilibrium carrier concentration, and N_{ph} is the density of photons absorbed per cm^2. The transient sheet resistance is then $1/q\mu(n_0W+N_{ph})$, giving 4.3×10^{15} photons/cm^2 absorbed. This corresponds to a pulse energy of 0.36 mJ, which is within a factor of three from that measured optically. The discrepancy is most likely due to the value assumed for the sample mobility.

In thin active layers with good surface passivation the carriers redistribute themselves before the optical pulse peaks, and the carrier concentration can be assumed to be uniform. Thus, for an active layer 2 μm thick with an effective lifetime much longer than the duration of the optical pulse, the photogenerated carrier concentration is $9.5(1-R)\times10^{19}$ cm^{-3} per mJ. For samples with lower lifetimes, the peak carrier concentration per mJ pulse energy can be obtained from Figure 3.12 normalized to the volume of generation.

The RF photoreflectance system discussed in this chapter demonstrated good repeatability and nearly 3 orders of magnitude dynamic range that should improve with more effective RF shielding and use of low-noise amplifiers. Since the system is based on a homodyne detector, care must be taken to null the effect of the different path lengths the signal sees prior to detection, which generally change with operating frequency unless cable lengths and velocity factors are matched precisely. Since sample lifetime generally varies with injection level, stable laser optical power is essential. The use of beam splitters permits monitoring of power levels throughout the measurement process, but the low reflection coefficients limit minimum detectable power to ~1 μJ at the output of the fiber. The beam splitters must be cleaned regularly (~2× per month) to maintain the reproducibility quoted. Finally, utilizing mechanically cleaved and polished fibers should permit near ideal coupling, limited only by the reflection coefficient of the fiber, and a wider range of injection levels.

4. Separation of Bulk and Surface Effects in Epitaxial Layers

In thin epitaxial samples, the decay transient is influenced by surface recombination at both the front surface and the back interface to underlying layers. If these surfaces have different properties (i.e., different surface recombination velocities), separation of the effects of each surface is generally not possible with the RF photoreflection technique. One strategy to characterize an interface is to have the same interface on both sides of an active layer. This doubly-capped structure allows the determination of the surface recombination velocity (SRV) and the bulk lifetime of the active layer. In this chapter, the analysis of doubly-capped structures is presented along with measurements of such structures grown with InGaAsSb active layers. Surface recombination velocities are obtained and the dominant bulk recombination mechanisms are explored.

4.1. Analysis of Doubly-Capped Test Structures

Analysis of the decay transient was accomplished by solving the transient diffusion equation for a uniform distribution of bulk recombination centers assuming an impulse excitation. This assumption is valid for times greater than the laser pulse decay time. The boundary conditions for the solution are then a Beer's law distribution for the excess carriers at t=0, and surface recombination velocities of S_1 and S_2 at the front and back surfaces. For p-type material, the excess electron concentration obeys the relations:

$$\frac{\partial n}{\partial t} = -\frac{n}{\tau_B} + D_n \frac{\partial^2 n}{\partial x^2}, \quad n(x,0) = \alpha N_{ph} e^{-\alpha x}$$
$$\text{and} \quad D_n \left.\frac{\partial n}{\partial x}\right|_{x=0} = S_1 n, \quad D_n \left.\frac{\partial n}{\partial x}\right|_{x=W} = -S_2 n \quad . \tag{4.1}$$

The preceding equations can be solved[54] by separation of variables and results in the solution:

$$n(x,t) = e^{-t/\tau_B} \sum_i A_i e^{-k_i^2 D_n t} \left(\cos k_i x + \frac{S_1}{D_n k_i} \sin k_i x \right) \quad ,$$
$$\text{where} \quad A_i = \frac{\int_0^W n(x,0) \left(\cos k_i x + \frac{S_1}{D_n k_i} \sin k_i x \right) dx}{\int_0^W \left(\cos k_i x + \frac{S_1}{D_n k_i} \sin k_i x \right) dx} \quad , \tag{4.2}$$

D_n is the electron diffusion constant, and W is the thickness of the active area. The k_i's are obtained by solving

$$\tan k_i W = \frac{k_i W \frac{S_1 + S_2}{D_n / W}}{\left(k_i W\right)^2 - \frac{S_1 S_2}{\left(D_n / W\right)^2}} \quad . \tag{4.3}$$

The transcendental equation must be solved numerically to give the eigenvalues k_i. This solution represents a series of exponentials of amplitude A_i, with decay times given by:

$$\frac{1}{\tau_i} = \frac{1}{\tau_B} + k_i^2 D_n \quad . \tag{4.4}$$

For very poor ($S >> D_n/W$) or very good ($S << D_n/W$) surfaces, the sum reduces to a single exponential with an effective decay time as:

$$\frac{1}{\tau_{eff}} = \begin{cases} \dfrac{1}{\tau_B} + \dfrac{S_1 + S_2}{W} & for\ S_1\ and\ S_2 << \dfrac{D_n}{W} \\ \dfrac{1}{\tau_B} + \dfrac{\pi^2 D_n}{W^2} & for\ S_1\ or\ S_2 >> \dfrac{D_n}{W} \end{cases} \tag{4.5}$$

Thus, for low SRV values the effective decay time depends on both the bulk lifetime and the sum of the SRV at each surface. For very high SRV values the effective decay time depends only on the bulk lifetime. When one or both of the surfaces have a large S the excess carriers recombine at the surface on the order of the time required for carriers to diffuse across W, if the diffusion length ($L_n = \sqrt{D_n \tau_B}$) is long. If $W >> L_n$, the carriers recombine by bulk recombination (e.g., at SRH centers) before reaching the surface. However, when both surfaces have low SRVs, as in the case of the double heterostructure confinement layers, the sum of the SRVs can be separated from the bulk lifetime using samples of different W. By plotting $1/\tau_{eff}$ versus $1/W$, the sum of the SRVs can be extracted from the slope and the bulk lifetime from the extrapolated y-intercept. In the case of the doubly-capped structure, the slope is given by $2S/W$. Although not considered in this thesis, it is worthwhile to note that with sufficiently thick active layers and a pair of optical wavelengths, (one of which satisfies $\alpha W<<1$), the SRV at both interfaces can be determined.

For high quality p-type epilayers, $D_n \approx 78$ cm^2/s and for practical device structures 3 μm$\leq W \leq$10 μm, so that D_n/W$\sim 10^5$ cm/s. Therefore, in order for this technique to be useful, interfaces with SRV$\leq 10^4$ cm/s are required to accurately extract the SRV.

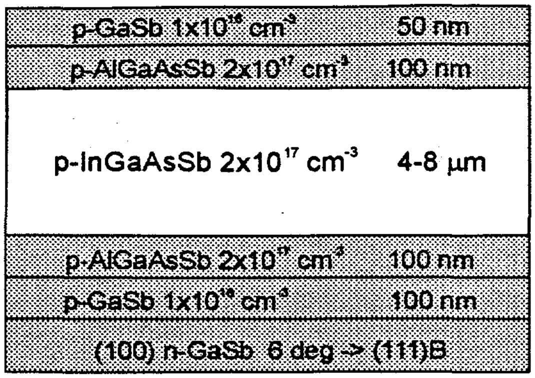

FIGURE 4.1a. Cross-section of AlGaAsSb Capping Layer Structure

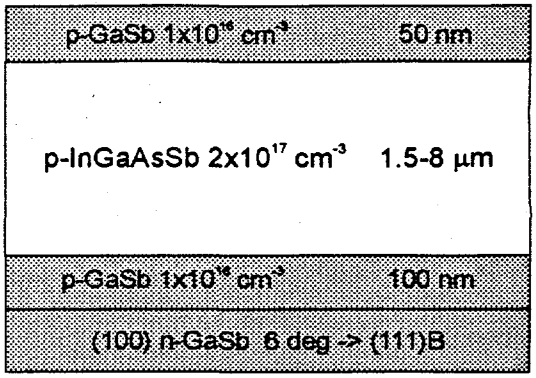

FIGURE 4.1b. Cross-section of GaSb Capping Layer Structure

4.2. Measurements of Surface Recombination Velocity

Lattice-matched structures were grown with the thickness of the Zn-doped p-type InGaAsSb active layer varied as indicated in Figures 4.1a and 4.1b. This 0.55 eV layer is capped on the front and back surfaces with undoped AlGaAsSb layers (Figure 4.1a) having a bandgap of about 1 eV. An undoped GaSb layer is grown on the front surface to prevent oxidation of the high-Al content cap. The GaSb capping structures (Figure 4.1b) are easier to accommodate in the OMVPE reactor[64] and give comparable TPV device performance[7]. The resulting heterostructures provide retarding fields for the minority carriers (electrons) at both surfaces, thus significantly reducing the effect of interface recombination. Similar structures have been used in the AlGaAs/GaAs material system in the same capacity[55,56], with reported[57] values for recombination velocity as low as 450 cm/s.

Table 4.1 shows the pulse heights and decay times measured on AlGaAsSb-capped samples of three thicknesses for a 0.02 mJ optical pulse excitation; all other parameters are nominally the same. The initial decay depends only on surface and bulk recombination and is found to increase with active layer thickness. This decay time is plotted with the thickness

Table 4.1 Photoreflectance Data from AlGaAsSb-capped OMVPE InGaAsSb (1064 nm Laser at 0.02 mJ Pulse Energy)

Sample	Active Layer thickness, p_0=2x10^{17} cm^{-3}	Pulse Height (mV)	Initial Decay (ns)	Long Decay (ns)	Long Decay Amp (%)
98-725	4 μm	24	50	156	31
98-723	6 μm	19	62	237	21
98-728	8 μm	24	64	167	34

on a 1/τ versus 1/*W* plot in Figure 4.2. Similar data taken with lower optical absorption density filters in place to increase the pulse energy are also plotted in this figure, with the relative intensities indicated.

The data for the binary capped samples is listed in Table 4.2 for five different active layer thicknesses. As expected from TPV device performance[7], similar pulse heights and

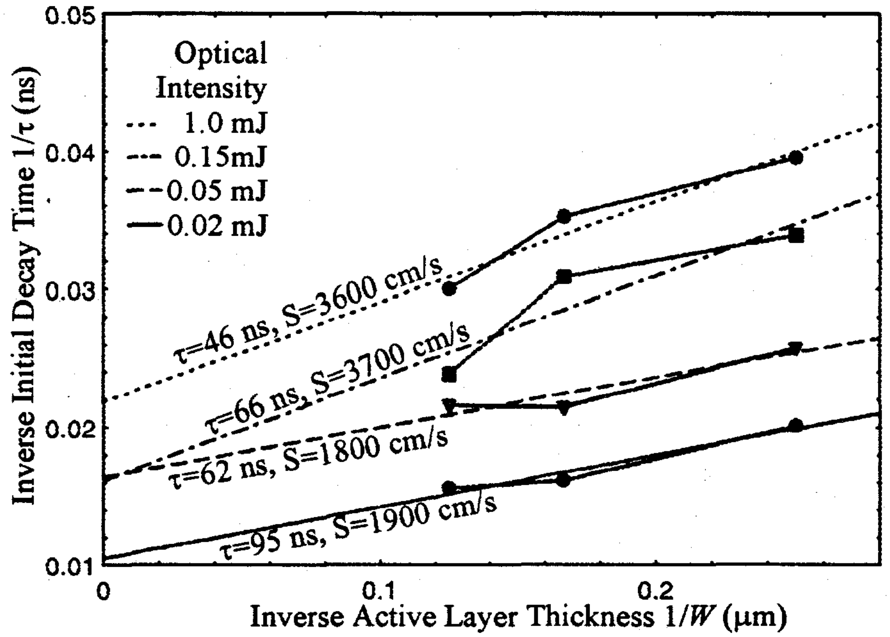

FIGURE 4.2 Extraction of SRV from Bulk Lifetime for Different Optical Intensities with AlGaAsSb Cap

Table 4.2 Photoreflectance Data from GaSb-capped OMVPE InGaAsSb
(1064 nm Laser at 0.02 mJ Pulse Energy)

Sample	Active Layer thickness, p_0=2x10^{17} cm^{-3}	Pulse Height (mV)	Initial Decay (ns)	Long Decay (ns)	Long Decay Amp (%)
98-812	1.5 μm	23	38	386	16
98-813	2 μm	24	34	162	18
98-814	3 μm	30	40	477	15
98-815	5 μm	32	46	*N/A	*N/A
98-816	8 μm	30	51	*N/A	*N/A

*Signal too small to be measured

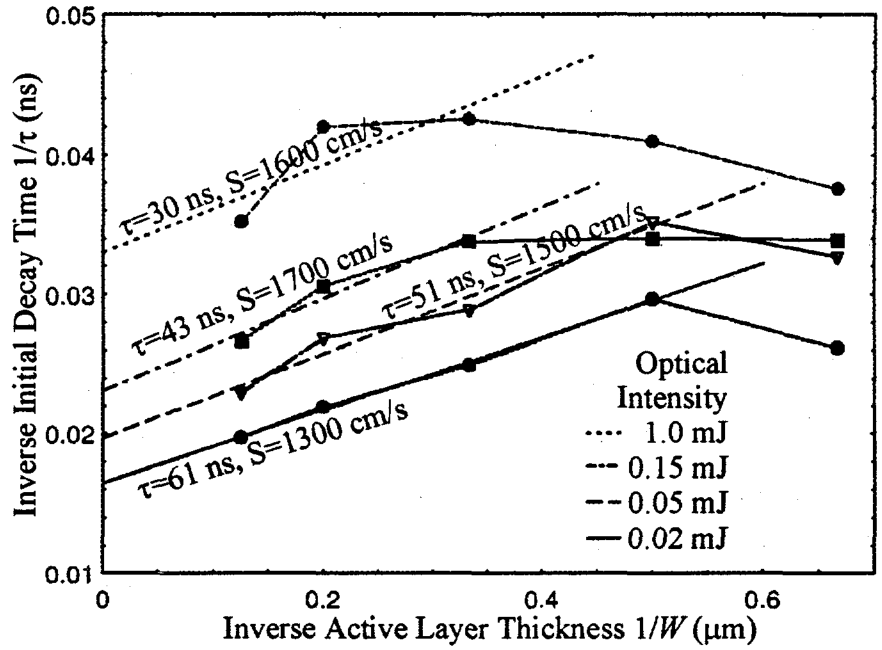

FIGURE 4.3. Extraction of SRV from Bulk Lifetime for Different Optical Intensities with GaSb cap

initial decays are obtained from these samples as compared to the quaternary capped structures. The initial decays are plotted in Figure 4.3 as a function of active layer thickness with the relative intensity varied as above. The extracted values for bulk lifetime are ~33% lower than those in Figure 4.2. The values for SRV are on the same order of magnitude and indicate that both caps provide good surface passivation. This result agrees with the high values (50-60%) measured[7] for external quantum efficiencies of devices fabricated with these caps. The departure of the inverse decay times of the thinner samples from the straight lines predicted by Equation (4.5) can be attributed to the lack of an abrupt interface as compared to the active layer thickness. In addition, more light is absorbed in the substrate as the active layer thickness is decreased, and the substrate lifetime may contribute to the measured decay time.

4.3. Characterization of Bulk Recombination

The bulk lifetime, τ_B, depends on SRH, radiative, and Auger recombination. Separation of the more conventional SRH recombination from radiative and Auger recombination is important in guiding material research and in designing optimum TPV device structures. For SRH recombination, the lifetime is given by τ_n under low-level injection, and $\tau_n+\tau_p$ under high-level injection levels, where $\tau_{n,p}=\sigma_{n,p}v_{th}N_t$, $\sigma_{n,p}$ is the electron (hole) capture cross-section, v_{th} is the thermal velocity, and N_t is the defect density. At 1064 nm, the laser full intensity excitation of 1 mJ corresponds to an initial excess carrier concentration in the range of 1.5×10^{19} to 5.9×10^{19} cm^{-3} for active layers 2-8 μm thick. This high level of injection (2.5 to 3 orders of magnitude above the active layer doping of 2×10^{17} cm^{-3}) necessitates the inclusion of high level injection effects on radiative and SRH recombination when interpreting the extrapolated value for bulk lifetime.

If radiative recombination is the dominant bulk recombination process, the following equation describes the distribution of excess carriers:

$$\frac{\partial n}{\partial t} = -\frac{G_{th}(n_0 + p_0 + n)n}{n_i^2} + D_n \frac{\partial^2 n}{\partial x^2} \quad , \tag{4.6}$$

where G_{th} is the thermal generation rate, n_0 and p_0 are the equilibrium electron and hole concentrations, respectively, and n_i is the intrinsic carrier concentration. A closed form solution of the above partial differential equation is not possible in general; but if the carrier concentration is assumed to be uniform, as is the case when both surfaces are good and $W \ll L_n$, the resulting ordinary differential equation can be solved[58] to give:

$$n(t) = \frac{(n_0 + p_0)n(0)}{\left(n_0 + p_0 + n(0)\right)e^{t/\tau_{rad}} - n(0)}, \quad \tau_{rad} = \frac{n_i^2}{G_{th}(n_0 + p_0)} \quad , \tag{4.8}$$

where $n(0)$ is the initial concentration of excess carriers following the photo excitation. This result is valid for times greater than that required for the carriers to diffuse through the active layer (W^2/D_n) and create a uniform distribution. For the practical layer thicknesses (3 to 5 μm) and typical diffusion constants of interest (~26 cm^2/s), the diffusion time is on the order of 3.5 to 10 ns.

The complete solution is plotted in Figures 4.4 and 4.5 for τ_{rad}=50 ns, a doping concentration p_0=2×10^{17} cm^{-3}, and the initial excess carrier concentration ranging from $n(0)$=10^{16} to 10^{21} cm^{-3}. The effective decay time shown in Figure 4.5 (extracted from the slope in Figure 4.4) indicates a dependence on the excitation level, with less excitation dependence in high-level injection. If the decay time is measured as a function of initial excess carrier concentration at a time 10 ns after the excitation pulse (to allow for a system

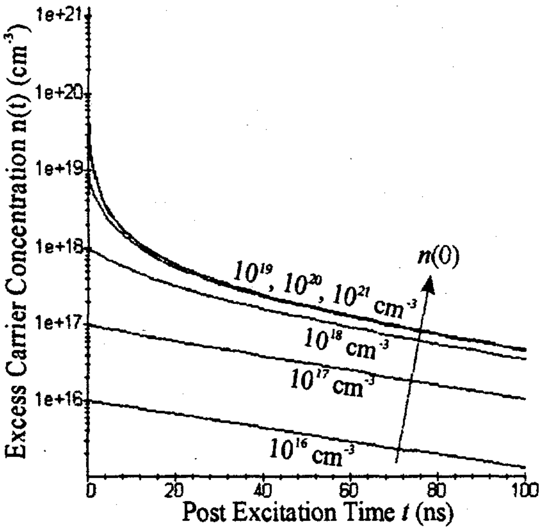

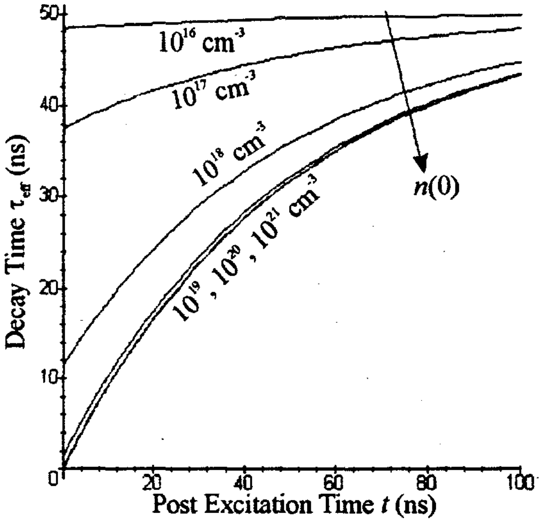

FIGURE 4.4. Radiative Recombination Solution of Excess Carriers for τ_{rad}=50 ns

FIGURE 4.5. Exponential Decay Time of Radiative Recombination Solution

response time of 5 ns), the effective decay time decreases with increasing excitation level as depicted in Figure 4.6.

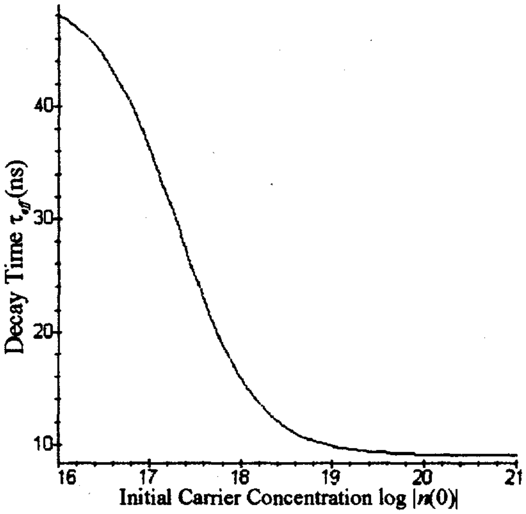

FIGURE 4.6. Effective Radiative Recombination Decay Time at t=10 ns

Auger recombination involves three carriers and is therefore in general a relatively weak effect except in heavily doped semiconductors or in the case of high level injection. The carrier distribution obeys the relationship[58]:

$$\begin{aligned}
\frac{dn}{dt} &= -\frac{(n_0+p_0+n)\left(n_0+\beta p_0+(1+\beta)n\right)n}{2n_i^2\tau_i} \quad , \\
\text{where:}\quad \beta &= \frac{\zeta^{1/2}(1+2\zeta)}{(2+\zeta)}e^{-\left(\frac{1-\zeta}{1+\zeta}\right)\frac{E_g}{kT}} \quad , \quad \zeta = \frac{m_C}{m_V} \quad , \\
\tau_i &= \frac{3.8\times10^{-18}\epsilon_S^2(1+\zeta)^{1/2}(1+2\zeta)e^{\frac{1+2\zeta}{1+\zeta}\frac{E_g}{kT}}}{\frac{m_C}{m_0}\left|F_1F_2\right|^2\left(\frac{kT}{E_g}\right)^{3/2}} \quad , \\
F_1 &= \int_V u_C^* u_V dr,\ F_2 = \int_V u_C^* u_C dr \quad ,
\end{aligned} \tag{4.9}$$

m_C and m_V are the conduction and valence band effective masses, respectively, E_g is the semiconductor bandgap, m_0 is the electron rest mass, ϵ_S is the relative dielectric constant, and u_C and u_V are the conduction and valence band wavefunctions, respectively.

Under high level injection, the Auger lifetime is given[58] by $\tau_A = 2\tau_i n_i^2/n(0)^2$ which has an inverse dependence on the excitation level squared. Using a linear interpolation of the effective masses[59] for electrons and holes in GaSb, GaAs, InAs, and InSb to obtain n_i=2.7×10^{13} cm^{-3} in 0.55 eV TPV devices and assuming $|F_1F_2|$=1 for a minimum τ_i of 25 ms, values for τ_A of 4×10^{-17} to 4×10^{-7} s are obtained for similar injection levels as for the radiative recombination analysis. A calculation[60] for $|F_1F_2|$ in InSb based on a Kronig-Penny model yielded a value of approximately 0.1 which results in τ_i=2.5 s or Auger lifetimes a factor of 100 greater than those given above.

The numerical solution of the above differential equation is shown in Figure 4.7 and

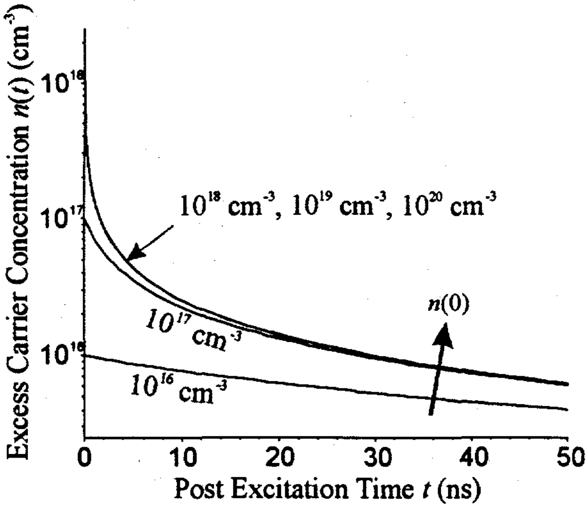

FIGURE 4.7 Auger Recombination Solution for Increasing Initial Carrier Concentration

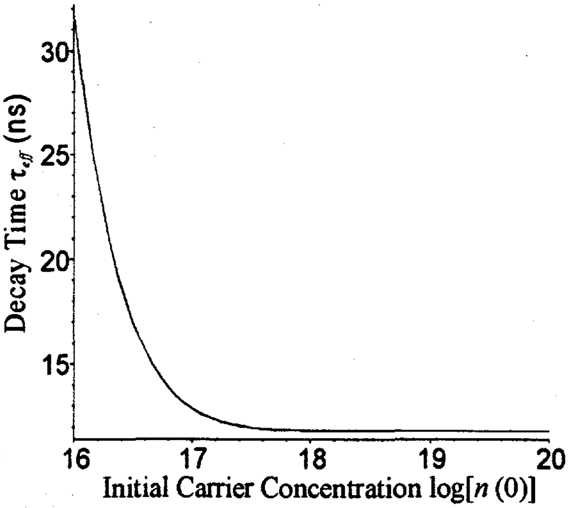

FIGURE 4.8 Exponential Decay Time of Auger Solution at t=10 ns

the effective exponential decay time (calculated from the slope 10 ns after the pulse) is shown in Figure 4.8 for τ_i=25 ms and different injection levels. With the value for n_i given above, the decay time decreases by a factor of three as $n(0)$ increases from 10^{16} to 10^{17} cm^{-3} and remains relatively constant at 12 ns for higher initial carrier concentrations. Comparison of Figures 4.6 and 4.8 shows that for the case of τ_{rad}=50 ns and τ_i=25 ms, the measured decay time is dominated by radiative recombination at higher injection levels and by Auger recombination at injection levels between 10^{16} and 3×10^{18} cm^{-3}.

The bulk recombination processes may be combined into a bulk lifetime by $1/\tau_B=1/\tau_{SRH}+1/\tau_{rad}+1/\tau_{Auger}$. Since these components exhibit a different dependence on excitation level, varying the laser pulse energy can differentiate between SRH, radiative, and Auger recombination by modulating the amount of photogenerated carriers. For SRH dominated recombination, the minority and majority carrier lifetimes are determined from the low-level and high-level injection conditions. For radiative and Auger recombination, the data must be fit with the equations that generate the curves of Figures 4.6 and 4.8 to extract radiative and intrinsic Auger lifetimes.

The initial decay times measured 30 ns after the laser pulse with surface components subtracted (i.e., bulk lifetime) versus the laser intensity relative to 0.02 mJ are plotted on a log scale in Figure 4.9 for each of the quaternary capped samples. Due to the similarity of this data with the plot of the solution of the effective radiative recombination equation 10 ns following the laser pulse (Figure 4.6), as well as the absence of a slow initial decay followed by a faster decay which is typical of SRH high level injection, radiative recombination appears to be the dominant mode in high level injection. The fits with the radiative model using a steepest descent algorithm[61] are superimposed in Figure 4.9.

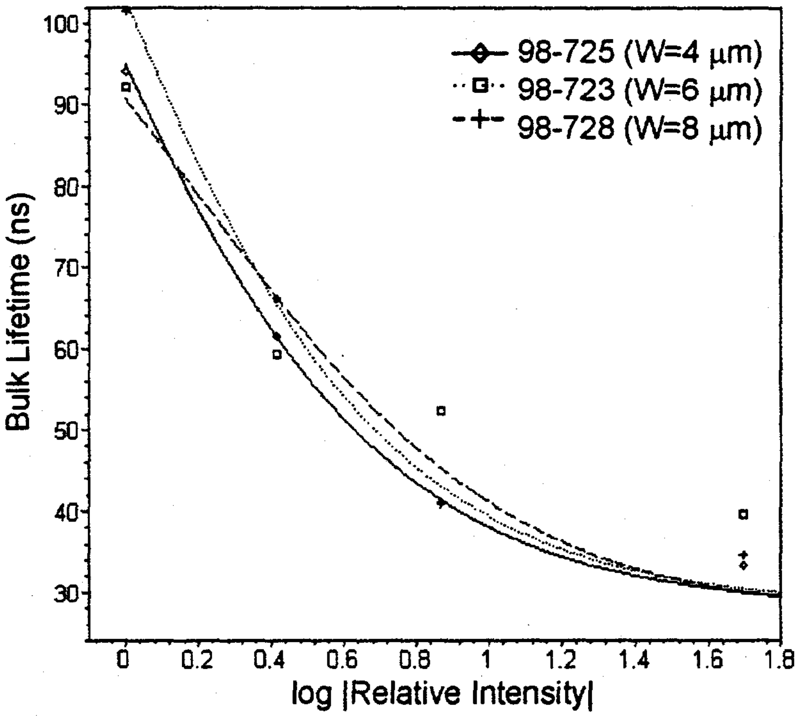

FIGURE 4.9 Fit of Radiative Recombination Model to AlGaAsSb-Capped InGaAsSb Bulk Lifetime for Different Active Layer Thicknesses

Using the background doping, p_0, and the excitation level, $n(0)$, as parameters, values of 210, 230, and 130 ns were obtained for the radiative lifetime of samples 98-725, -723, and -728, respectively. This variance in radiative lifetime, larger than the experimental error of the system (±3 ns with filters), is attributed to the lack of robustness of the fitting algorithm and/or run-to-run repeatability in the growth process (which can be manifested as variation in the bandgap). Since radiative recombination plays a greater role at high injection levels, the variance observed increases the error in the extrapolated bulk lifetime and SRV of Figures 4.2 and 4.3. Thus, the most accurate value for the bulk lifetime of InGaAsSb layers and the SRV of the InGaAsSb/AlGaAsSb interface are obtained from the lowest intensity data (i.e., τ_B=95 ns, S_1=S_2=1900 cm/s).

The bulk lifetimes of the GaSb-capped samples are plotted versus relative intensity in Figure 4.10 for the 2, 3, 5, and 8 μm samples (98-813, -814, -815, and -816, respectively). The least-squares fits using the radiative recombination model are superimposed with radiative lifetimes of 55, 73, 72, and 66 ns, respectively. The bulk lifetimes of the three thicker samples fit the radiative model well, whereas those of the 2 μm sample do not fit as well. The data for the 1.5 μm sample has been omitted due to an even poorer fit. Note that in the plot of Figure 4.3 the decay times of the 1.5 μm-thick samples and, for the higher intensities, those of the 2 μm-thick sample depart from the linear fits towards longer times. Thus, absorption in the p-type GaSb substrate is believed to be occurring in samples less than 3 μm thick, thereby obscuring the bulk recombination behavior in the active layer.

The absorption constants and indices of refraction calculated for the 0.55 eV InGaAsSb active layer (based on the optical constants of the constituent binaries and listed in Appendix D), in agreement with those measured by Muñoz *et al.*[62], can be used to

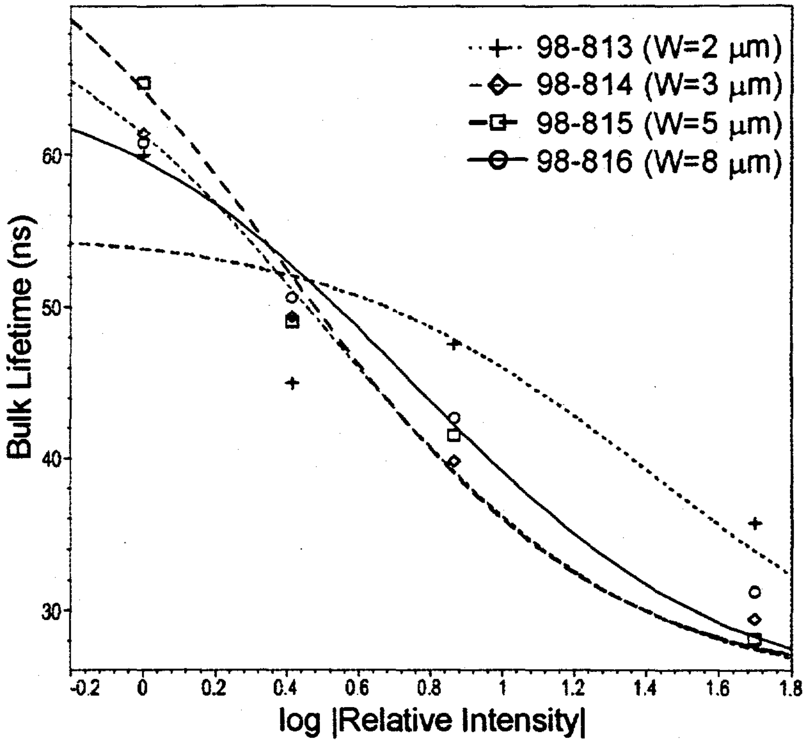

FIGURE 4.10 Fit of Radiative Recombination Model to GaSb-Capped InGaAsSb Bulk Lifetime for Different Active Layer Thicknesses

calculate the thermal generation rate from the vanRoosbroeck-Shockley relationship [Eq. (2.24)] to give 1.4×10^{17} cm^{-3}s^{-1}. Using the intrinsic carrier concentration of 2.7×10^{13} cm^{-3} gives a radiative coefficient ($B_r=G_r/n_i^2$) of 1.9×10^{-10} cm^3/s and a radiative lifetime of 26 ns in 2×10^{17} cm^{-3} doped samples. The results from several different calculations of the radiative coefficient have been presented by Charache *et al.*[63] giving the theoretical range for radiative lifetime of 70 to 500 ns in this material at the doping level given.

The results of fitting the 0.55 eV samples with the radiative recombination model fall within the theoretical range given above and are summarized in Table 4.3. Also listed are the measured[64] double-crystal X-ray diffraction peak separation (a measure of lattice mismatch), and the RMS error (a measure of the agreement between.the measured bulk lifetimes and the

Table 4.3 Result of Fitting 0.55 eV InGaAsSb with Radiative Recombination Model

Sample	Cap	Growth Temp. (°C)	Thickness (μm)	X-ray Peak Sep. (arc-sec)	τ_{rad} (ns)	RMS Error (ns)
98-725	AlGaAsSb	550	4	-223	210	1.7
98-723			6	42	230	2.4
98-728			8	507	130	6.9
98-813	GaSb	525	2	101	55	4.8
98-814			3	91	73	1.4
98-815			4	128	80	2.0
98-816			8	166	66	1.9

radiative recombination model). The large decrease in radiative lifetime for the 8 μm AlGaAsSb-capped sample as compared to the thinner samples (98-725 and 98-723) correlates with the high X-ray peak separation, indicating that large strain reduces the radiative lifetime. In addition, the RMS error increases with X-ray peak separation, indicating that other modes of bulk recombination play a greater role in heavily strained layers. Such a correlation is not as obvious for the GaSb-capped samples due to the smaller spread in X-ray peak separation.

Neglecting the samples with the largest RMS errors (98-728 and 98-813) the difference in radiative lifetimes between the AlGaAsSb-capped (220 ns average) and the GaSb-capped (73 ns average) samples appears to correlate with the sample growth temperature, suggesting that samples grown at higher temperatures are higher in quality. However, as shown in Figure 4.11, the full-width half-maxima (FWHM) of photoluminescence (PL) peaks, which are a measure of crystalline quality, obtained[64] from the GaSb-capped samples (525 °C) are less than those of either the AlGaAsSb-capped samples

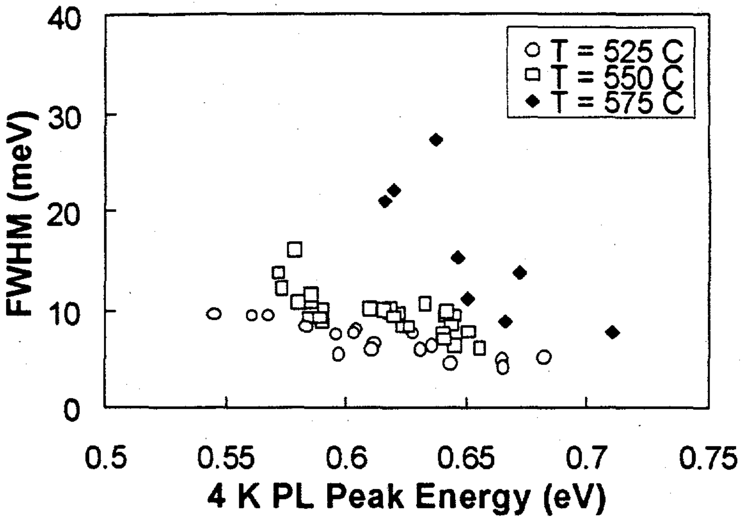

FIGURE 4.11 FWHM of 4 K PL Peaks from OMPVE InGaAsSb Grown at Different Temperatures (from C. A. Wang, Lincoln Laboratories)

(550 °C) or the samples grown at 575 °C, thus indicating that lower growth temperatures result in higher quality material.

Another difference between the two sets of samples is the index of refraction of the caps (3.75 measured[72] for GaSb and 3.64 calculated[65] for 1 eV AlGaAsSb) for light with energy at the 0.55 eV bandgap of the active layer. The mismatch between the indices of the cap and the active layer (3.73 calculated[65] at the same wavelength) results in a reflection of light at the heterointerface emitted via radiative recombination. The reflectivities of the AlGaAsSb and the GaSb interface are very low (1.7×10^{-4} and 2.5×10^{-5}, respectively) for this light and cannot be the source of the difference observed. However, due to the large difference in index between the cap layers and air, there is a considerable amount of internal reflection which can enhance photon recycling in both structures.

The presence of photon recycling was investigated[66] using a 4 µm-thick 0.53 eV

InGaAsSb structure doubly-capped with AlGaAsSb layers grown on GaSb. The radiative lifetimes were compared before and after deposition of 2000 Å of Au followed by a 350 °C anneal for 5 s on the substrate side. The processing was intended to scatter photons emitted from radiative recombination events occurring in the active layer and arriving at the back surface of the substrate, thereby reducing the reflectivity. Bulk lifetimes were measured as a function of injection level and then fit to a radiative recombination model as performed above. The radiative lifetime of the sample prior to Au deposition was found to be 110 ns and decreased to 61 ns after the deposition and anneal. To eliminate the possibility that the change observed was due to the thermal processing, the Au layer was subsequently removed by mechanical polishing after which the radiative lifetime increased to 95 ns. Therefore, photon recycling appears to be present in the InGaAsSb material system.

4.4. 0.5 to 0.6 eV Doubly-Capped OMVPE InGaAsSb

The effect of bandgap variation on bulk recombination was investigated using four 2 μm thick undoped (p_0=10^{16} cm^{-3}) InGaAsSb samples grown via OMVPE at 525 °C with GaSb caps similar to that in Figure 4.1b, but having different In concentrations. The room temperature bandgaps of the samples, determined by photoluminescence measurements[64], were 0.50, 0.52, 0.55, and 0.59 eV. Using the value obtained with the previous set of GaSb-capped 0.55 eV InGaAsSb samples of 1300 cm/s for the SRV and assuming no bandgap dependence, the values of bulk lifetimes are plotted in Figure 4.12 as a function of optical pulse energy relative to 0.02 mJ. Since these samples are undoped, the injection level is over an order of magnitude higher than in the samples used in the previous section. Thus, very-

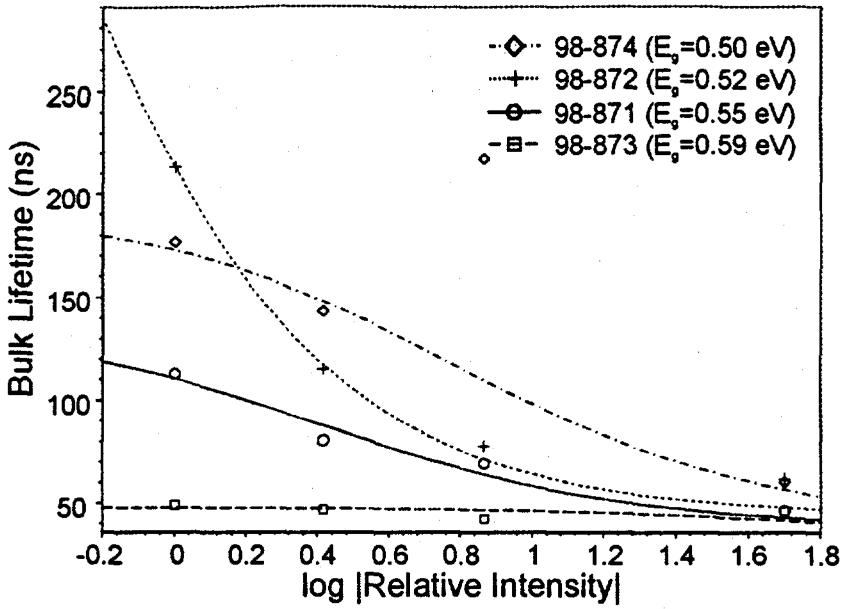

FIGURE 4.12 Fit of Radiative Recombination to GaSb-Capped InGaAsSb Bulk Lifetime for Different Bandgaps Assuming Bandgap-Independent Surface Recombination Velocities

high-level injection effects are expected to be observed. Furthermore, since the active layers are 2 μm-thick, absorption in the substrate is expected to increase the error in fitting. The least-squares curves fit to the data using the radiative recombination model are superimposed in the figure; the results of the fitting are summarized in Table 4.4, along with the double-crystal X-ray peak shift and calculated RMS error.

The radiative lifetime appears to decrease as the bandgap increases, with the

Table 4.4 Result of Fitting GaSb-capped InGaAsSb with Radiative Recombination Model

Sample	Bandgap (eV)	X-ray Peak Sep. (arc-sec)	τ_{rad} (ns)	RMS Error (ns)
98-874	0.50	93	190*	*
98-872	0.52	109	930	7.7
98-871	0.55	195	140	4.9
98-873	0.59	-26	48	3.3

* One data point discarded to improve fitting and RMS error is omitted

exception of the 0.50 eV sample where one data point at 220 ns was excluded from the fitting to promote convergence of the fitting algorithm. As with the previous set of GaSb-capped samples, there is no clear correlation between X-ray peak shift and radiative lifetime. Furthermore, since the calculated index of refraction[65] of the active layers for light with energy at their respective bandgap is approximately invariant (0.12% change) over the range of bandgaps grown, the reflectivity at the GaSb interface is the same for each sample, thus eliminating photon recycling as a possible source of effective radiative lifetime dependency on bandgap. The increasing error for the lower bandgap samples may be an indication that other modes of bulk recombination, especially Auger recombination, have a greater influence as the bandgap decreases from 0.59 eV.

An algorithm was developed which attempts to fit bulk lifetime measurements as a function of excitation level to a combined radiative and Auger recombination model. The details are presented in Appendix B as an extension to the current method of analysis. However, results using the data presented above suggest that Auger recombination dominates in the 0.55 eV sample with an Auger coefficient of 2.2×10^{-26} cm^{6}s^{-1}, which corresponds to an Auger lifetime of 450 ns in an unilluminated sample while the radiative lifetime was 11 μs (B_r=9.1×10^{-12} cm^3/s). In the 0.50, 0.52, and 0.59 eV samples, radiative recombination dominates with radiative lifetimes of 200 ns, 40 μs, and 92 ns, respectively.

A calculation of the energy separations between the Γ, L, and X conduction band minima and the valence band maximum in InGaAsSb lattice-matched to GaSb along with the spin-orbital splitting is shown in Figure 4.13. Since Auger recombination rates of the *CHHS*

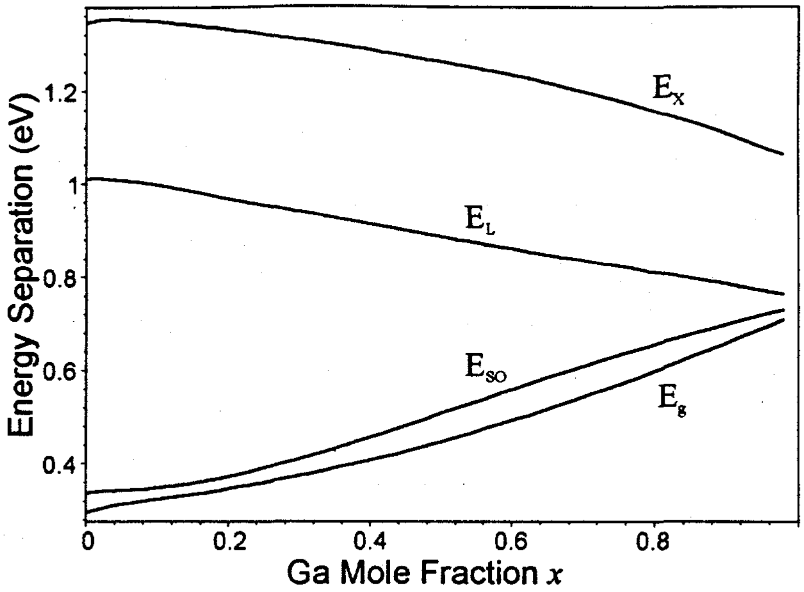

FIGURE 4.13 Energy Separations Between Γ, L, and X Conduction Band Minima and Valence Band Maximum, and Spin-Orbital Splitting for InGaAsSb Lattice-Matched to GaSb (after Adachi[65])

process, in which a conduction band electron (*C*) recombines with a heavy hole (*H*) and excites a heavy hole (*H*) to the spin-split-off band (*S*) and is the dominant Auger process in

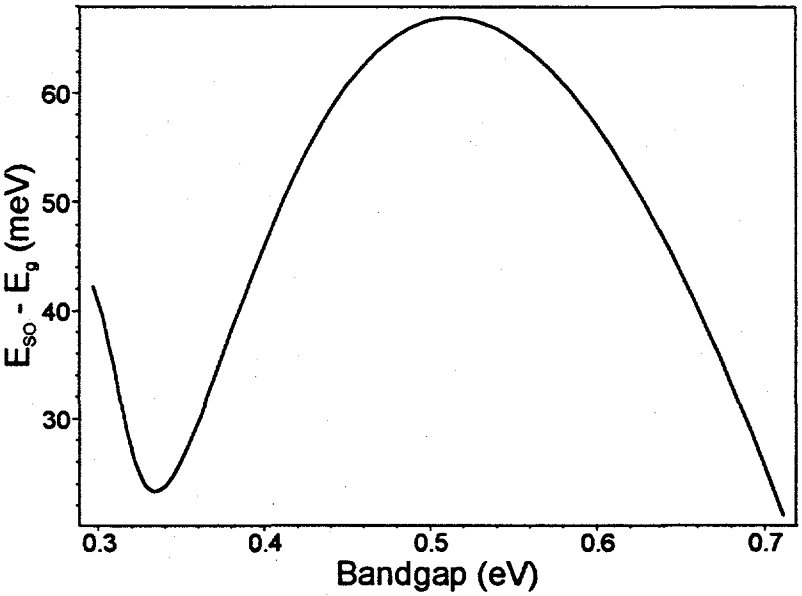

FIGURE 4.14 Energy Difference Between Calculated Spin-Orbital Splitting and Bandgap for InGaAsSb Lattice Matched to GaSb (after Adachi[65])

GaSb[67], are at a maximum when the spin-orbit splitting is near the bandgap energy, the Auger recombination rate is expected to be at a minimum for samples with bandgaps near 0.52 eV (as evident from Figure 4.14). Thus, the Auger lifetime is expected to decrease for the wider bandgap samples measured in this section. The apparent lack of agreement between the results of the combined radiative-Auger fitting and those obtained with purely radiative fitting are attributed to the small number of intensities for which data has be recorded, since the algorithm combining the two recombination modes inherently has more fitting parameters.

4.5. Alternative Interpretation of Epitaxial InGaAsSb Bulk Lifetime

Recent experimental and theoretical work indicate that photon recycling is important in appropriately designed antimonide-based structures and TPV devices. As a result, the experimental data for bulk lifetime presented in this chapter was re-analyzed (in a preliminary fashion) assuming photon recycling in the doubly-capped structures results in a very large effective radiative lifetime.

Under the above condition, SRH and Auger recombination dominate the bulk recombination at the extremes of injection level, requiring the bulk lifetimes to be fit to a model which incorporates both SRH and Auger recombination. Unfortunately, the resulting set of equations (listed in Appendix C) involves numerical solution of the continuity equation describing SRH recombination. Furthermore, there are five parameters required to fit the bulk lifetimes: the ratio of electron and hole capture cross-sections, the energy level of the defect within the bandgap, the low-level SRH lifetime, the intrinsic Auger lifetime, and the injection level. As a result, a full analysis comparable to the descriptions in section 4.3 and

4.4 is not possible at this time.

4.6. Summary

Recombination in epitaxial films was analyzed to determine the relative contributions of bulk and surface recombination. When the layer has identical front and back surfaces, determination of the bulk lifetime and surface recombination velocity (SRV) is possible by growing test structures with different thicknesses. Analysis of Shockley-Read-Hall (SRH), radiative, and Auger recombination lifetimes showed that each has a different dependence on injection level. Therefore, examination of the bulk lifetimes at various intensities reveals the dominant mode of bulk recombination. Furthermore, fitting the bulk lifetimes to the solutions of the recombination equations results in lifetimes for radiative recombination.

The 1 eV p-AlGaAsSb and 0.72 eV p-GaSb caps on 0.55 eV p-InGaAsSb active layer interfaces were characterized. Both interfaces show low SRV, on the order of 10^3 cm/s. The 2×10^{17} cm^{-3} Zn-doped 0.55 eV organometallic vapor phase epitaxy (OMVPE) active layer demonstrates radiative recombination behavior with strain-modulated radiative lifetime on the order of 200 ns for the AlGaAsSb-capped samples, whereas a relatively strain-independent radiative lifetime of ~70 ns was obtained for the GaSb-capped samples. Absorption in the substrate is suspected as the cause of increased error in fitting the bulk lifetimes of samples with active layer thicknesses less than 3 μm. The apparent differences in radiative lifetime between the two sets of samples are most likely not due to the fact that the GaSb-capped samples were grown after modifications to the OMVPE reactor and at a lower temperature (525 °C versus 550 °C), based on photoluminescence measurements. The difference observed may be resolved through fitting with a combined SRH and Auger recombination model; however, additional data over a wider range of intensity levels, wavelengths, and possibly temperature would be needed for a full evaluation.

The bulk lifetimes measured from GaSb-capped undoped InGaAsSb layers with 0.50 to 0.59 eV bandgaps yielded radiative lifetimes ranging from a minimum 50 ns for the 0.59 eV active layer to a maximum of 960 ns for the 0.52 eV active layer. Since the index of refraction is approximately the same for each of the active layers, photon recycling is not believed to cause the change in radiative lifetime. While the range of optical pulse energies used with these samples was the same as for the previous set of GaSb-capped samples these samples are undoped. Therefore, Auger recombination, which depends heavily on the band structure, is likely the reason for the increased fitting error observed with the lower bandgap samples.

5. Separation of Bulk and Surface Effects in Thick Substrates

In substrate samples, where the thickness is generally much greater than both the carrier diffusion length and the characteristic optical absorption depth (α^{-1}), the back surface has no effect on the carrier distribution. Since varying the sample thickness will not influence the decay time, other means of controlling the contribution of the front surface are necessary to separate the effect of the front surface from the bulk recombination on the measured decay time. In this chapter, an analysis using values of α to control the surface lifetime is presented, followed by measurements on GaSb and quasi-binary InGaAsSb substrates at different optical wavelengths (and therefore different values of α).

5.1. Analysis of Recombination in Thick Substrates

5.1.1. Separation of Surface Recombination Velocity and Bulk Lifetime

Analysis of the photoreflectance decay transient in thick boule samples was accomplished by solving the transient diffusion equation for a uniform distribution of bulk recombination centers, with the assumptions that the RF signal penetrates the entire sample and that the optical excitation is an impulse. The latter assumption is valid for times after the laser pulse transient. The boundary conditions for the solution include a Beer's law distribution for the excess carriers at $t=0$ with N_{ph} incident photons/cm^2, a surface recombination velocity (SRV) of S_R at the front surface, and a vanishing excess carrier concentration at the back surface for a semi-infinite solid. For p-type material with bulk lifetime τ_B and electron diffusion constant D_n, the excess electron concentration obeys the relations:

$$\frac{\partial n}{\partial t} = -\frac{n}{\tau_B} + D_n \frac{\partial^2 n}{\partial x^2}, \quad n(x,0) = \alpha N_{ph} e^{-\alpha x}$$
$$D_n \left.\frac{\partial n}{\partial x}\right|_{x=0} = S_R n, \quad \text{and } n(\infty,t) = 0 \quad , \tag{5.1}$$

where α is the absorption constant of the monochromatic light. The preceding equations are simplified by substituting

$$n(x,t) = f(x,t) \cdot e^{-t/\tau_B} \tag{5.2}$$

in the continuity equation, thus giving

$$D_n \frac{\partial^2 f}{\partial x^2} = \frac{\partial f}{\partial t} \quad . \tag{5.3}$$

Solution of this equation (subject to the boundary conditions given above) is accomplished through the Laplace transform in the time domain as follows:

$$\mathcal{L}\left[\frac{\partial f(x,t)}{\partial t}\right] = sF(x,s) - f(x,0+) = sF(x,s) - \alpha N_{ph} e^{-\alpha x}$$
$$D_n \frac{\mathrm{d}^2 F(x,s)}{\mathrm{d}x^2} - sF(x,s) = -\alpha N_{ph} e^{-\alpha x} \tag{5.4}$$
$$\Rightarrow F(x,s) = Ae^{-\lambda x} + Be^{\lambda x} + \frac{\alpha N_{ph}}{s - \alpha^2 D_n} e^{-\alpha x} \quad , \lambda = \sqrt{\frac{s}{D_n}} \quad .$$

The value of the constant B must be 0 for the solution to remain finite throughout the semi-infinite slab, and the value of the constant A can be obtained by applying the boundary condition on the front surface (i.e., $D_n \, \partial n/\partial x|_{x=0} = S_R n$), giving

$$F(x,s)=\frac{\alpha N_{ph}}{s-\alpha^2 D_n}\left(e^{-\alpha x}-\frac{S_R+\alpha D_n}{S_R+\lambda D_n}e^{-\lambda x}\right)\quad . \tag{5.5}$$

Integrating $F(x,s)$ over the thickness to obtain the total free carrier concentration in the Laplace domain, i.e., $G(s)$, yields

$$G(s)=\int_0^\infty F(x,s)\mathrm{d}x=\frac{N_{ph}}{s-\alpha^2 D_n}-\frac{N_{ph}\alpha(S_R+\alpha D_n)}{\sqrt{s}\left(\sqrt{s}+\frac{S_R}{\sqrt{D_n}}\right)\left(s-\alpha^2 D_n\right)}, \tag{5.6}$$

which has poles at $s^{1/2}=0$, $s^{1/2}=(\alpha^2 D_n)^{1/2}$, $s^{1/2}=-(\alpha^2 D_n)^{1/2}$ and $s=S_R^{\,2}/D_n$. This expression can be rewritten using partial fraction expansion as

$$\begin{gathered}G(s)=\frac{A}{\sqrt{s}}+\frac{B}{\sqrt{s}+\frac{S_R}{\sqrt{D_n}}}+\frac{C}{\sqrt{s}+\alpha\sqrt{D_n}}+\frac{D}{\sqrt{s}-\alpha\sqrt{D_n}}\\ A=\frac{N_{ph}(S_R+\alpha D_n)}{\alpha S_R\sqrt{D_n}}\quad,\quad B=\frac{N_{ph}\alpha D_n^{3/2}}{S_R(S_R-\alpha D_n)}\quad,\quad C=-\frac{N_{ph}S_R}{\alpha\sqrt{D_n}(S_R-\alpha D_n)},\end{gathered} \tag{5.7}$$

and $D=0$. Taking the inverse Laplace transform, the integrated carrier concentration is

$$\begin{aligned}N(t)&=\Bigg[\frac{S_R+\alpha D_n}{\alpha S_R\sqrt{\pi D_n t}}+\frac{\alpha D_n^{3/2}}{S_R(S_R-\alpha D_n)}\left(\frac{1}{\sqrt{\pi t}}-\frac{S_R}{\sqrt{D_n}}e^{\frac{S_R^{\,2}t}{D_n}}\operatorname{erfc}S_R\sqrt{\frac{t}{D_n}}\right)\\ &\quad-\frac{S_R}{\alpha\sqrt{D_n}(S_R-\alpha D_n)}\left(\frac{1}{\sqrt{\pi t}}-\alpha\sqrt{D_n}e^{\alpha^2 D_n t}\operatorname{erfc}\alpha\sqrt{D_n t}\right)\Bigg]N_{ph}e^{-\frac{t}{\tau_B}} \\ &=\left[S_R e^{\alpha^2 D_n t}\operatorname{erfc}\alpha\sqrt{D_n t}-\alpha D_n e^{\frac{S_R^2 t}{D_n}}\operatorname{erfc}S_R\sqrt{\frac{t}{D_n}}\right]\frac{N_{ph}e^{-\frac{t}{\tau_B}}}{S_R-\alpha D_n}\quad .\end{aligned} \tag{5.8}$$

For low and high values of SRV, the above expression simplifies to the following

$$N(t)=\begin{cases} N_{ph}e^{-\frac{t}{\tau_B}}\ , & S_R=0 \\ N_{ph}e^{-\frac{t}{\tau_B}+\alpha^2 D_n t}\ \operatorname{erfc}\alpha\sqrt{D_n t}\ , & S_R\to\infty \end{cases}\ . \tag{5.9}$$

For intermediate values of SRV, the solution can be simplified for $t \gg D_n/S_R^2$ and $t \gg 1/\alpha^2 D_n$ using the asymptotic approximation[68]

$$\operatorname{erfc} x=\frac{e^{-x^2}}{x\sqrt{\pi}}\quad \text{for } x \gg 1 \tag{5.10}$$

to give

$$N(t)=\frac{N_{ph}(S_R+\alpha D_n)}{\alpha S_R}\ \frac{e^{-\frac{t}{\tau_B}}}{\sqrt{\pi D_n t}}\ . \tag{5.11}$$

By plotting $\ln[\sqrt{t}N(t)]$, a linear plot is obtained with a slope of $-1/\tau_B$ and, extrapolating back to the y-axis, a y-intercept of

$$\ln\left|\frac{N_{ph}(S_R+\alpha D_n)}{\alpha S_R\sqrt{\pi D_n}}\right|\ . \tag{5.12}$$

Thus, both the bulk lifetime and SRV can be extracted from the decay transient through this analysis.

In practice, due to the finite optical pulse width and decay time, the y-intercept of the $\ln[\sqrt{t}N(t)]$ plot may require a correction term. With an impulse optical excitation, the carrier concentration decay (Eq. (5.11)) is proportional to $N_{ph}t^{-1/2}e^{-t/\tau B}$ where N_{ph} is the number of photons/cm^2; if a 1 mJ pulse at 1064 nm is absorbed then N_{ph} is 1.9×10^{16} /cm^2. To determine

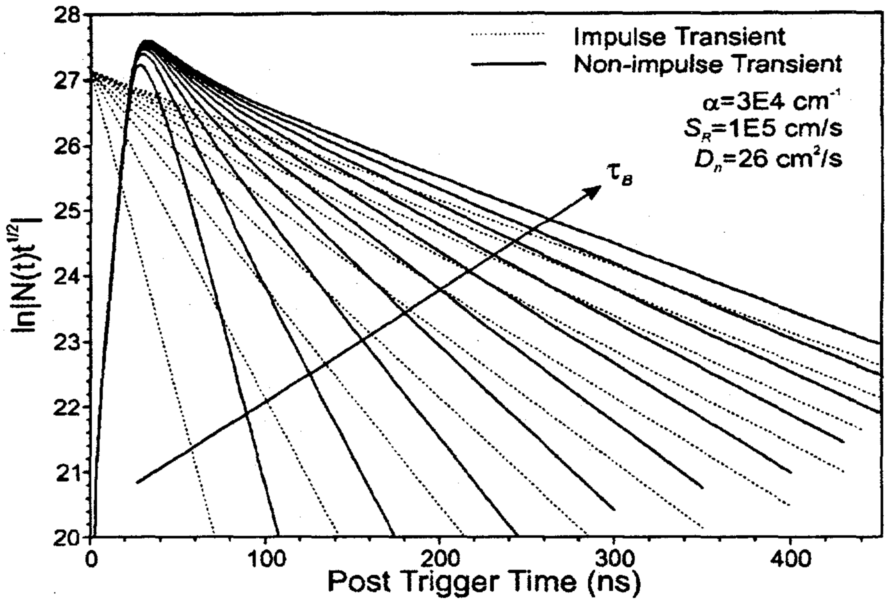

FIGURE 5.1 Transient Decays in a Substrate with a 1064 nm 1 mJ Impulse and Non-Impulse Optical Excitation for τ_B=10, 20, 30, 40, 50, 60, 70, 80, 90, and 100 ns

the impact of the finite pulse shape, the decay is calculated via convolution of the expression in Equation (5.8) with the analytical approximation of the optical pulse shape [Equation (3.2) and Fig. 3.6] and the response of the RF electronics.

Computed decay transients are shown in Figure 5.1 for different bulk lifetimes with t=0 at the trigger threshold for the non-impulse optical pulse (~ 1% of peak value) using the material parameters shown in the figure; superimposed on the figure are lines representing the asymptotic impulse transients [Eq. (5.11)] for comparison. Note that the non-impulse transients peak ~30 ns after the trigger followed by a relatively fast decay for τ_B>20 ns. The slope of the non-impulse transient, from which the bulk lifetime is obtained, approaches that of the impulse transient asymptotically, as expected, within at least 21 ns after the peak with a 10 ns bulk lifetime. The minimum time at which the measured decay yields an accurate bulk lifetime (±10%) is depicted as the broken curve in Figure 5.3 for which an empirical fit yields

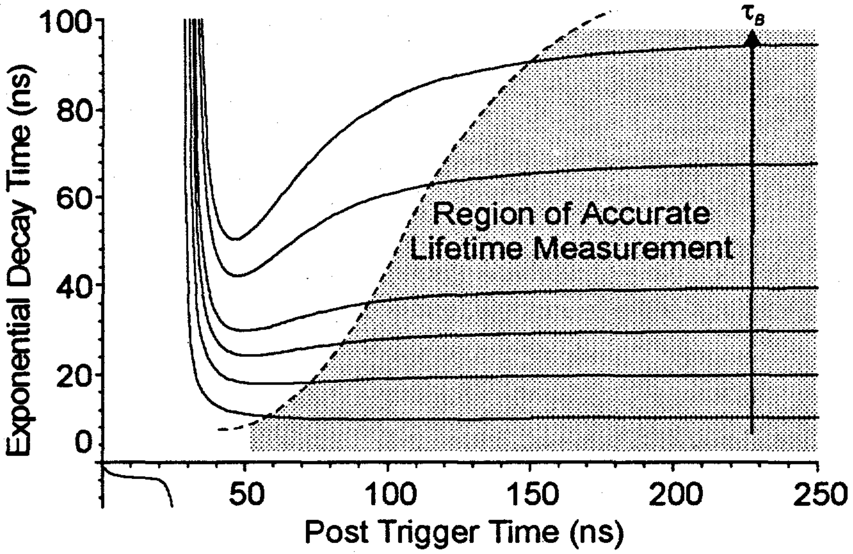

FIGURE 5.3 Exponential Decay Time in a Substrate with τ_B=10, 20, 30, 40, 70, and 100 ns for Non-Impulse Optical Excitation

$t_{min}=6.19\times10^{-5}\tau^3-1.39\times10^{-2}\tau^2+1.83\tau+7.02$ (valid for $10<\tau<200$ ns) measured after the peak of the non-impulse transient. Although the delay varies for different material parameters, the general shape of the transient remains unchanged qualitatively, i.e., an initial fast decay preceding the asymptotic decay.

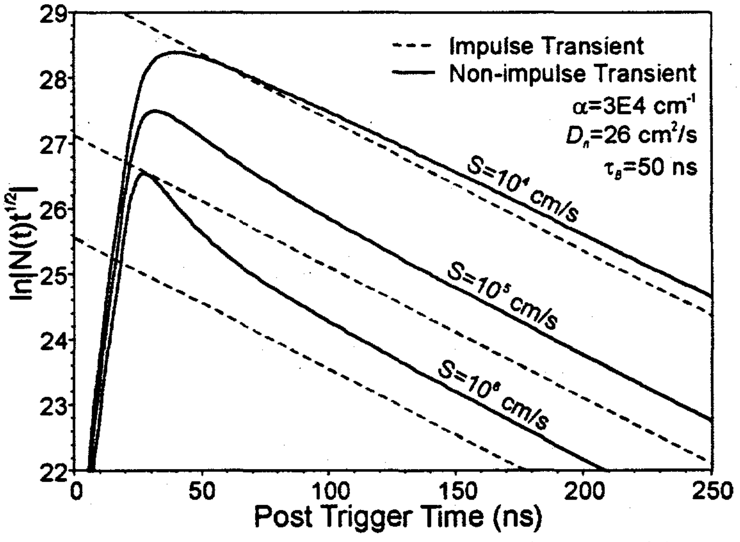

FIGURE 5.2 Transient Decays in a Substrate with a 1064 nm 1 mJ Impulse and Non-Impulse Optical Excitation for $S_R=10^4$, 10^5, and 10^6 cm/s

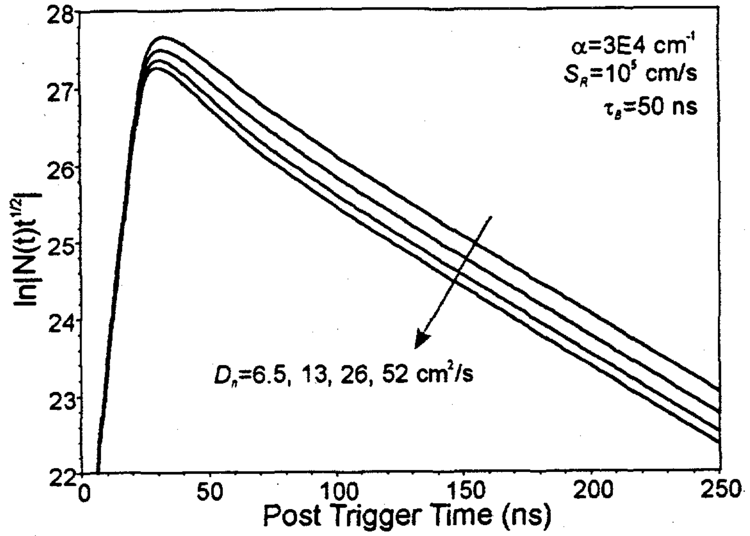

FIGURE 5.4 Transient Decays in a Substrate with a 1064 nm 1 mJ Non-Impulse Optical Excitation for D_n=6.5, 13, 26, and 52 cm^2/s

The computed decay transients are shown in Figure 5.2 and 5.4 for different values of surface recombination velocity and diffusion constant, respectively. The SRV has the greatest effect on the shape of the computed decay. Low values of SRV produce transients with a longer initial decay time compared to the bulk lifetime whereas for $S_R > 10^5$ cm/s the transients exhibit a faster initial decay time. Fitting a measured decay transient is possible in principle with S_R, D_n, and τ_B as fitting parameters; however, in order to decrease the computation time knowledge of D_n is desirable.

While the radio-frequency (RF) photoreflectance system is capable of measuring bulk lifetimes as low as 10 ns in substrates, the slope of the transient decay must be measured at increasingly later times after the transient peak as the bulk lifetimes increase, as much as 113 ns for a 100 ns bulk lifetime. Therefore, in order to observe high-level injection effects, the pulse energy must be selected for the high-level conditions that persist at the time when the lifetime can be measured accurately. For example, since the non-impulse transient is delayed by at least 10 ns from the peak of the optical pulse (see Fig. 3.6), in the case of a 10 ns bulk lifetime, the transient can be measured no less than 30 ns after the peak of the optical pulse, during which time the carrier density (cm^{-2}) from Equation (5.11) has decreased by a factor of 0.009, using the material parameters in Figure 5.1. Thus, N_{ph} must be much greater than $100N_A/W$, where N_A is the doping density and W is the sample thickness. For a 500μm-thick sample doped 5×10^{16} cm^{-3}, N_{ph} must be much greater than 2.5×10^{15} cm^{-2} and requires a pulse energy much greater than 0.13 mJ. Hence, the effects of radiative and Auger recombination in high-level injection are expected to be observed with a 1 mJ optical pulse. Since the decrease in carrier density is most significant for the minimum detectable bulk lifetime of 10 ns, SRH recombination, characterized by a slow initial decay followed by a faster decay, becomes easier to detect with longer bulk lifetimes.

Comparing the asymptote of the non-impulse transient to that of the impulse

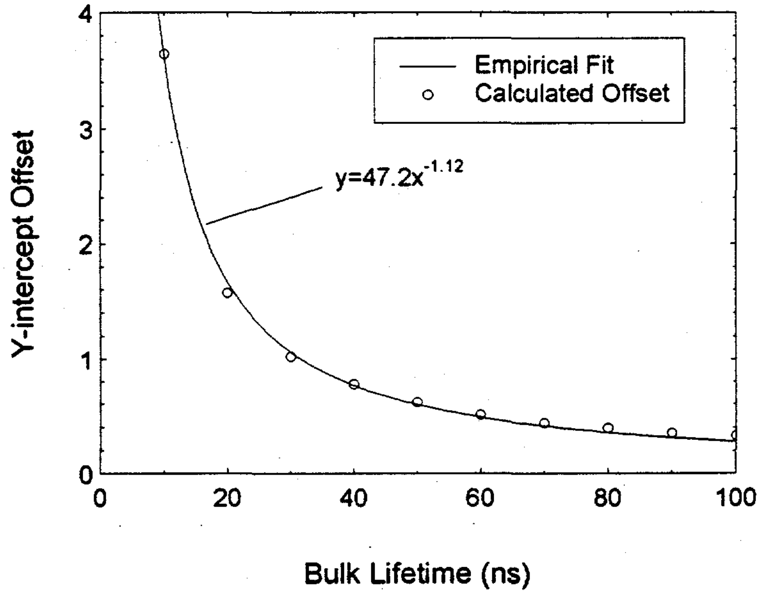

FIGURE 5.5 Y-intercept Offset of Transient Decay in Substrates Due to Non-Impulse Optical Excitation. Y-Intercept Offset is Obtained by Plotting $\ln|N(t)t^{1/2}|$ versus t (ns) where $N(t)$ is in Units of cm^{-2}.

transient, the y-intercept exceeds the ideal value by varying amounts depending on the bulk lifetime. The y-intercept offset is plotted in Figure 5.5 for a range of bulk lifetimes with an empirical fit of $47.2\tau_B^{-1.12}$ (τ_B in ns) superimposed for interpolation purposes. The offset is used to correct measured y-intercepts when calculating SRV.

The error in extrapolated y-intercept due to jitter in the triggering, noise in the transient decay, and the error due to uncertainty of material parameters results in an error in the value of S_R. From a first-order Taylor expansion of Equation (5.11) in terms of the y-intercept (B), the fractional error in S_R is estimated using

$$\frac{\Delta S_R}{S_R} = \frac{\Delta B}{S_R}\frac{\partial S_R}{\partial B} = -\frac{\alpha e^B \sqrt{\pi D_n}\Delta B}{\alpha e^B \sqrt{\pi D_n} - N_{ph}} \quad . \tag{5.13}$$

Thus, in order to calculate S_R to within 10%, the error in corrected B at 1064 nm must be less than 0.089 assuming $S_R = 10^5$ cm/s, $\alpha = 3.12\times10^4$ cm^{-1}, and $D_n = 26$ cm^2/Vs. For a bulk lifetime of 100 ns, the error in B translates into a maximum uncertainty of 9 ns in the time to which the fit line is extrapolated, i.e., the trigger time, using $\Delta t = \Delta B\tau$. With the present setup, this condition is easily met, since the risetime of the laser pulse that the trigger circuit of the digital oscilloscope monitors is on the order of 2 ns. Thus, the error in S_R is limited by noise in the transient.

For passivated samples (i.e., $S_R < 10^4$ cm/s) the condition under which Eqs. (5.11) and (5.12) are derived (i.e., $t \gg D_n/S_R^2$) applies to the long decay of the transient. In such cases, the analysis of the initial decay is achieved by first integrating the transient diffusion equation, Eq. (5.1), over the thickness of the sample to give

$$D_n \frac{\partial n(x,t)}{\partial x}\bigg|_0^\infty - \frac{N(t)}{\tau_B} = \frac{dN(t)}{dt} \quad . \tag{5.14}$$

Substituting the boundary conditions of Eq. (5.1) for the first term results in

$$-S_R n(0,t) - \frac{N(t)}{\tau_B} = \frac{dN(t)}{dt} \tag{5.15}$$

from which the instantaneous exponential decay time may be obtained by dividing by $N(t)$. Evaluating the result at $t=0$ gives the following expression for the initial decay:

$$\frac{-1}{N(t)} \frac{dN(t)}{dt}\bigg|_{t=0} = \frac{S_R n(0,0)}{N(0)} + \frac{1}{\tau_B} \quad . \tag{5.16}$$

From the initial condition in Eq. (5.1) and the fact that $N(0)=N_{ph}$, the initial decay time can be expressed as

$$\frac{1}{\tau_{eff}} = \alpha S_R + \frac{1}{\tau_B} \quad . \tag{5.17}$$

Thus, for passivated samples the initial decay time depends on the bulk lifetime, the SRV, and the absorption constant, i.e., wavelength of light, whereas the long decay time depends on the bulk lifetime. Due to the minimum decay time resolution of $\tau_{min}=10$ ns with the present system, use of Equation (5.17) is limited to cases where $\alpha S_R<1/\tau_{min}$, which in GaSb at 1064 nm wavelength requires $S_R < 3.2\times10^3$ cm/s; i.e., a well passivated surface. For surfaces with higher SRV, analysis is conducted with Equations (5.11) and (5.12).

5.1.2. Bulk Recombination

The equations that describe bulk recombination due to SRH, radiative, and Auger recombination were presented in section 4.3. However, due to the semi-infinite thickness of the substrate materials, the assumption that the carrier concentration is uniform is no longer valid. Therefore, the diffusion term remains and the solutions of the partial differential equations must be obtained numerically.

From a qualitative view, the equations for the three types of recombination differ only in their recombination term, i.e., n/τ_{SRH}, n^2/τ_{rad}, and n^3/τ_A for SRH, radiative, and Auger recombination in high-level injection, respectively. By dividing these equations by n to obtain equations for the reciprocal of the exponential decay time ($1/n \cdot \partial n/\partial t$), the resulting recombination term varies as $1/\tau_{SRH}$, n/τ_{rad}, and n^2/τ_A for SRH, radiative, and Auger recombination, respectively, where τ_{SRH} is given by τ_n for low-level injection, and $\tau_n + \tau_p$ for high-level injection in p-type material. Thus, one can generally describe the decay transients as either an exponential with decay time τ_{SRH}, an n^{-1} dependence, or an n^{-2} dependence, respectively. This description serves to determine the dominant mode of bulk recombination.

When trapping centers are active, i.e., unfilled, an additional type of loss mechanism for the carrier concentration must be considered. Trap emission is typically a slow process, compared to the three forms of bulk recombination. The emission rate is determined by the position of the trap level within the energy bandgap, E_T, and the capture cross-section, σ, and assuming that the recombination lifetime is less than the mean trap emission time yields the following trap-limited decay time[69]:

$$\tau = \frac{e^{(E_C - E_T)/kT}}{\sigma N_C v_{th}} \tag{5.18}$$

where k is the Boltzmann constant, T is the absolute temperature, N_C is the effective density of states in the conduction band, E_C is the energy at the bottom of the conduction band, and v_{th} is the thermal velocity of the carrier. By accounting for the T^2 dependence of the N_C and v_{th} product, the temperature dependence of the decay time can be fit to give values for E_T and σ.

5.2. Commercial and In-House Grown GaSb

Bulk GaSb can be used as the active layer in a diffused-junction. The performance of the device formed in this case depends on the properties of the substrate material. In this section, GaSb grown by the vertical Bridgman technique[70,71] is compared to that which is commercially available.

5.2.1. Separation of Surface and Bulk Recombination

The decay transient from a 500 μm thick Firebird® p-type GaSb substrate at 1.5 mJ pulse energy is shown in Figures 5.6 and 5.7 on a linear and log scale, respectively, at 1064

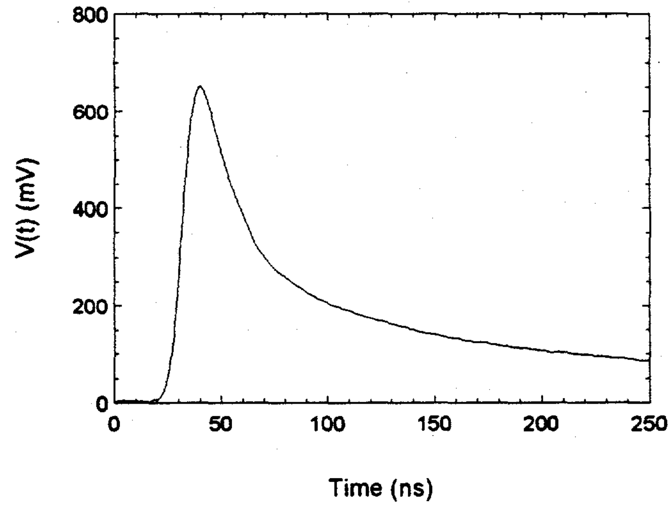

FIGURE 5.6 Decay Transient from Commercial p-GaSb Substrate at 1064 nm on a Linear Scale

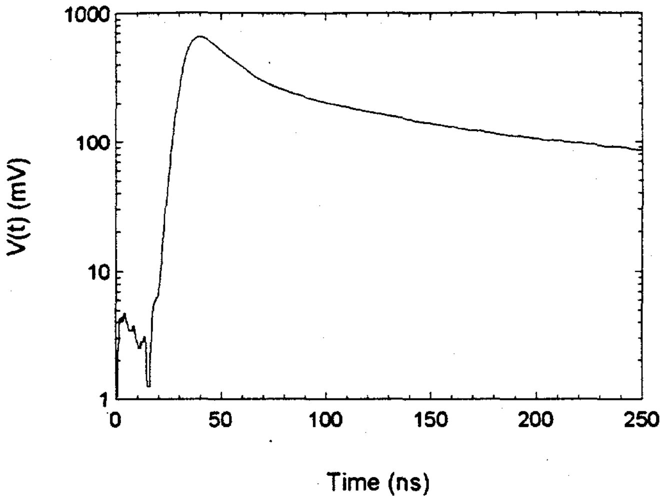

FIGURE 5.7 Decay Transient from Commercial p-GaSb Substrate at 1064 nm on a Log Scale

nm. Similarly, the data at 532 nm is shown in Figures 5.8 and 5.9. Compared to the decay transient typical of the epitaxial layers (Figure 3.10), the initial decay does not appear to be exponential over as long a time, but in each case a long exponential tail is evident. Plotting the transients at wavelengths of 1064 nm, 532 nm, and 266 nm at approximately the same excitation levels as described in Equations (5.11) and (5.12) yields the results shown in Figure 5.10. The initial portion of the decay is neglected according to the simulation results;

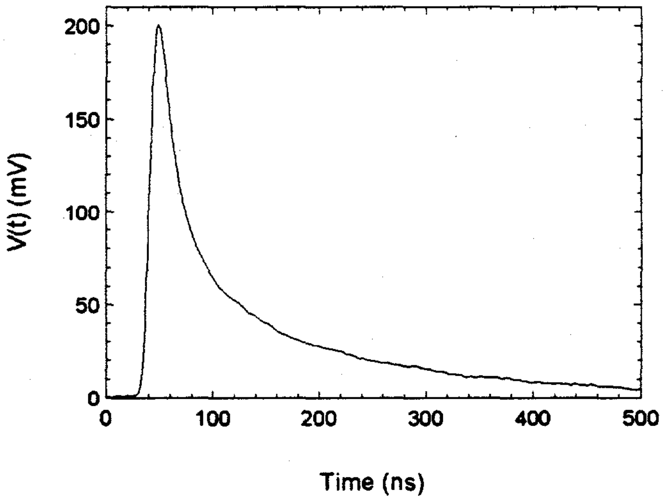

FIGURE 5.8 Decay Transient from Commercial p-GaSb Substrate at 532 nm on a Linear Scale

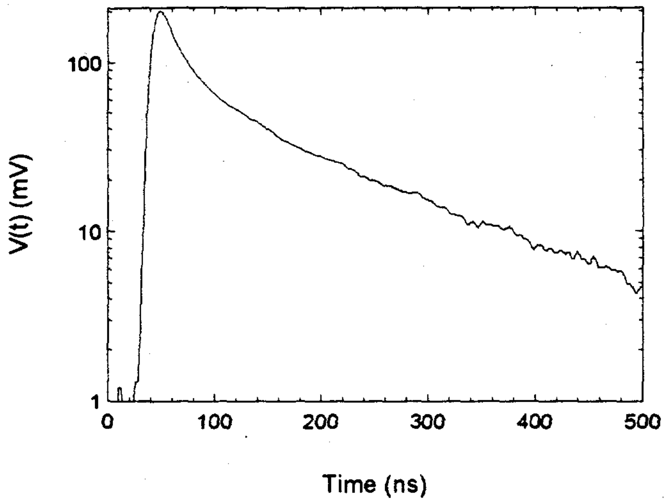

FIGURE 5.9 Decay Transient from Commercial p-GaSb Substrate at 532 nm on a Log Scale

therefore the analysis is conducted on the linear portion >20 ns from the transient peak. The slopes of the least-squares fit lines yield values of 38, 72, and 140 ns for the bulk lifetime measured with 1064 nm, 532 nm, and 266 nm light, respectively. The apparent dependence of bulk lifetime on wavelength is not presently understood. The pulse energy was 0.083 mJ at 1064 nm (IR), 0.13 mJ at 532 nm (GR), and 0.51 mJ at 266 nm (UV), which corresponds to 9.8×10^{14}, 6.4×10^{14}, and 8.9×10^{14} photons/cm² absorbed in an area 6 mm in diameter, respectively. In determining the excitation level, the wavelength dependent reflection coefficient must be used. Using experimentally obtained[72] values of α and n, the extinction coefficient (k) and the reflection coefficient (listed in Table 5.1 for each wavelength) are determined using the following relations[73]:

$$k=\frac{\alpha c}{2\omega} \quad \text{and} \quad R=\frac{(n-1)^2+k^2}{(n+1)^2+k^2} \quad . \tag{5.19}$$

Using the values for N_{ph} given above, the corrected y-intercepts of the fit lines (using Figure 5.12), and assuming an electron mobility of 1000 cm²/V·s (i.e., D_n=26 cm²/s) the

Table 5.1 Optical Constants for GaSb

Wavelength (nm)	α (cm^{-1})*	n*	*k*	*R*
1064	3.12×10^4	4.198	0.264	0.380
532	4.85×10^5	4.499	2.05	0.477
266	1.51×10^6	1.556	3.20	0.628

* Taken from Palik, "Handbook of Optical Constants of Solids", Ref [72]

values for SRV are obtained using the experimentally obtained absorption constants given in Table 5.1 and the following expression obtained by solving Equation (5.12) for pairs of values of α, N_{ph}, and y-intercept:

$$S_R = \frac{\alpha_1\alpha_2 D_n (N_{ph2}e^{B_1} - N_{ph1}e^{B_2})}{\alpha_2 N_{ph1}e^{B_2} - \alpha_1 N_{ph2}e^{B_1}} \tag{5.20}$$

where α_1 and α_2 are the two absorption constants, B_1 and B_2 are the corresponding y-intercepts of the fit lines, and N_{ph1} and N_{ph2} the corresponding photons/pulse and listed in

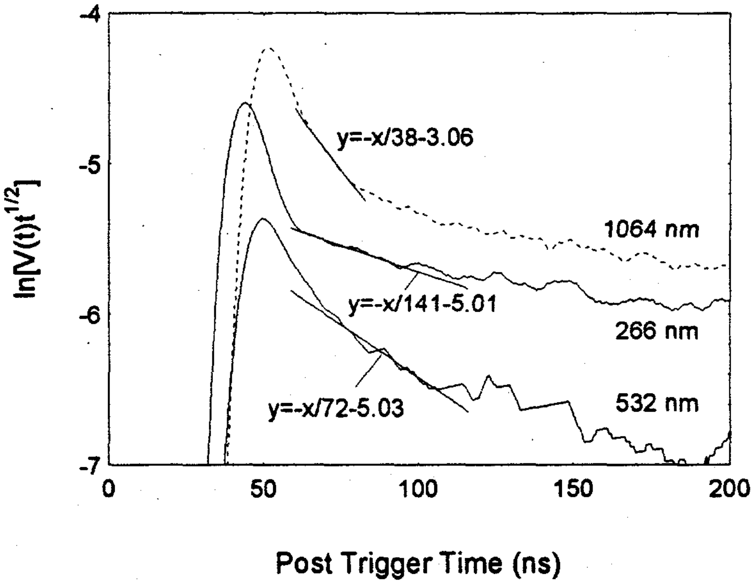

FIGURE 5.10 Transformed Decay Transients from Commercial p-GaSb Substrate at Different Wavelengths

Table 5.2, where the errors reported were calculated using Equation (5.13) based upon the error in B from the least-squares fitting. From the data using the three wavelength pairs, the SRV in p-type unpassivated GaSb substrates is approximately 2×10^6 cm/s. The agreement in SRV between the three pairs of excitation wavelength is good, but also increases the concern for the different values of bulk lifetime described previously.

Table 5.2 Extracted SRV for Commercial p-type GaSb

Wavelengths Used	Calculated SRV (cm/s)	Conversion Factor (mV·cm^2)
IR-GR	$(1.8\pm0.1)\times10^6$	3.6×10^{-12}
GR-UV	$(2.1\pm0.1)\times10^6$	4.2×10^{-12}
IR-UV	$(1.9\pm0.2)\times10^6$	3.7×10^{-12}

Since Equation (5.11) is derived for the density of photogenerated carriers (cm^{-2}), a multiplicative constant is used to convert the expression to mV in the preceding analysis and is solved for along with the SRV. The origin of the constant is the responsivity of the RF photoreflectance system, which is determined by the DC conductivity of the sample. The equilibrium carrier concentration integrated over the thickness of the sample (the integration can be taken to ∞ since $1/\alpha$ is generally much less than the RF skin depth and the substrate thickness) along with the mobility determines the DC conductivity. Thus, for a given sample at a fixed injection level, the responsivity is constant. For example, assuming a p-type sample with $\mu_{n,p}$=1000 cm^2/V·s, p_0=5×10^{16} cm^{-3}, and thickness d=0.05 cm gives R_S=2.5 Ω/□. A first-order Taylor expansion of R_S yields

$$\Delta R_S = -\frac{\mu_n N_{ph}}{q\mu_p^2 p_0^2 d^2} = 10^{-15} N_{ph} \tag{5.21}$$

for the change in sheet resistance after the optical excitation. The change in sample sheet resistance is transformed by a factor of ~4.43 by the probe card according to Figure 3.9. The change in the transformed impedance (ΔZ) is detected as a change in reflection coefficient ($\Delta\Gamma$) using

$$\Gamma = \frac{Z - Z_0}{Z + Z_0} \Rightarrow \Delta\Gamma \approx \frac{2Z_0}{\left(Z + Z_0\right)^2}\Delta Z = 0.028\Delta Z = 1.2 \times 10^{-16} N_{ph} \quad , \qquad (5.22)$$

where Z_0 is the system impedance (50 Ω). Finally, accounting for the gains in the two signal amplifiers (25 dB+21 dB=46 dB) and the losses in the directional coupler and mixer conversion (-6 dB-6.9 dB= -12.9 dB) gives a conversion factor of 5.4×10^{-12} mV·cm^2 which is on the same order of magnitude as the values calculated from the commercial GaSb substrate.

The SRV result is linearly dependent on the diffusion constant; therefore, the accuracy of the SRV is limited by the accuracy of the value used for D_n. In addition, when the absorption constants differ by more than an order of magnitude (i.e., $\alpha_2 >> \alpha_1$) with similar values of N_{ph} and y-intercept, the SRV obtained from Equation 5.20 loses sensitivity to the value of α_2. The result is a minimum SRV, $S_{R,\min}$, that can be determined, given by

$$S_{R,\min} \rightarrow \frac{\alpha_1 D_n (N_{ph2} e^{B_1} - N_{ph1} e^{B_2})}{N_{ph1} e^{B_2}} \quad . \qquad (5.23)$$

In the remainder of this chapter, the decay transients presented are transformed as in Figure 5.10. The raw decay transients for each sample can be found in Appendix E.

5.2.2. Bulk Recombination

By plotting the bulk lifetime as the pulse energy (i.e., injection level) is varied, the dominant mode of bulk recombination is revealed for substrates. Figure 5.11 shows the transients from the p-type GaSb sample where the laser intensity at 1064 nm has been varied using a set of neutral density filters. Similar data taken at 532 nm and 266 nm are shown in Figures 5.12 and 5.13, respectively; although at 266 nm the optics used limit the maximum pulse energy to 0.51 mJ impinging on the sample.

From the slopes of the fit lines at 1064 nm (Figure 5.11) and using Equation 5.11, the bulk lifetime generally increases as the pulse energy is increased. This behavior is typical of SRH recombination that is characterized by longer lifetimes in high-level injection. The bulk lifetimes measured at 532 nm (Figure 5.12) also increase with intensity. However, at 266 nm (Figure 5.13) the lifetime appears to decrease with increasing excitation up to 0.26 mJ pulse energy.

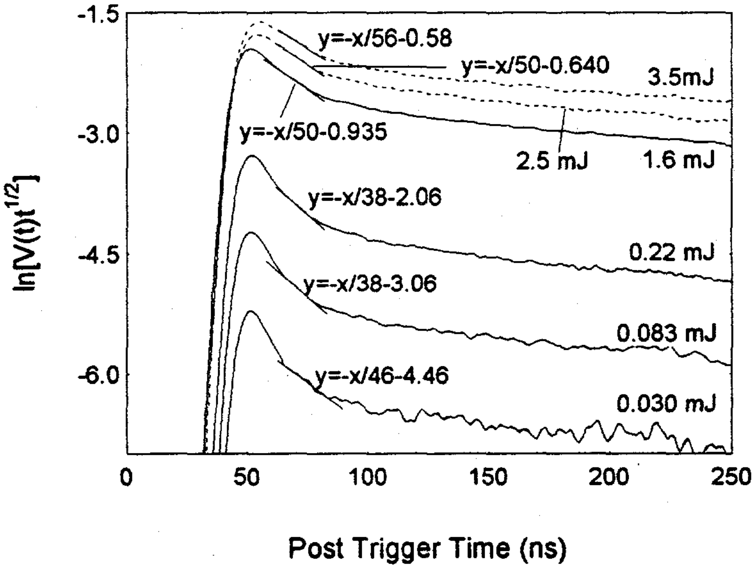

FIGURE 5.11 Transformed Decay Transients from Commercial p-GaSb for Different Intensities at 1064 nm

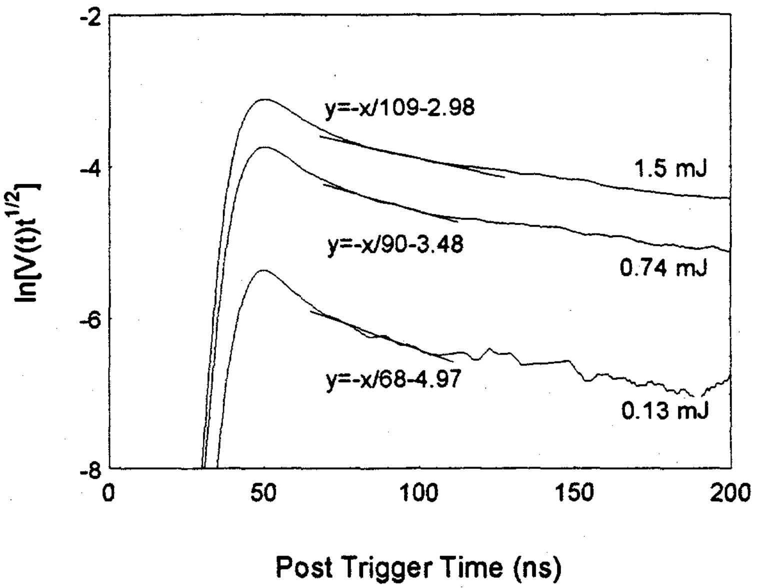

FIGURE 5.12 Transformed Decay Transient from Commercial p-GaSb for Different Intensities at 532 nm

The decay transients from p-type GaSb ($p=1.9\times10^{17}$ cm^{-3}) grown in-house by the vertical Bridgman process are shown in Figure 5.14 at 1064 nm with the optical pulse energy varied as above. The bulk lifetimes for the GaSb substrates are plotted versus injection level

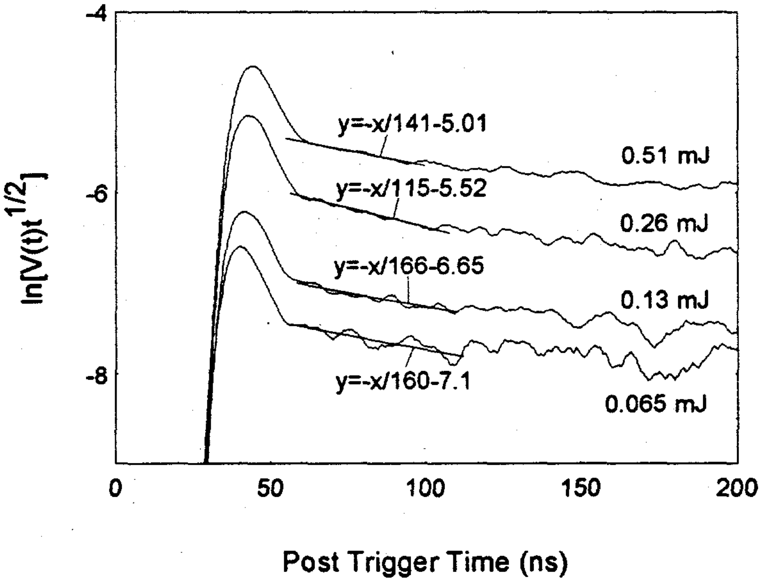

FIGURE 5.13 Transformed Decay Transients from Commercial p-GaSb for Different Intensities at 266 nm

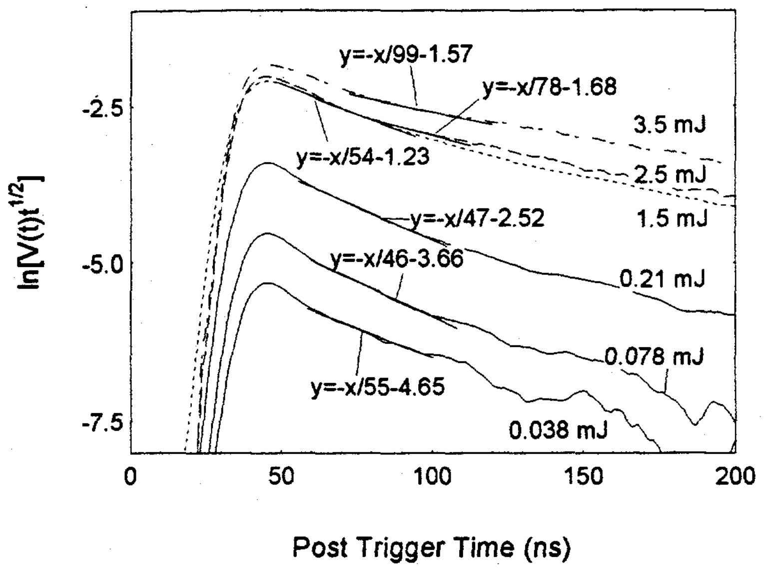

FIGURE 5.14 Transformed Decay Transients from In-house p-GaSb for Different Intensities at 1064 nm

relative to 3.5 mJ at 1064 nm in Figure 5.15. At 1064 nm the bulk lifetime of the in-house grown GaSb substrate and the commercial GaSb substrate exhibits SRH recombination. At 532 nm SRH recombination is also dominant in the commercial GaSb substrate. The 266 nm recombination mechanism is not understood at present.

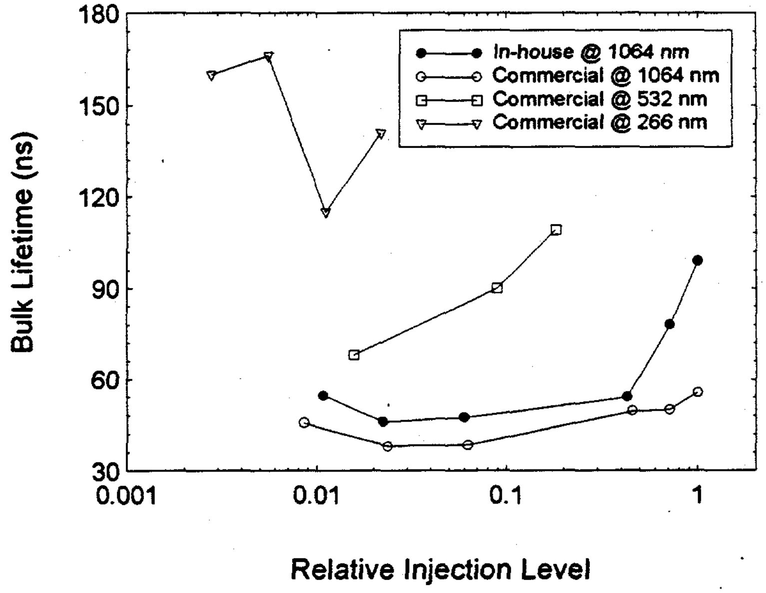

FIGURE 5.15 Bulk Lifetime of GaSb Substrates at Different Injection Levels Relative to 3.5 mJ at 1064 nm

5.2.3. Temperature Measurements

Since the RF photoreflectance system depends on the inductive coupling between the probe coil and the sample, only low-loss insulating materials can be in the vicinity of the sample or probe coil for proper operation. In order to take measurements at other temperatures while not changing the operating temperature of the probe card and coil, the sample is placed on a quartz block immersed in a temperature reservoir.

The decay transients for the commercial p-type GaSb sample are compared at room temperature (300 K) and liquid nitrogen temperature (77 K) at an optical pulse energy of 2.1 mJ in Figure 5.16. The initial decay time (bulk lifetime) increases from 51 ns to 72 ns, while the long decay decreases from 370 ns to 330 ns when the sample is cooled from room temperature to 77 K. Since trap capture rates increase with temperature, the long decay time is not consistent with a trapping process. Auger recombination can also be eliminated as a dominant mode of bulk recombination since from Equation (2.36) τ_A increases with

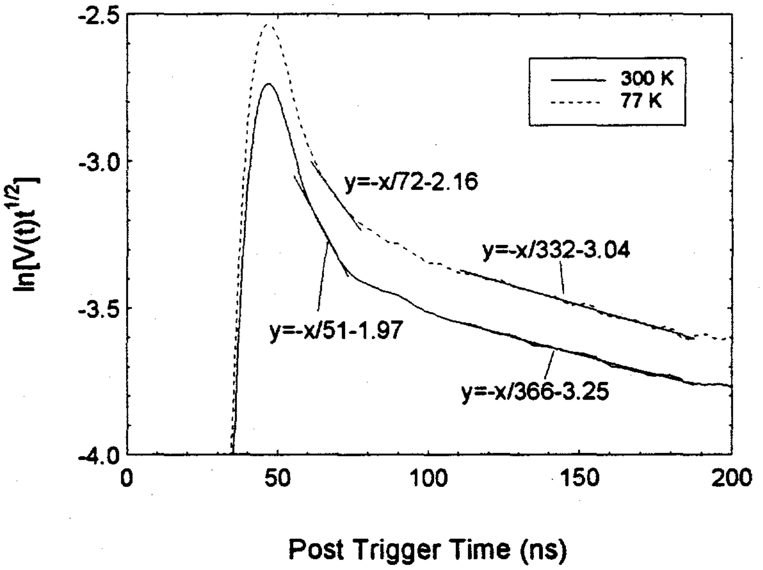

FIGURE 5.16 Transformed Decay Transients from Commercial p-GaSb for Different Temperatures at 1064 nm

temperature by more than a factor of seven over the temperature range considered. Thus, either radiative or SRH recombination dominates the bulk recombination at low temperatures since recombination of non-degenerate electrons and holes at the band edge has a $T^{-3/2}$ temperature dependence[74] and SRH recombination has a $T^{-1/2}$ dependence.

The difference in corrected y-intercepts calculated from the values for the initial decays in Figure 5.16 (-5.0 versus -5.2) is due to the temperature dependence of α, D_n, the reflectivity (which determines N_{ph} absorbed), and S_R. In the commercial GaSb sample αD_n was found to be a factor of approximately 0.39 of the S_R extracted at room temperature. While the mobility generally increases by a factor of 2 or 3 at low temperatures α can decrease by orders of magnitude at low temperatures. Under this condition, the y-intercept reduces to $N_{ph}/(\alpha^2\pi D_n)^{1/2}$ which is dominated by the thermal dependence of α. Hence, the y-intercept is expected to increase as the temperature decreases, in agreement with the long decay. However, the decrease observed requires nearly constant α (consistent with the 5% change in E_g) and an order of magnitude increase in S_R.

5.3. Quasi-Binary InGaAsSb

Since the diffused junction process is a lower cost alternative to epitaxially grown junctions, substrates with bandgaps in the range of 0.5 to 0.55 eV are desirable in order to achieve maximum utilization of the radiation spectrum produced by low-temperature (1000-1500 K) combustion sources. The in-house grown $(GaSb)_x(InAs)_y$ quasi-binary substrates used in this section were grown from GaSb and InAs sources by the same vertical Bridgman process used in the growth of the in-house GaSb substrate of the preceding section, and are the starting material used in the fabrication of diffused junction TPV devices.

5.3.1. Separation of Surface and Bulk Recombination

The decay transients from a small (~5 mm) single-crystal 5.4×10^{16} cm^{-3} Te-doped (n-type) 0.55 eV quasi-binary substrate mined from a large-grain polycrystalline boule at 0.11 mJ (1064 nm) and 0.26 mJ (532 nm) are shown in Figure 5.17. The bulk lifetime of the sample decreases from 17 ns at 1064 nm to 12 ns at 532 nm. Using the corrected y-intercepts from the fit lines and a mobility of 1000 cm^2/V·s, the SRV is $(2.2\pm1.4)\times10^6$ cm/s. The absorption constants used are taken from the experimental data[72] of GaSb, InSb, GaAs, and InAs (listed in Appendix D) linearly interpolated taking into account the most significant critical point due to the bandgap to obtain the absorption constant for the quasi-binary for each bandgap. The composition is computed by solving the following equation[75] for the

Table 5.3 Absorption Constant and Reflectivity for Binaries and Quasi-binaries

	1064 nm		532 nm	
	α (cm^{-1})	R	α (cm^{-1})	R
GaAs	<10*	0.307	$7.85\times10^{4*}$	0.578
GaSb	$3.12\times10^{4*}$	0.380	$4.85\times10^{5*}$	0.477
InAs	$2.43\times10^{4*}$	0.321	$1.35\times10^{5*}$	0.406
InSb	$3.70\times10^{4*}$	0.383	$5.26\times10^{5*}$	0.465
0.62 eV $(GaSb)_{0.92}(InAs)_{0.08}$	2.93×10^4	0.375	4.57×10^5	0.467
0.60 eV $(GaSb)_{0.91}(InAs)_{0.09}$	2.90×10^4	0.374	4.51×10^5	0.465
0.55 eV $(GaSb)_{0.86}(InAs)_{0.14}$	2.80×10^4	0.371	4.34×10^5	0.459
0.40 eV $(GaSb)_{0.66}(InAs)_{0.34}$	2.47×10^4	0.359	3.64×10^5	0.435

*Taken from Palik, "Handbook of Optical Constants of Solids", Ref [72]

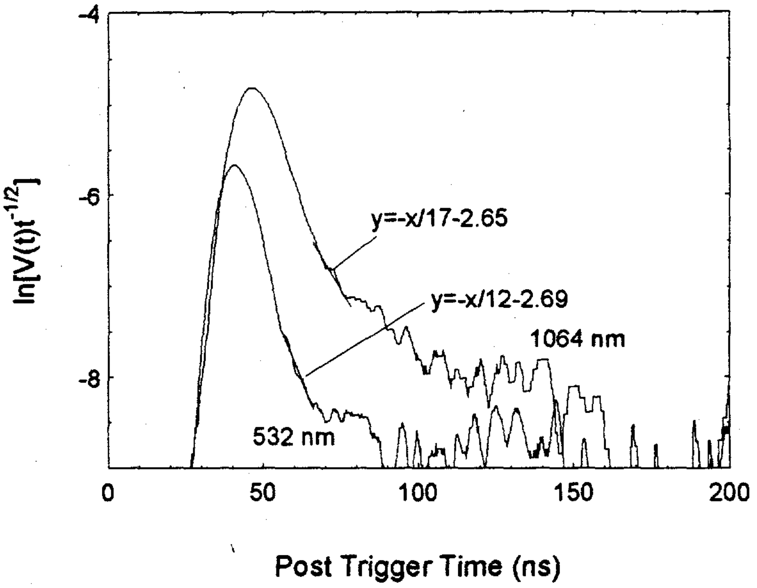

FIGURE 5.17 Transformed Decay Transients from 0.55 eV n-type Quasi-binary Substrate at Different Wavelengths

requisite bandgap energy:

$$E_g(x) = 0.5990x^3 - 0.09677x^2 - 0.1386x + 0.3600 \quad . \tag{5.23}$$

The interpolated absorption constants and calculated reflectivities are listed in Table 5.3 for the three quasi-binaries used in this section as well as for the four constituent binaries taken from Palik[72].

The data from a 0.60 eV n-type (4×10^{17} cm^{-3}) polycrystalline quasi-binary substrate grown at 950 °C with 10% InAs in the melt is shown in Figure 5.18 at 0.078 mJ (1064 nm) and 0.13 mJ (532 nm). The values for absorption constant are derived in the same manner as for the previous sample. The slopes of the fit lines give bulk lifetimes of 59 ns and 29 ns at 1064 nm and 532 nm, respectively, and an SRV of $(2.3\pm0.3)\times10^6$ cm/s. The SRV is in the expected range for unpassivated n-type substrates.

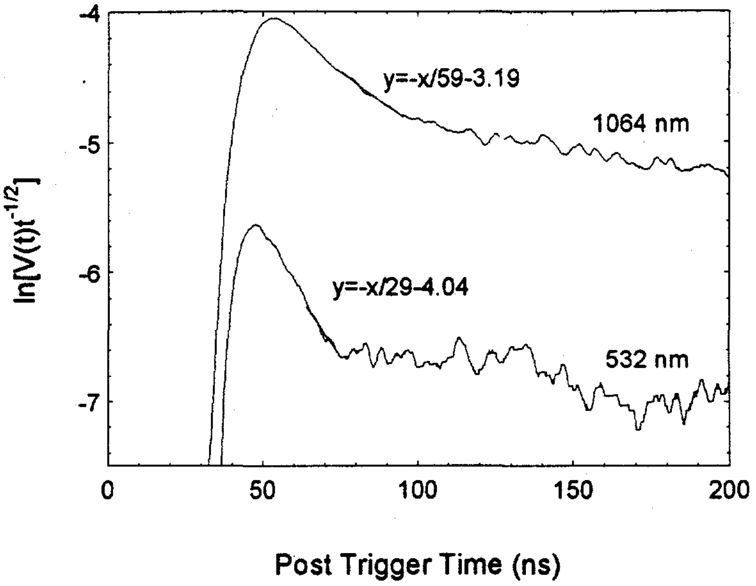

FIGURE 5.18 Transformed Decay Transient from 0.60 eV Quasi-binary Substrate at Different Wavelengths

The data from a 0.62 eV n-type (3×10^{17} cm^{-3}) polycrystalline quasi-binary substrate grown at 720 °C with 3% InAs in the melt is shown in Figure 5.19 at the same pulse energies and wavelengths as for the previous sample. The slopes of the least-squares fit lines

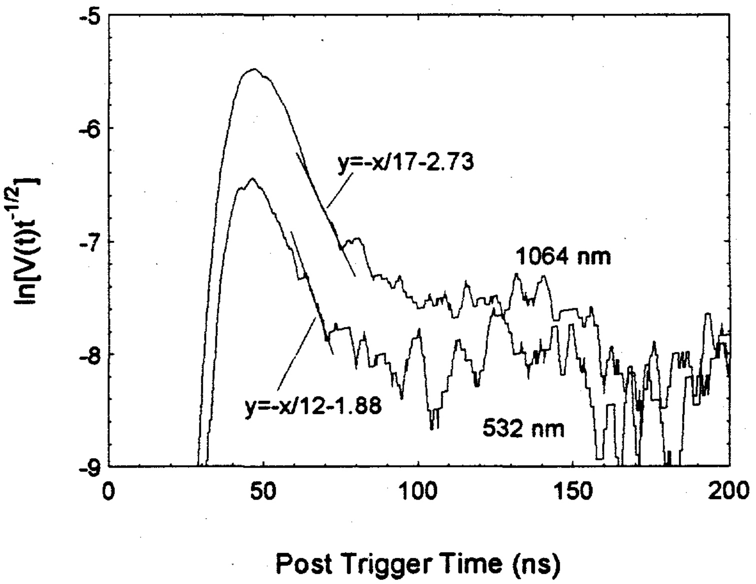

FIGURE 5.19 Transformed Decay Transients from 0.62 eV n-type Quasi-binary Substrate at Different Wavelengths

yield bulk lifetimes of 17 ns and 12 ns, respectively; however, using the corrected y-intercepts, an SRV of $(-1.0\pm1.7)\times10^5$ cm/s is obtained. The negative value and large error obtained for the SRV are due to the relatively noisy transient that, combined with the short bulk lifetime, produces a large uncertainty in y-intercept. However, from a qualitative view, since this sample is GaSb-rich the surface is expected to have the Fermi level pinned at the valence band. The surface field thus created should attract holes and enhance surface recombination, thereby reducing the carrier concentration and producing the noisier decay.

The results from the dual wavelength measurements of SRV on quasi-binary substrates are summarized in Table 5.4. With the exception of the 0.62 eV sample, the unpassivated n-type quasi-binary samples have an SRV on the order of 2×10^6 cm/s. The values of $S_{R,\min}$ for the 0.55 eV and 0.60 eV samples are 1.7×10^6 and 1.8×10^6 cm/s. Since these values are close to those listed in Table 5.4, the large difference in absorption constant resulting from the optical wavelengths used is limiting the SRV resolution.

Table 5.4 Extracted SRV for n-type Quasi-binary Substrates

Sample	Bandgap (eV)	Calculated SRV (cm/s)	Conversion Factor (mV·cm²)
CZ2	0.55	$(2.2\pm1.4)\times10^6$	1.1×10^{-12}
IGAS2	0.60	$(2.3\pm0.3)\times10^6$	5.0×10^{-12}
IGAS1	0.62	$-(1.0\pm1.7)\times10^5$*	-3.0×10^{-13}*

*Due to noisy signal

5.3.2. Bulk Recombination

The decay transients from the 0.55 eV single-crystal quasi-binary substrate are shown in Figure 5.20 at 1064 nm with the optical pulse energy varying from 0.042 mJ to 3.5 mJ.

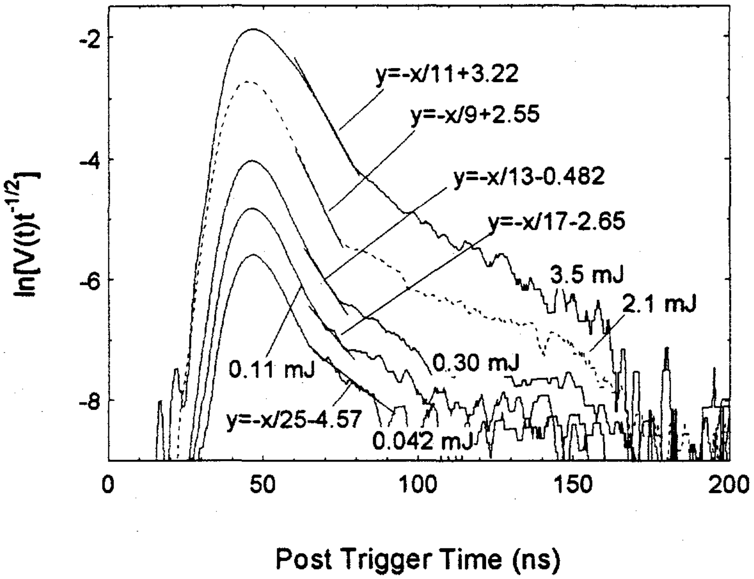

FIGURE 5.20 Transformed Decay Transients from 0.55 eV n-type Quasi-binary Substrate as a Function of Pulse Energy at 1064 nm

At the higher pulse energies, the slope of the transient is nearly constant while at the lower energies the bulk lifetime varies inversely. The bulk lifetimes and long decay times are plotted in Figure 5.21 showing the intensity dependence on a log-log scale. The bulk lifetime and the long decay time both exhibit an inverse power-law dependence between that of $x^{1/3}$ and $x^{1/2}$.

An undoped n-type single-crystal quasi-binary substrate was prepared similarly to the above sample, but with an InAs-rich melt resulting in a bandgap of 0.40 eV having a carrier concentration of 1×10^{16} cm^{-3} measured at room temperature. The transformed decay transients at 1064 nm wavelength are shown in Figure 5.22, and the bulk lifetimes extracted from their slopes are shown in Figure 5.23 as a function of pulse energy plotted on a log-log scale. At low intensity, the bulk lifetime is relatively independent of excitation, typical of SRH. At higher intensities the bulk lifetime decreases with excitation level which is consistent with either radiative or Auger recombination, as shown in Figure 5.23. Although a power-

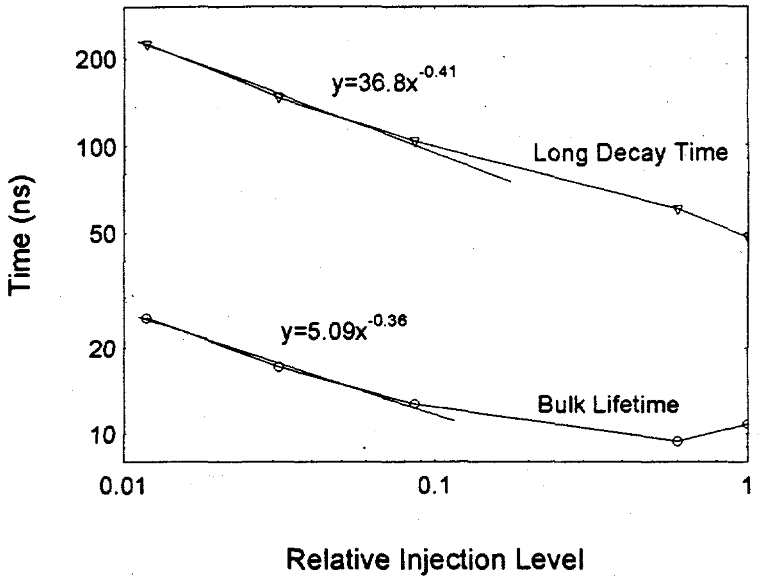

FIGURE 5.21 Bulk Lifetime and Long Decay Time for 0.55 eV n-type Quasi-binary Substrate Dependence on Injection Level Relative to 3.5 mJ at 1064 nm

law fit at high intensity results in the bulk lifetime being inversely proportional to the pulse energy raised to approximately the 1/3 power. This dependence is in between what is

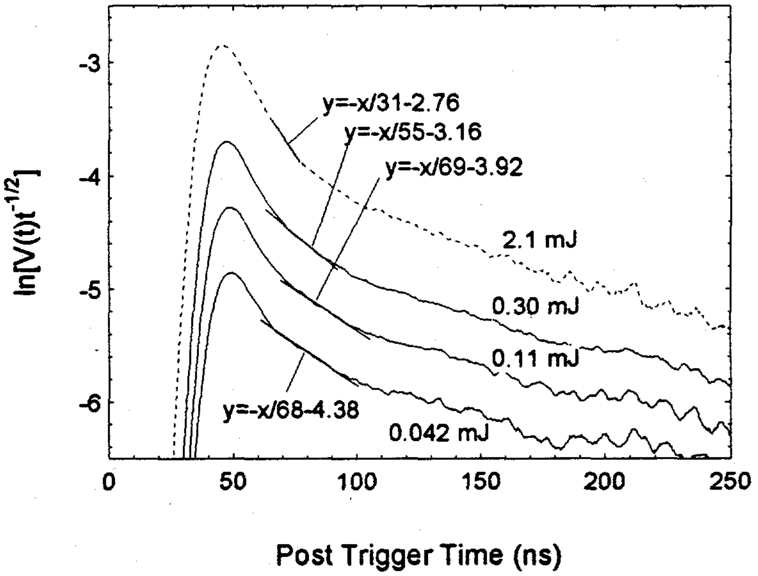

FIGURE 5.22 Transformed Decay Transients from 0.40 eV n-type Quasi-binary Substrate for Different Intensities at 1064 nm

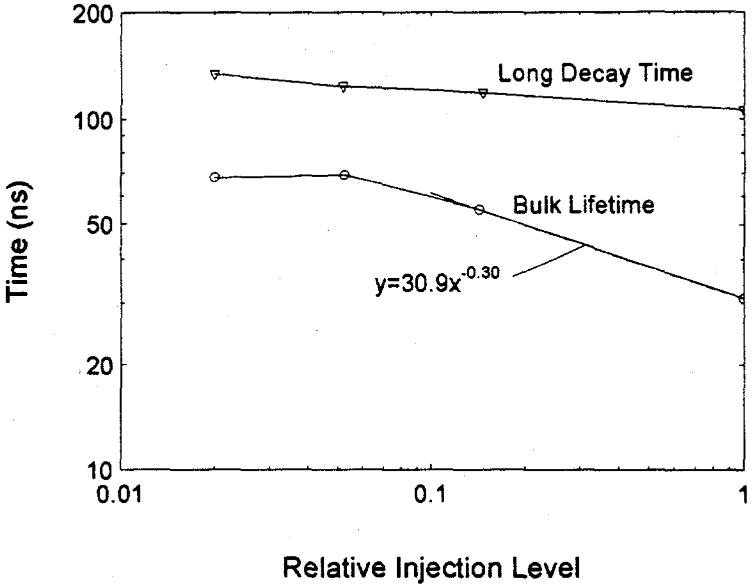

FIGURE 5.23 Bulk Lifetime and Long Decay Time of 0.40 eV n-type Quasi-binary Substrate Dependence on Injection Level Relative to 2.1 mJ

expected for SRH and radiative recombination (n^{-1}), and can be interpreted as being in the transition from SRH to radiative recombination. Higher intensity data is required to confirm this conclusion.

The transformed decay transients from the p-type 0.62 eV polycrystalline quasi-binary substrate grown at 720 °C as the pulse energy is varied from 0.03 mJ up to 1.5 mJ are shown in Figure 5.24. The bulk lifetime of the sample, shown in Figure 5.25, decreases from 36 ns to 25 ns as the pulse energy increases, indicating that radiative or Auger recombination is the dominant recombination process, while the long decay shows a four-fold decrease. The transformed decay transients from the 0.60 eV n-type polycrystalline quasi-binary substrate grown at 950 °C are shown in Figure 5.26 over the same pulse energy range. The bulk lifetime increases with increasing pulse energy characteristic of SRH recombination, and the long decay time has an inverse dependence as shown in Figure 5.27 on a log-log plot.

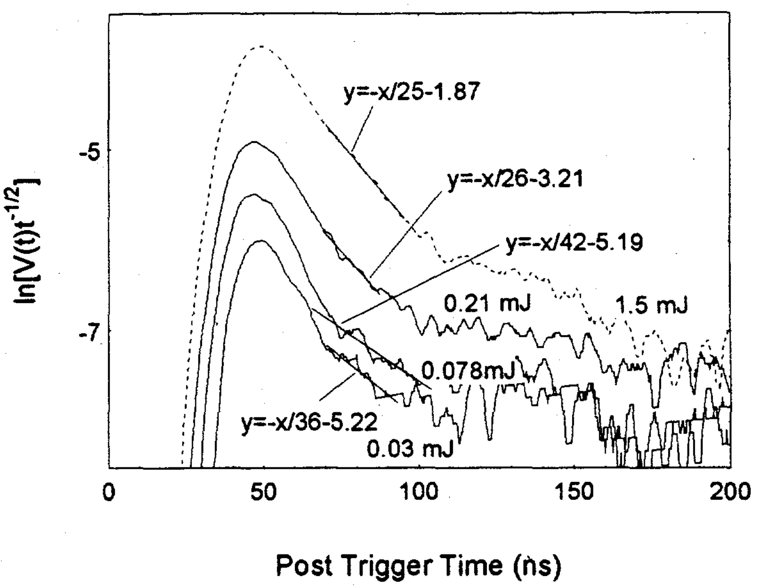

FIGURE 5.24 Transformed Decay Transients from 0.62 eV n-type Quasi-binary Substrate for Different Pulse Energies

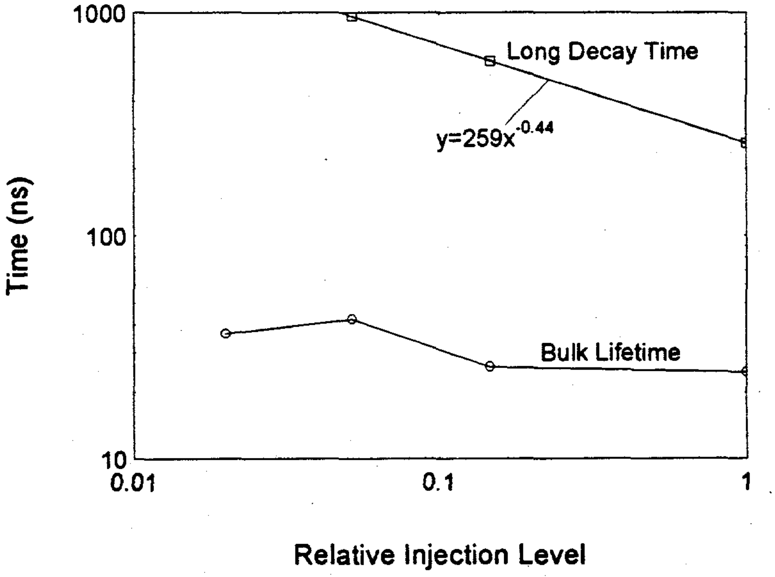

FIGURE 5.25 Bulk Lifetime and Long Decay Time of 0.62 eV n-type Quasi-binary Substrate Dependence on Injection Level Relative to 1.5 mJ

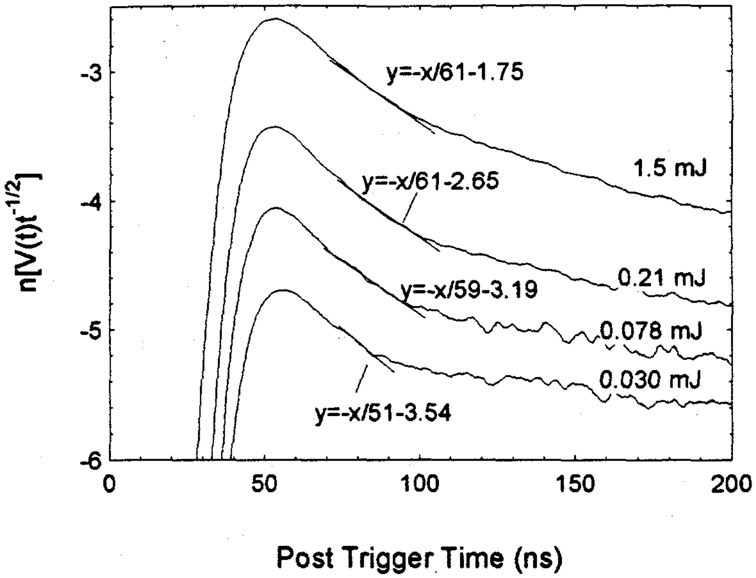

FIGURE 5.26 Transformed Decay Transients from 0.60 eV n-type Quasi-binary Substrate for Different Pulse Energies

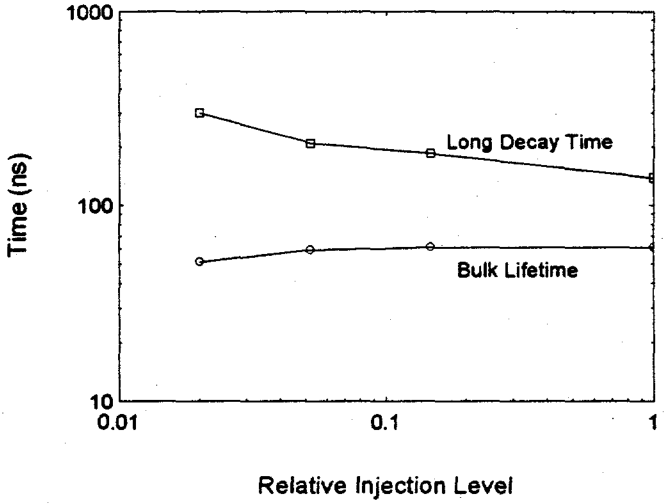

FIGURE 5.27 Bulk Lifetime and Long Decay Time of 0.60 eV n-type Quasi-binary Substrate Dependence on Injection Level Relative to 1.5 mJ

5.3.3. Temperature Measurements

The decay transients of the quasi-binary substrates were measured at room temperature and immersed in a LN_2 bath at 77 K, as was done with the GaSb substrate (section 5.2.3). The transformed decays for the 0.55 eV quasi-binary substrate are shown in Figure 5.28 at 77 K and 300 K with a 3.65 mJ 1064 nm excitation. The bulk lifetime increases from 22 ns at room temperature to 73 ns at 77 K. A similar increase is observed in the 0.60 eV and 0.62 eV quasi-binaries as well. The $T^{-3/2}$ dependence of radiative recombination implies that the bulk lifetime should increase by more than a factor of 7. Auger recombination has a $T^{3/2}e^{-E_m/kT}$ dependence[76], where $E_m=[\zeta/(1+\zeta)]E_g \sim 0.09E_g$ is the Auger threshold energy, and thus decreases with decreasing temperature. The $T^{-1/2}$ dependence of SRH recombination implies that the bulk lifetime should double.

Using a model that combines the temperature dependences of radiative and SRH

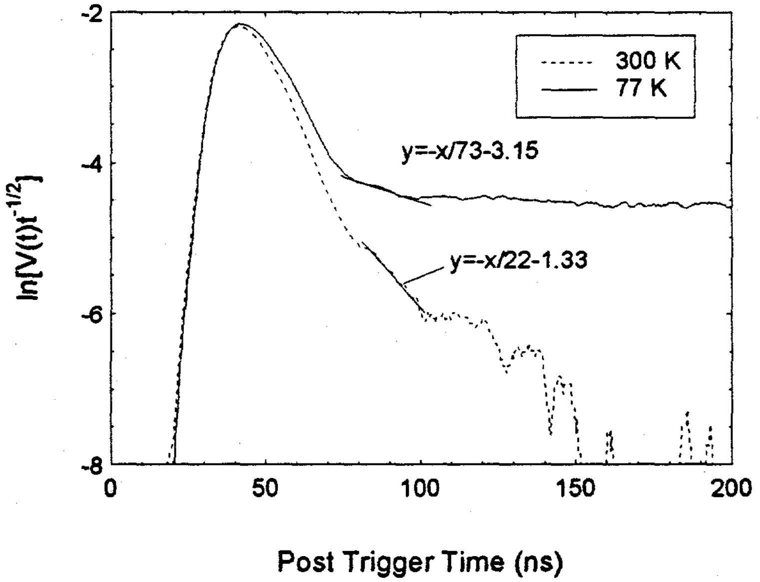

FIGURE 5.28 Transformed Decay Transients from 0.55 eV n-type Quasi-binary Substrate at 1064 nm for Different Temperatures at 3.65 mJ

recombination as follows:

$$\frac{1}{\tau_{eff}(T)} = \frac{1}{AT^{-1/2}} + \frac{1}{BT^{-3/2}} \quad ,$$

the measured bulk lifetimes can be used to determine the fitting parameters *A* and *B*. Using the bulk lifetimes given above yield radiative and SRH lifetimes of 40 ns and 70 ns at room temperature, and 300 ns and 130 ns at 77 K, respectively, for the IGAS1 and IGAS2 samples. Therefore, the observed change in bulk lifetime is dominated by radiative recombination (in agreement with the results of the intensity variation at room temperature in the preceding section) with SRH recombination becoming dominant at lower temperatures. For the CZ2 sample, similar radiative lifetimes were obtained at each temperature, but the SRH lifetimes were 50 ns and 100 ns at room temperature and 77 K, respectively. While only two temperature measurements were used in the above analysis, the results serve to demonstrate the usefulness of the temperature profiling of bulk lifetime. Measurements at additional temperatures would permit more complete evaluation of the various modes of bulk recombination.

The results of the measurements are summarized in Table 5.5. In each case the long

Table 5.5 Long Decay Time and Bulk Lifetime of n-type Quasi-binary Substrates versus Temperature at 3.65 mJ Optical Pulse Energy

Sample	Bandgap (eV)	Long Decay Time (ns)		Bulk Lifetime (ns)	
		77 K	300 K	77 K	300 K
CZ2	0.55	483	284	73	22
IGAS2	0.62	2380	971	92	24
IGAS1	0.60	2950	1580	90	24

decay time approximately doubles as the temperature decreases. The change in decay time is too small to fit a trap model, but due to the $T^{-1/2}$ dependence can be attributed to SRH recombination.

5.4. Summary

An analysis applicable for substrates has been presented that permits the determination of surface recombination velocities and bulk lifetimes as low as 10 ns. By illuminating the samples with light of different wavelengths, and hence different absorption depths, the generated carriers recombine with different surface lifetime components, thereby allowing separation of the surface recombination velocity (SRV) from bulk lifetime. Due to the order of magnitude difference in absorption depth from the wavelengths used, the minimum SRV value obtainable from this analysis is on the order of 10^5 cm/s. A qualitative treatment of bulk lifetime dependence on injection level and temperature was presented that permits determination of the dominant mode of bulk recombination.

An SRV of 2×10^6 cm/s was obtained from commercially available unpassivated p-type GaSb using wavelengths of 1064 nm, 532 nm, and 266 nm. The bulk lifetime exhibited a wavelength dependence, increasing from 40 ns at 1064 nm to 140 ns at 266 nm, which is presently not understood. A similar value of bulk lifetime was obtained with an in-house grown unpassivated p-type GaSb sample at 1064 nm. Injection level dependence of the bulk lifetime indicated that SRH recombination dominates at room temperature in the commercial sample as well as in the in-house grown sample. At 77 K either radiative or SRH recombination appears to dominate, although measurements at additional temperature are required to make the determination quantitatively. The dependence of the y-intercept with temperature suggests that the SRV increases by over an order of magnitude at 77 K. While the SRV value obtained is much higher than that for the capped OMVPE InGaAsSb samples, since diffused junctions are generally shallow, the high front surface SRV does not significantly impact TPV performance.

Unpassivated n-type quasi-binary InGaAsSb substrates having bandgaps of 0.55, 0.60, and 0.62 eV were measured at 1064 nm and 532 nm resulting in an SRV of approximately 2×10^6 cm/s, similar to that obtained with the commercial p-type GaSb sample, and bulk lifetimes ranging from 25 to 50 ns. Since the substrates are GaSb-rich, band-bending present at the surface creates an attractive field that enhances the effect of surface states on surface recombination. The 0.62 eV sample had the lowest concentration of InAs and therefore the maximum band-bending. This resulted in a higher SRV that reduced the transient amplitude, and led to the noisy signal observed. Since similar SRVs were obtained with the n-type quasi-binary and p-type GaSb samples despite the attractive field of the quasi-binary, the quasi-binary surface is possibly as good as or better than that of commercially available epi-ready GaSb. The injection level dependence revealed that SRH recombination dominates at the lower injection levels becoming radiative-dominated at the higher injection levels for the 0.40 and 0.55 eV samples, while the 0.60 eV sample exhibited SRH-dominated recombination over the range of injection level used. The injection level dependence for the 0.62 eV sample is attributed to either radiative or Auger recombination. In each case, the temperature dependence suggested that SRH recombination dominates at 77 K.

The long decay present in each case doubles as the temperature decreases from room temperature to 77 K, but does not fit the temperature dependence of a trap model. However, the temperature dependence agrees well with that of SRH recombination.

The quasi-binary substrates were found to have similar values of SRV and bulk lifetimes as the epi-ready commercial and in-house GaSb samples. While the bulk recombination mechanism was found to be SRH dominated in both sets of samples at the lower injection levels, radiative and possibly Auger recombination generally dominated the bulk lifetime in the quasi-binary samples at the higher injection levels. Since SRH typically dominates bulk recombination in highly defected material, the absence of SRH recombination in the quasi-binary samples indicates that this material is of a sufficiently high quality. The technique used to analyze these samples can be used to guide further improvements in material quality to maximize the efficiency of diffused-junction TPV devices fabricated with quasi-binary substrates.

6. Summary and Conclusions

A radio-frequency (RF) photoreflectance system was designed, developed, and evaluated as a non-contacting, non-destructive tool for the characterization of recombination processes in low bandgap semiconductors, both epitaxial thin active device layers and bulk substrates. Analysis techniques were developed based on the dependence of the decay time of photoreflectance transients on active layer thickness, injection level, wavelength, and temperature to determine the surface recombination velocity (SRV) and dominant bulk recombination mechanism. The system performance and results of its application to doubly-capped epitaxial InGaAsSb and uncapped Sb-based substrates are summarized below.

6.1. RF Photoreflectance System

The RF photoreflectance system, designed to complement the capabilities of microwave reflectance systems, is capable of determining the conductivity, SRV, and the lifetime of the dominant recombination mechanism in samples having a sheet resistance in the range of 0.1 to >12.5 Ω/□. The sensitivity on highly conducting samples is accomplished through the reduction of the operating frequency from 36 GHz to 410 MHz, thereby permitting the use of a 50 Ω system impedance, and a probe coil that maximizes coupling of the RF probe signal into the sample. The low system response time (~5 ns) is made possible through the use of a 5th-order 250 MHz Chebyshev diplexer which, by minimizing reflections, also reduces signal distortion.

Using samples with calibrated resistivities, the system demonstrated a 67 dB dynamic range in sensitivity with a linear response over two decades of resistivity. Combined with the characteristics of the laser, the system is capable of responding to decays as fast as 12 ns in thin active layers with less than 1 ns error.

6.2. Doubly-Capped OMVPE Epitaxial InGaAsSb

The system was applied to antimonide-based TPV device structures and substrates. The strong difference in pulse height and decay time between capped and uncapped device structures demonstrates the system's ability to discriminate surface passivation. With the use of double heterostructure capping (carrier confinement) layers with different active layer thicknesses, separation of bulk and surface effects yielded a 95 ns bulk lifetime in InGaAsSb, 1900 cm/s SRV at the InGaAsSb/AlGaAsSb interfaces, and 1300 cm/s SRV at the InGaAsSb/GaSb interface. In both the InGaAsSb device structures and the InGaAsSb quasi-binary substrates an inverse dependence on optical intensity was generally observed. This is indicative of radiative or Auger recombination being dominant. In the organometallic vapor phase epitaxy (OMVPE) samples, the bulk lifetimes fit a radiative behavior well; fitting the decay time versus excitation level yielded radiative lifetimes in the range of 70 ns with the GaSb caps and 210 ns with the AlGaAsSb caps. The difference observed may be resolved using a model which combines SRH and Auger recombination; however, data at additional intensities are required for a full evaluation.

GaSb-capped undoped InGaAsSb layers with bandgaps ranging from 0.50 to 0.59 eV show an increasing error in the fit to a purely radiative recombination model as the bandgap decreases, with radiative lifetime increasing towards a maximum of 960 ns for a 0.52 eV active layer. The variation of radiative lifetime with bandgap cannot be attributed to photon recycling because the index of refraction of the active layer is approximately constant. Since the samples are undoped (p_0~10^{16} cm^{-3}), the samples are subjected to higher injection levels than the previous set of samples conditions and Auger recombination is expected to become dominant, which may explain the error in fitting to a radiative recombination model. The possibility of an increased role played by Auger recombination can be explored with addition intensity data and fitting to a model that combines radiative and Auger recombination.

6.3. GaSb and InGaAsSb Substrates

An analysis of decay times in thick substrates indicated that the SRV and bulk lifetime can be determined by varying the wavelength of the optical excitation. Convolution of the analytical expression for impulse excitation with the shape of the optical pulse resulted in a minimum measurable bulk lifetime of 10 ns. Since the absorption constants differ by an order of magnitude with the wavelengths available, the SRV can be determined as low as 10^5 cm/s. The variation of bulk lifetime with intensity is used to qualitatively obtain the dominant mode of bulk recombination.

The SRVs of the unpassivated p-type GaSb and quasi-binary n-type InGaAsSb substrates were found to be approximately 2×10^6 cm/s using optical wavelengths of 1064 nm, 532 nm, and 266 nm, which is within the expected range. Due to the effect of band-bending at the surface in the n-type samples, the surface of the quasi-binaries are believed to be at least as good as the epi-ready commercial p-type GaSb substrate. In both the commercial and in-house grown p-type GaSb boule material the bulk lifetime dependence on optical intensity exhibited SRH recombination behavior, while radiative recombination generally dominated the recombination in n-type quasi-binary InGaAsSb. A dependence on excitation wavelength of the bulk lifetime was observed, but is presently not understood. At LN_2 temperatures, either radiative or SRH recombination appeared to dominate the bulk lifetime, while the dependence of the y-intercept is consistent with an order of magnitude increase in SRV at low temperatures. However, these results are preliminary, since the bulk lifetime and long decays were measured at only two temperatures.

The injection level dependence of the bulk lifetimes of the 0.40 and 0.55 eV quasi-binary samples showed that SRH recombination dominated the lower injection levels while radiative recombination dominated the higher injection levels. The dependence in the 0.60 eV sample exhibited SRH-dominated recombination and either radiative or Auger recombination in the 0.62 eV sample. At 77 K SRH recombination was found to dominate in each quasi-binary sample. The absence of SRH-dominated recombination in all but the 0.60 eV sample is an indication of the quality of quasi-binary InGaAsSb.

6.4. Suggestions for Future Work

In most of the data presented, the optical intensity was varied over less than two decades using fixed neutral density filters. While providing repeatable excitation levels, replacing the filters with fine control of the laser output energy will allow measurements at more injection levels within the extremes in pulse energy. Having bulk lifetimes at more intensities will improve the fitting used to determine the radiative and Auger lifetimes. In addition, the dynamic range may be extended on the high end by increasing the laser output energy, up to the damage threshold of the fiberoptic used to illuminate the sample (~6.5 mJ at 1064 nm). However, observation of low-level injection effects is limited by the noise floor of the RF electronics. Improvements in shielding and design may extend the dynamic range by as much as an order of magnitude. Finally, the ability to excite substrates with different optical wavelengths has been demonstrated to allow measurement of SRV; however, resolution is limited due to the large difference in absorption constant. The availability of additional wavelengths in between those presently available, will enhance the capability of the system. With careful control of sample temperature, delineation of the modes of recombination can be anticipated with a greater degree of confidence (particularly in combination with variation in laser intensity and wavelength).

The variation of bulk lifetime with optical wavelength observed in the thick substrates can be corroborated with similar measurements in thick epitaxial layers. However, in order to observe the wavelength dependence in epitaxial layers of practical thicknesses (≤ 8 µm) the absorption depth and the diffusion length must be much less than the layer thickness in order to approximate the conditions in thick substrates. For the latter condition, the bulk lifetime must be low ($<<25$ ns with a diffusion constant of 26 cm^2/s in an 8 µm layer). Such samples also permit the determination of the SRV without requiring double caps.

Photon recycling requires a radiative-dominated bulk recombination, a strong probability of re-absorption of light emitted at the bandgap, and reflective interfaces. The presence of photon recycling in InGaAsSb materials, which have been found to have a bulk lifetime dominated by radiative recombination, can be further studied by comparison of the effective radiative lifetime of samples grown with caps having thicknesses that interfere either constructively or destructively at the wavelength of the bandgap energy. Since the thickness of such caps will be on the order of 250 nm, it is important to select a material and excitation wavelength that minimize absorption in the cap.

The analyses presented in Chapters 4 and 5 rely on extracting bulk lifetimes by measuring the slope of processed decay transients. Fitting whole decay transients with a model which incorporates surface and bulk recombination, and trapping would permit more complete utilization of the information contained in each decay transient.

Literature Cited

1. M. Wolf, "Historical Development of Solar Cells", *Proc. 25th Power Sources Symp.*, 120 (May 1972).
2. L. Fraas, J. Avery, R. Ballantyne, P. Custard, L. Ferguson, H. H. Xiang, J. Keyes, B. Mulligan, J. Samaras, and D. Williams, "2-Amp TPV Cogenerator Using Forced-Air Cooled Gallium Antimonide Cells", *Thermophotovoltaic Generation of Electricity, 3rd NREL Conference*, 369 (1997).
3. B. D. Wedlock, "Thermo-Photo-Voltaic Energy Conversion", *Proceedings of the IEEE*, 694 (May 1963).
4. C. K. Gethers, C. T. Ballinger, M. A. Postlethwait, D. M. DePoy, and P. F. Baldasaro, "TPV Efficiency Predictions and Measurements for a Closed Cavity Geometry", *Thermophotovoltaic Generation of Electricity, 3rd NREL Conference*, 471 (1997).
5. G. W. Charache, P. F. Baldasaro, L. R. Danielson, D. M. DePoy, M. J. Freeman, C. A. Wang, H. K. Choi, D. Z. Garbuzov, R. U. Martinelli, S. Saroop, J. M. Borrego, R. J. Gutmann, "InGaAsSb Thermophotovoltaic Diode: Physics Evaluation", J. Appl. Phys. **85**, 2247 (1999).
6. C. Hitchcock, R. Gutmann, J. Borrego, H. Ehsani, I. Bhat, M. Freeman, and G. Charache, "GaInSb and GaInAsSb Thermophotovoltaic Device Fabrication and Characterization", *Thermophotovoltaic Generation of Electricity, 3rd NREL Conference*, 89 (1997).

7. C. W. Hitchcock, R. J. Gutmann, H. Ehsani, I. B. Bhat, C. A. Wang, M. J. Freeman, G. W. Charache, "Ternary and Quaternary Antimonide Devices for Thermophotovoltaic Applications", presented at the OMVPE Conference, San Diego, CA (1998).
8. H. C. Casey, Jr. and F. Stern, "Concentration-dependent absorption and spontaneous emission of heavily doped GaAs", J. Appl. Phys. **47**, 631 (1976).
9. M. Levinshtein, S. Rumyantsev, and M. Shur, *Handbook Series on Semiconductor Parameters Volume II*, to be published.
10. G. Burns, *Solid State Physics*, (Academic Press, New York, 1985) p 467.
11. G. Burns, *Solid State Physics*, (Academic Press, New York, 1985) p 448.
12. G. Burns, *Solid State Physics*, (Academic Press, New York, 1985) p 461-495.
13. J. J. Sakurai, Advanced Quantum Mechanics, (Addison-Wesley, New York, 1967) p 41.
14. S. M. Sze, *Physics of Semiconductor Devices 2nd Edition*, (J. Wiley & Sons, New York, 1981) p 802-803.
15. S. M. Sze, *Physics of Semiconductor Devices 2nd Edition*, (J. Wiley & Sons, New York, 1981) p 806.
16. W. van Roosbroeck and W. Schockley, Phys. Rev. **94**, 1558 (1954).
17. J. S. Blakemore, *Semiconductor Statistics*, (Pergamon Press, New York, 1962) p 200.
18. J. S. Blakemore, *Semiconductor Statistics*, (Pergamon Press, New York, 1962) p 211.
19. A. R. Beattie and P. T. Landsberg, Proc. Roy. Soc. London Ser. A **16**, 249 (1959).

20. S. M. Sze, *Physics of Semiconductor Devices 2nd Edition*, (J. Wiley & Sons, New York, 1981) p 35.
21. W. Shockley, *Electrons and Holes in Semiconductors*, (D. Van Nostrand, New York, 1951).
22. S. K. Ghandhi, *The Theory and Practice of Microelectronics*, (R. E. Krieger, Florida, 1968) p 433.
23. S. K. Ghandhi, *The Theory and Practice of Microelectronics*, (R. E. Krieger, Florida, 1968) p 431.
24. D. K. Schroeder, *Semiconductor Material and Device Characterization*, (J. Wiley & Sons, New York, 1990) p 432.
25. D. K. Schroeder, *Semiconductor Material and Device Characterization*, (J. Wiley & Sons, New York, 1990) p 359-447.
26. J. W. Orton and P. Blood, *The Electrical Characterization of Semiconductors: Measurement of Minority Carrier Properties*, (Academic Press, London, 1990), p 51-122.
27. D. T. Stevenson and R. J. Keyes, "Measurement of Carrier Lifetime in Germanium and Silicon", J. Appl. Phys. **26**, 190 (1955).
28. S. H. Shin, J. M. Arias, M. Zandian, J. G. Pasko, and R. E. DeWames, "Effect of the dislocation density on minority-carrier lifetime in molecular beam epitaxial HgCdTe", Appl. Phys. Lett. **59** (21), 2817 (1991).
29. S. W. Kurnick and R. N. Zitter, J. Appl. Phys. **27**, 278 (1956).
30. J. W. Orton and P. Blood, *The Electrical Characterization of Semiconductors: Measurement of Minority Carrier Properties*, (Academic Press, London, 1990),

p 65.

31. R. J. Nelson and R. G. Sobers, Appl. Phys. Lett. **32**, 761 (1978).
32. R. K. Ahrenkiel, "Measurement of minority-carrier lifetime by time-resolved photoluminescence", Solid-State Elec. **35** (3), 239 (1992).
33. B. Mendez, J. Piqueras, P. S. Dutta, and E. Dieguez, "Cathodoluminescence microscopy of doped GaSb crystals", Mat. Sci. and Eng. **B42**, 38 (1996).
34. M. Mazzer, E. Grünbaum, K. W. J. Barnham, J. Barnes, P. R. Griffin, D. B. Holt, J. L. Hutchison, A. G. Norman, J. P. R. David, J. S. Roberts, and R. Grey, "Study of misfit dislocations by EBIC, CL and HRTEM in GaAs/InGaAs lattice-strained multi-quantum well p-i-n solar cells", Mat. Sci. and Eng. **B42**, 43 (1996).
35. J. Linnros, "Carrier lifetime measurements using free carrier absorption transients. I. Principle and injection dependence", J. Appl. Phys. **84**, 275 (1998).
36. G. Beck and M. Kunst, Rev. Sci. Inst. **57**, 197 (1986).
37. J. M. Borrego, R. J. Gutmann, N. Jensen, and O. Paz, "Non-destructive lifetime measurements in silicon wafers by microwave reflection", Solid-State Electronics **30**, 195 (1987).
38. M. C. Chen, "Photoconductivity lifetime measurements on HgCdTe using a contactless microwave technique", J. Appl. Phys. **64**, 945 (1988).
39. J. W. Orton and P. Blood, *The Electrical Characterization of Semiconductors: Measurement of Minority Carrier Properties*, (Academic Press, London, 1990), p 90.
40. J. A. Naber and D. P. Snowden, Rev. Sci. Inst. **40**, 1137 (1969).
41. R. J. Gutmann, J. M. Borrego, C. S. Lo, M. C. Heimlich, O. Paz, "Microwave-

detected photoconductivity-transient spectroscopy for non-destructive evaluation of GaAs wafers", *Modern Optical Characterization Techniques for Semiconductors and Semiconductor Devices*, O. J. Glembocki, F. H. Pollack, and J. J. Song, Editors, Proc. SPIE **794**, p. 128 (1987).

42. C. S. Campbell, "The effect of ion implantation processing on semi-insulating GaAs wafers using photo-enhanced microwave reflectance", Masters Thesis, Rensselaer Polytechnic Institute, Sept. 1988.
43. M. C. Heimlich, "Non-destructive GaAs characterization by microwave-detected photoconductivity-response spectroscopy", Masters Thesis, Rensselaer Polytechnic Institute, August 1987.
44. N. Jensen, "Nondestructive characterization of semiconductor wafers by microwave reflection", Masters Thesis, Rensselaer Polytechnic Institute, May 1986.
45. Y. Mada, Jpn. J. Appl. Phys. **18**, 2171 (1979).
46. K. D. Cummings, S. J. Pearton, and G. P. Vella-Coleiro, J. Appl. Phys. **60**, 1676 (1986).
47. A. Buczkowski, Z. J. Radzimski, G. A. Rozgonyi, and F. Shimura, "Separation of the bulk and surface components of recombination lifetime obtained with a single laser/microwave photoconductance technique", J. Appl. Phys. **72** (7), 2873 (1992).
48. F. Shimura, T. Okui, and T. Kusama, "Noncontact minority-carrier lifetime measurement at elevated temperatures for metal-doped Czochralski silicon crystals", J. Appl. Phys. **67**, 7168 (1990).
49. E. Yablonovitch and T. J. Gmitter, "A contactless minority lifetime probe of heterostructures, surfaces, interfaces and bulk wafers", Sol.-State. Elect. **35** (3),

261 (1992).

50. R. K. Ahrenkiel, D. Levi, and J. Arch, "Recombination lifetime studies of silicon spheres", Solar Energy Mat. And Solar Cells **41/42**, 171 (1996).

51. R. K. Ahrenkiel, S. P. Ahrenkiel, and D. J. Arent, "Recombination lifetime in ordered and disordered InGaAs", *Thermophotovoltaic Generation of Electricity, 2nd NREL Conference*, 434 (1996).

52. P. S. Dutta, H. L. Bhat, and V. Kumar, "The physics and technology of gallium antimonide: An emerging optoelectronic material", J. Appl. Phys. **81** (9), 5821 (1997).

53. R. K. Ahrenkiel, R. Ellingson, S. Johnston, and M. Wanlass, "Recombination Lifetime on $In_{0.53}Ga_{0.47}As$ as a Function of Doping Density", Appl. Phys. Lett. **72** (26), 3470 (1998).

54. H. S. Carslaw and J. C. Jaeger, *Conduction of Heat in Solids 2nd Edition*, (Clarendon Press, Oxford, 1959) p144-146.

55. D. L. Keune, N. Holonyak Jr., R. D. Burnham, D. R. Scifres, H. W. Zwicker, J. W. Burd, M. G. Craford, D. L. Dickus, and M. J. Fox, "Optical Phase-Shift Measurement of Carrier Decay Times (77 K) on Lightly Doped Double-Surface and Surface-Free Epitaxial GaAs", J. Appl. Phys. **42**, 2048 (1971).

56. R. K. Ahrenkiel, B. M. Keyes, and D. J. Dunlavy, "Intensity-dependent minority-carrier lifetime in III-V semiconductors due to saturation of recombination centers", J. Appl. Phys. **70** (1), 225 (1991).

57. R. K. Ahrenkiel, "Influence of junctions on photoluminescence decay in thin-film devices", J. Appl. Phys. **62** (7), 2937 (1987).

58. J. S. Blakemore, *Semiconductor Statistics*, (Pergamon Press, New York, 1962) p 221.

59. S. M. Sze, *Physics of Semiconductor Devices, 2nd Edition*, (J. Wiley and Sons, New York, 1981), p. 849.

60. A. R. Beattie and P. T. Landsberg, Proc. Roy. Soc. London A **258**, 486 (1960).

61. W. Press, S. Teukolsky, W. Vetterling, B. Flannery, *Numerical Recipes in C 2nd Edition*, (Cambridge University Press, Cambridge, 1992) p 421.

62. M. Muñoz, K. Wei, F. Pollack, J. L. Freeouf, C. A. Wang, and G. W. Charache, "Optical constants of $Ga_{1-x}In_xAs_ySb_{1-y}$ lattice-matched to GaSb (100): experiment and modeling", (Accepted for publication J. Appl. Phys.).

63. G. W. Charache, P. F. Baldasaro, L. R. Danielson, D. M. DePoy, M. J. Freeman, C. A. Wang, H. K. Choi, D. Z. Garbuzov, R. U. Martinelli. V. Khalfin, S. Saroop, J. M. Borrego, and R. J. Gutmann, "InGaAsSb thermophotovoltaic diode: Physics evaluation", J. Appl. Phys. **85** (4), 2247 (1999).

64. C. A. Wang, in private communications.

65. S. Adachi, "Band gaps and refractive indices of AlGaAsSb, GaInAsSb, and InPAsSb: Key properties for a variety of the 2-4 μm optoelectronic device applications", J. Appl. Phys. **61** (10), 4869 (1987).

66. G. W. Charache, P. F. Baldasaro, J. M. Borrego, S. Saroop, R. J. Gutmann, and C. A. Wang, "Photon recycling in 0.53 eV InGaAsSb", Electronic Materials Conference, Santa Barbara, CA, June 1999.

67. Y. Jiang, M. C. Teich, and W. I. Wang, "The Auger recombination rate is larger in a GaSb quantum well than in bulk GaSb", J. Appl. Phys. **62** (2), 836 (1991).

68. E. Kreyszig, *Advanced Engineering Mathematics 5th Edition*, (J. Wiley & Sons, New York, 1983) p 796.

69. D. K. Schroeder, *Semiconductor Material and Device Characterization*, (J. Wiley & Sons, New York, 1990) p. 320.

70. P. S. Dutta and A. G. Ostrogorsky, "Melt growth of quasi-binary $(GaSb)_{1-x}(InAs)_x$ crystals", J. Crystal Growth **199**, 384 (1999).

71. P. S. Dutta and A. G. Ostrogorsky, "Strong band gap narrowing in quasi-binary $(GaSb)_{1-x}(InAs)_x$ crystals grown from melt", J. Crystal Growth **197**, 1 (1999).

72. Palik, E. D., ed., *Handbook of Optical Constants of Solids*, (Academic Press, Orlando, 1985) pp. 429, 479.

73. G. Burns, *Solid State Physics*, (Academic Press, New York, 1985) p 456-458.

74. G. Lasker and F. Storm, , Phys. Rev. A **133**, 533 (1964).

75. Y. Tian, T. Zhou, B. Zhang, Y. Jin, Y. Ning, H. Jiang, G. Yuan, "Theoretical analysis of the Auger mechanism in a GaInAsSb infrared photovoltaic detector", Opt. Eng. **37**(6), 1754 (1998).

76. A. R. Beattie and A. M. White, "An analytic approximation with a wide range of applicability for electron initiated Auger transitions in narrow-gap semiconductors", J. Appl. Phys. **79** (2), 802 (1996).

Appendix A

RF Photoreflectance Software

The software used to collect, store, and perform basic analysis on photoreflectance decay transients was developed in National Instruments LabView 4.0® running under the Windows 95® operating system on a 233 MHz Pentium-II class PC. LabView provides a framework for graphical programming and control of and communication with laboratory instruments via the General Purpose Interface Bus (GPIB). The program flow is developed in the diagram frame while the user interface is designed on the front panel frame.

Program execution begins when the user presses the "Run" button (▶) under the menu bar and runs in an infinite loop until the "Stop" button (▣) is pressed. Once running, the user may select the number of points per trace by entering the value in the "# points" text box (default: 1000), select the desired channel on the digital oscilloscope from which the data is to be collected by moving the "digitize" and "read source" sliders, enter the width of the smoothing window (i.e., moving average) in the "Smoothing Window Size" text box (default: 10), load/save data from/to disk by pressing the "Load Data" or "Save Data" button, overwrite pre-saved data by pressing the "Replace" button, move the red and yellow cursors (vertical lines in the graphics display windows) by moving the corresponding slider or entering a value in the "Index" box, enter comments into the "Comments" text box, or record any of three decay times and the corresponding cursor locations by pressing the record button (▣) under either the "Risetime", "1st Decay", or "2nd Decay" box. Digitized data or data loaded from disk is displayed in the graphics display windows. The lower window displays the raw data on a linear scale, while the upper window displays the smoothed data on a log scale. The windows automatically adjust the x- and y-axis ranges to fit the data, but the user may override the autoscaling at any time by clicking on the number displayed at the desired axis extreme.

At any time, the user may move the red or yellow cursor as describe above. As the cursor is moved, the exponential that fits the smoothed data displayed in the upper graphics window bracketed by the cursors is overlayed in cyan in real-time in both windows. The fitting is accomplished with a least-squares calculation, while the exponential decay time is displayed in the "Avg. Decay" window in ns and the statistical error (calculated from a t-distribution) is displayed in the "Error" window in ns. The cursors may also be moved by loading the positions stored in any of the decay time windows by pressing the corresponding ▶ button. When data is loaded from disk, the filename is displayed in the "Filename" box, the time at which the data was originally digitized is displayed in the "Timestamp" box, the user's stored comments are displayed in the "Comments" textbox, and any values stored in the decay time windows are loaded. When data is read from the oscilloscope, the current system time is displayed in the "Timestamp" window, the data is displayed in the graphics windows, and all of the decay time boxes and the "Filename" box are cleared.

Appendix B - Radiative and Auger Fitting Algorithm

Analysis of the dependence of bulk lifetime on injection level for thin active layers was accomplished by fitting the bulk lifetimes to analytic expressions for the solution of radiative and Auger recombination neglecting the diffusion term (i.e., assuming a uniform carrier distribution). The analysis is accomplished using algorithms written in Maple V© Release 5 by Waterloo Maple Inc.

The algorithm used calculates the bulk lifetimes for each intensity by subtracting the surface lifetime using the sample thickness and the surface recombination velocity (SRV). It then generates an error function from the difference between the bulk lifetimes and an analytical calculation of the decay time, evaluated at the same time delay from the impulse excitation that the data was taken after the peak of the optical pulse. Plots of the error function are generated in discrete increments of one parameter while varying the other(s), and the minima are determined graphically.

For a purely radiative fit, the parameters against which the error function is plotted are the radiative lifetime and the maximum injection level. A 3-dimensional plot is first generated varying both parameters in order to locate the absolute minimum of the error function. The 2-dimensional plots are then used to precisely determine the value of each parameter at the minimum as well as the value of the error function at the minimum. The data is then plotted versus the intensity relative to the minimum pulse energy with the curve of the analytical expression for bulk lifetime equation overlaid to verify the fit. The radiative-only algorithm is given in Listing B.1.

Listing B.1 Maple V Algorithm for Radiative Recombination Fitting

```
> p0:=2e17;ni:=2.7e13;S:=1900;
```

$$p0 := .2\ 10^{18}$$

$$ni := .27\ 10^{14}$$

$$S := 1900$$

Solution of radiative recombination equation neglecting diffusion term (nn=n(0))

```
> n:=(t,nn)->p0*nn/((p0+nn)*exp(t/tau)-nn);
```

$$n := (t, nn) \rightarrow \frac{p0\ nn}{(p0 + nn)\ \mathbf{e}^{\left(\frac{t}{\tau}\right)} \quad nn}$$

Raw data [n(0), decay time (ns)] and active layer thickness W (um)

```
> t722a:=[[.02,51.3],[.052,49.1],[.147,41.5],[1,28.6]]:
t722b:=[[.02,40.1],[.052,36.2],[.147,35.6],[1,30.4]]:
t722c:=[[.02,48.4],[.052,41.2],[.147,37.7],[1,29.2]]:
t725:=[[.02,49.7],[.052,38.8],[.147,29.5],[1,25.3]]:
t723:=[[.02,61.8],[.052,46.6],[.147,32.4],[1,28.4]]:
t728:=[[.02,64.1],[.052,46.3],[.147,41.9],[1,33.3]]:
t812:=[[.02,38.2],[.052,30.6],[.147,29.5],[1,26.6]]:
t813:=[[.02,33.7],[.052,28.4],[.147,29.4],[1,24.4]]:
t814:=[[.02,40.1],[.052,34.6],[.147,29.6],[1,23.5]]:
t815:=[[.02,45.6],[.052,37.2],[.147,32.7],[1,23.8]]:
t816:=[[.02,50.8],[.052,43.5],[.147,37.5],[1,28.4]]:
t871:=[[.02,45.7],[.052,39.4],[.147,36.5],[1,29]]:
t872:=[[.02,56.5],[.052,46.1],[.147,38.7],[1,34.3]]:
t873:=[[.02,30],[.052,29.1],[.147,27.3],[1,28.9]]:
t874:=[[.02,53.6],[.052,50.1],[.147,56.8],[1,33.9]]:
t874m:=[[.02,53.6],[.052,50.1],[1e20,33.9]]:
tt:=t722c;W:=4e-4:
```

tt := [[.02, 48.4], [.052, 41.2], [.147, 37.7], [1, 29.2]]

Subtract surface lifetime

```
> N:=linalg[vectdim](tt);for j from 1 to N do
tt[j][2]:=1/(1/tt[j][2]-2*S/W*1e-9) od:tt;
```

N := 4

[[.02, 89.59644580], [.052, 67.69635228], [.147, 58.73646490], [1, 40.40963189]]

Theoretical bulk lifetime in ns (t0=delay from pulse peak)

```
> t0:=30e-9;f:=unapply(-n(t,nn)/diff(n(t,nn),t)*1e9,(t,tau,
nn));
```

$$t0 := .30\ 10^{-7}$$

$$f := (t, \tau, nn) \to .1000000000\ 10^{10}\ \frac{\left((.2\ 10^{18} + nn)\ \mathbf{e}^{\left(\frac{t}{\tau}\right)} - nn\right)\tau}{(.2\ 10^{18} + nn)\ \mathbf{e}^{\left(\frac{t}{\tau}\right)}}$$

Error function (tau=radiative lifetime, x=maximum injection level)

```
> error:=(tau,x)->sum((f(t0,tau,x*tt[i][1])-tt[i][2])^2,i=
1..N);
```

$$error := (\tau, x) \to \sum_{i=1}^{N} (\mathrm{f}(t0, \tau, x\ tt_{i_1}) - tt_{i_2})^2$$

3D plot of error function vs. log(radiative lifetime) and log(injection level)

```
> plot3d(error(10^x,10^y),x=-8..-4,y=17..20,axes=boxed,view
=0..700,grid=[100,25]);
```

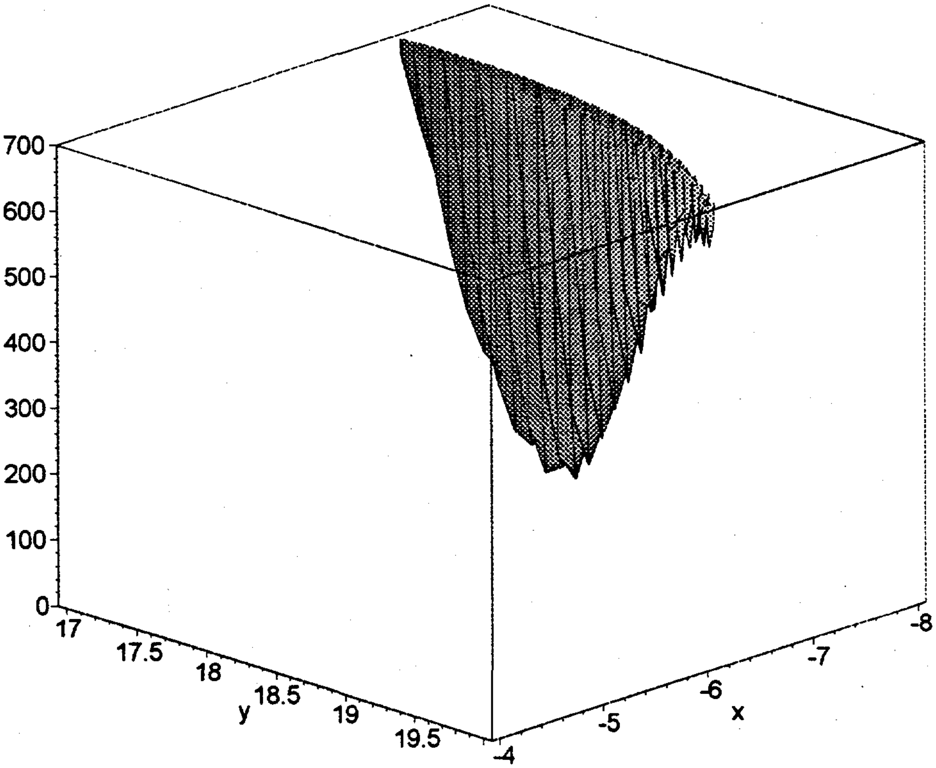

2D plots of error function (x=log(injection level), y=radiative lifetime)

```
> taul:=80:tauh:=120:xl:=18:xh:=18.4:plot({seq(error(tau*
.5e-9,10^x),tau=2*taul..2*tauh)},x=xl..xh,y=90..180,color=
red,labels=[`log|Injection Level|`,`Error`]);plot({seq(
```

```
error(tau*1e-9,10^(x/80)),x=80*xl..80*xh)},tau=taul..tauh,
```

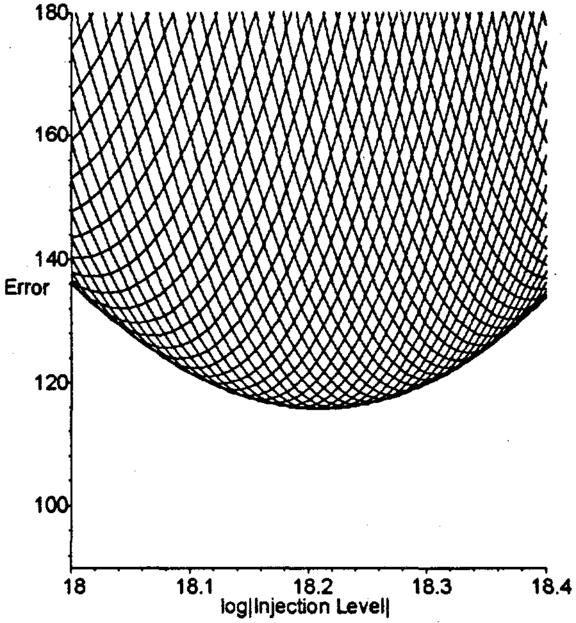

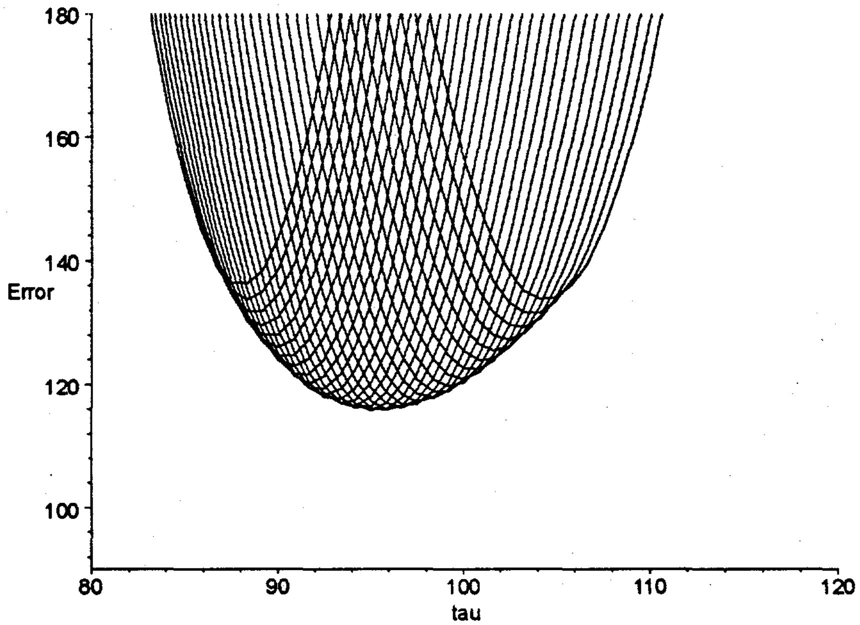

```
y=90..180,color=blue,labels=[`tau`,`Error`]);
```

Overlay of measured bulk lifetime and radiative fit (relative to minimum injection level)

```
> inj:=18.25:taur=96e-9:p1:=plot([seq([log10(tt[i][1]/.02),
tt[i][2]],i=1..N)],style=point,symbol=circle,color=black,
labels=[``,``]):p2:=plot(f(t0,taur,10^(i+inj-1.699)),i=-.2..
1.8,color=black,labels=[``,``],linestyle=1,thickness=1):plot
s[display]({p1,p2},axes=boxed,labels=[`log|Relative
Intensity|`,`Bulk Lifetime (ns)`]);
```

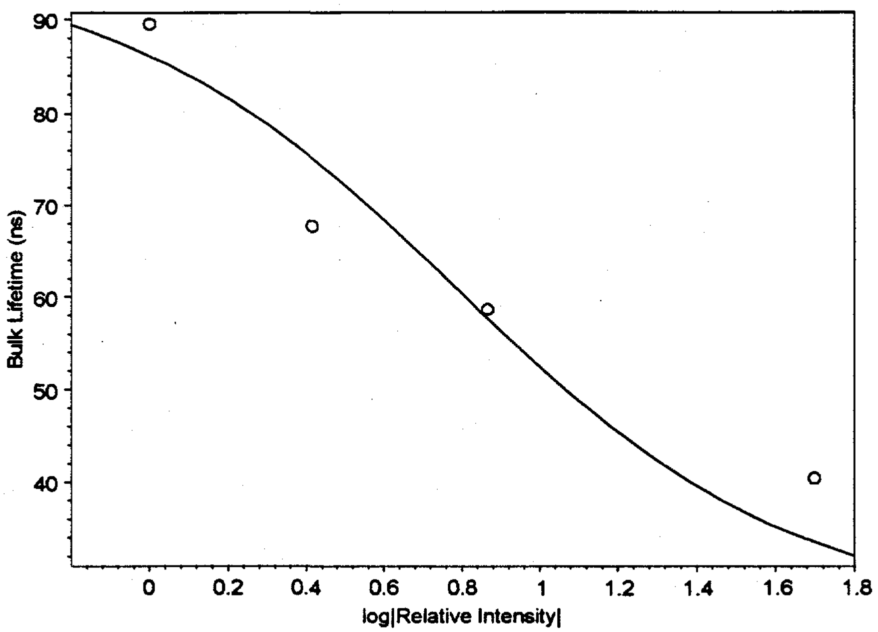

The algorithm in Listing B.2 is used to fit the bulk lifetimes to a combined radiative and Auger recombination model. The parameters against which the error function is plotted are the radiative lifetime, the intrinsic Auger lifetime, and the maximum injection level. An animated 3-dimensional plot is first generated varying both lifetimes and with the injection level serving as the time index in order to locate the absolute minimum of the error function. The 3-dimensional plots are then used to locate the value of each parameter at the minimum as well as the value of the error function at the minimum. A steepest descent procedure is then used to precisely determine the lifetimes and maximum injection level at the absolute minimum. The data is then plotted versus the intensity relative to the minimum pulse energy with the curve of the analytical expression of the bulk lifetime overlaid to verify the fit.

Listing B.2 Maple V Algorithm for Radiative+Auger Recombination Fitting

Solution of Auger recombination equation neglecting diffusion

```
> solve((1+p0/n)*exp(-p0/n)=C*exp(-p0^2*t/2/ni^2/taua),n);
```

$$-\frac{p0}{\mathrm{LambertW}\left(-C\,\mathbf{e}^{\left(-\frac{1}{2}\,\frac{p0^{2}\,t+2\,ni^{2}\,taua}{ni^{2}\,taua}\right)}\right)+1}$$

Analytical expressions for Auger recombination (na) and radiative recombination (n)

```
> na:=(t,taua,nn)->-p0/(LambertW(-1,-(1+p0/nn)*exp(-p0^2*t/
2/ni^2/taua-p0/nn-1))+1);n:=(t,tau,nn)->p0*nn/((p0+nn)*exp(t
/tau)-nn);
```

$$na := (t, taua, nn) \to -\frac{p0}{\mathrm{LambertW}\left(-1, -\left(1+\frac{p0}{nn}\right)\mathbf{e}^{\left(-\frac{1}{2}\,\frac{p0^{2}\,t}{ni^{2}\,taua}-\frac{p0}{nn}-1\right)}\right)+1}$$

$$n := (t, \tau, nn) \to \frac{p0\,nn}{(p0+nn)\,\mathbf{e}^{\left(\frac{t}{\tau}\right)}-nn}$$

Theorical bulk lifetimes for Auger (f) and radiative (fr) recombination in ns

```
> f:=unapply(-na(t,taua,nn)/diff(na(t,taua,nn),t),[t,taua,
nn])*1e9;fr:=unapply(-n(t,tau,nn)/diff(n(t,tau,nn),t),(t,tau
,nn))*1e9;
```

$$f := .1\;10^{10}\left((t, taua, nn) \to -2\,\frac{\left(\mathrm{LambertW}\left(-1, -\left(1+\frac{p0}{nn}\right)\mathbf{e}^{\left(-\frac{1}{2}\,\frac{p0^{2}\,t}{ni^{2}\,taua}-\frac{p0}{nn}-1\right)}\right)+1\right)^{2} ni^{2}\,taua}{p0^{2}\,\mathrm{LambertW}\left(-1, -\left(1+\frac{p0}{nn}\right)\mathbf{e}^{\left(-\frac{1}{2}\,\frac{p0^{2}\,t}{ni^{2}\,taua}-\frac{p0}{nn}-1\right)}\right)}\right)$$

$$fr := .1\ 10^{10} \left((t, \tau, nn) \to 1.000000000 \frac{\left((.1\ 10^{17} + nn)\, e^{\left(\frac{t}{\tau}\right)} - nn \right) \tau}{(.1\ 10^{17} + nn)\, e^{\left(\frac{t}{\tau}\right)}} \right)$$

```
> p0:=1e16;ni:=2.7e13;n0:=ni^2/p0;S:=1300;
```

$$\mathbf{p0} := .1\ 10^{17}$$

$$\mathbf{ni} := .27\ 10^{14}$$

$$\mathbf{n0} := .7290000000\ 10^{11}$$

$$\mathbf{S} := 1300$$

Raw data [n(0), decay time (ns)] and active layer thickness (W)

```
> t725:=[[.02,49.7],[.052,38.8],[.147,29.5],[1,25.3]]:
t723:=[[.02,61.8],[.052,46.6],[.147,32.4],[1,28.4]]:
t728:=[[.02,64.1],[.052,46.3],[.147,41.9],[1,33.3]]:
t812:=[[.02,38.2],[.052,30.6],[.147,29.5],[1,26.6]]:
t813:=[[.02,33.7],[.052,28.4],[.147,29.4],[1,24.4]]:
t814:=[[.02,40.1],[.052,34.6],[.147,29.6],[1,23.5]]:
t815:=[[.02,45.6],[.052,37.2],[.147,32.7],[1,23.8]]:
t816:=[[.02,50.8],[.052,43.5],[.147,37.5],[1,28.4]]:
t871:=[[.02,45.7],[.052,39.4],[.147,36.5],[1,29]]:
t872:=[[.02,56.5],[.052,46.1],[.147,38.7],[1,34.3]]:
t873:=[[.02,30],[.052,29.1],[.147,27.3],[1,28.9]]:
t874:=[[.02,53.6],[.052,50.1],[.147,56.8],[1,33.9]]:
t874m:=[[.02,53.6],[.052,50.1],[1,33.9]]:
tt:=t874m;W:=2e-4:
```

tt := [[.02, 53.6], [.052, 50.1], [1, 33.9]]

Subtract surface lifetime

```
> N:=linalg[vectdim](tt);for j from 1 to N do tt[j][2]:=1/
(1/tt[j][2]-2*S/W*1e-9) od:tt;
```

N := 3

[[.02, 176.7810026], [.052, 143.6765128], [1, 60.61147865]]

Error function (t=intrinsic Auger lifetime (s), tr=radiative lifetime (s), x=injection level, t0=delay from pulse peak)

```
> t0:=45e-9;error:=(t,tr,x)->sum((1/(1/f(t0,t,10^x*
tt[k][1])+1/fr(t0,tr,10^x*tt[k][1]))-tt[k][2])^2,k=1..N);
```

$$\mathbf{t0 := .45\ 10^{-7}}$$

$$error := (t, tr, x) \rightarrow \sum_{k=1}^{N} \left(\frac{1}{\dfrac{1}{\mathrm{f}\left(t0, t, 10^{x}\, tt_{k_1}\right)} + \dfrac{1}{\mathrm{fr}\left(t0, tr, 10^{x}\, tt_{k_1}\right)}} - tt_{k_2} \right)^2$$

Animation of 3D plots of error function vs. log|radiative lifetime| and log|intrinsic Auger lifetime| at different injection levels

```
> plots[animate3d](error(10^x,10^y,z),x=-1.5..3.5,y=-8..-4,
z=17..19,view=0..500,axes=boxed,frames=21,grid=[25,100]);
```

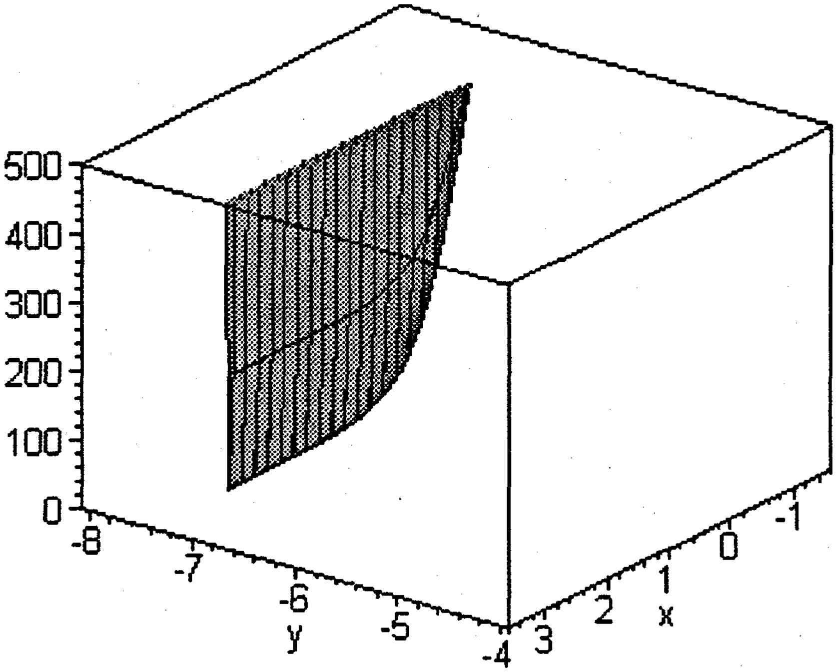

Partial derivatives of error function for use in the iterative algorithm

```
> dxerror:=unapply(diff(error(x,y,z),x),(x,y,z)):dyerror:=
unapply(diff(error(x,y,z),y),(x,y,z)):dzerror:=unapply(diff(
error(x,y,z),z),(x,y,z)):
```

Procedure to find local minimum of error function based on a steepest descent algorithm
Inputs: guesses for log|radiative lifetime| (a), log|intrinsic Auger lifetime| (b), and log|max. injection level| (c)

```
> sol:=proc(a,b,c)
> local x,y,xx,yy,z,zz,err,f,del,i,maxh,scale;global h;
```

```
> x:=a;y:=b;z:=c;maxh:=.03;
> del:=1;i:=0;
> while abs(del)>1e-6 do h:=linalg[vector]([1/(dxerror(
10^x,10^y,z)*10^x*2.3026),1/(dyerror(10^x,10^y,z)*10^y*
2.3026),1/dzerror(10^x,10^y,z)]);
> scale:=sqrt(linalg[dotprod](h,h));
> h:=map(x->x/scale*maxh,h);
> del:=1;err:=1;
> while abs(del)>maxh*10 do
> f:=error(10^x,10^y,z);
> xx:=x-h[1];if xx<-6 then xx:=-6; elif xx>4 then xx:=4;fi;
> yy:=y-h[2];if yy<-9 then yy:=-9; elif yy>-4 then yy:=-4;
fi;
> zz:=z-h[3];if zz<-4 then zz:=-4; elif zz>0 then zz:=0;fi;
> del:=f-error(10^xx,10^yy,zz);
> err:=sqrt((x-xx)^2+(y-yy)^2+(z-zz)^2);
> x:=xx;y:=yy;z:=zz;i:=i+1;if del<0 then h:=map(x->-x/2,h);
fi;
> od;maxh:=err/10;print("Loop: ",10^x,10^y,z,error(10^x,
10^y,z));od;
> print("Solution: ",10^x,10^y,z,error(10^x,10^y,z));
> end;
```

```
sol := proc(a, b, c)
local x, y, xx, yy, z, zz, err, f, del, i, maxh, scale;
global h;
   x := a;
   y := b;
   z := c;
   maxh := .03;
   del := 1;
   i := 0;
   while .1*10^(-5) < abs(del) do
      h := linalg[vector]([.4342916703*1/(dxerror(10^x, 10^y, z)*10^x),
         .4342916703*1/(dyerror(10^x, 10^y, z)*10^y),1/dzerror(10^x, 10^y, z)]);
      scale := sqrt(linalg[dotprod](h, h));
      h := map(x -> x*maxh/scale, h);
      del := 1;
      err := 1;
      while 10*maxh < abs(del) do
         f := error(10^x, 10^y, z);
         xx := x - h[1];
         if xx < -6 then xx := -6 elif 4 < xx then xx := 4 fi;
         yy := y - h[2];
         if yy < -9 then yy := -9 elif -4 < yy then yy := -4 fi;
         zz := z - h[3];
```

```
      if zz < -4 then zz := -4 elif 0 < zz then zz := 0 fi;
      del := f - error(10^xx, 10^yy, zz);
      err := sqrt((x - xx)^2 + (y - yy)^2 + (z - zz)^2);
      x := xx; y := yy; z := zz;
      i := i + 1;
      if del < 0 then h := map(x -> - 1/2*x, h) fi
    od;
    maxh := 1/10*err;
    print("Loop: ", 10^x, 10^y, z, error(10^x, 10^y, z))
  od;
  print("Solution: ", 10^x, 10^y, z, error(10^x, 10^y, z))
end
```

```
> sol(3,-6.7,-2.9);
    "Loop: ", 1071.519300, .1995275082 10^-6 , -2.900011618, 211.8013213
    "Loop: ", 1078.946717, .1995276272 10^-6 , -2.900012702, 211.7922935
    "Loop: ", 1079.692285, .1995276392 10^-6 , -2.900012810, 211.7913908
    "Loop: ", 1079.766870, .1995276406 10^-6 , -2.900012821, 211.7912958
    "Loop: ", 1079.774329, .1995276406 10^-6 , -2.900012822, 211.7912930
    "Loop: ", 1079.775074, .1995276406 10^-6 , -2.900012822, 211.7912925
    "Solution: ", 1079.775074, .1995276406 10^-6 , -2.900012822, 211.7912925
```

3D plot of error function at a given injection level (x=log|intrinsic Auger lifetime, y=log|radiative lifetime|)

```
> plot3d(error(10^x,10^y,16),x=0..3.5,y=-6..0,view=-1e4..
1e4);
```

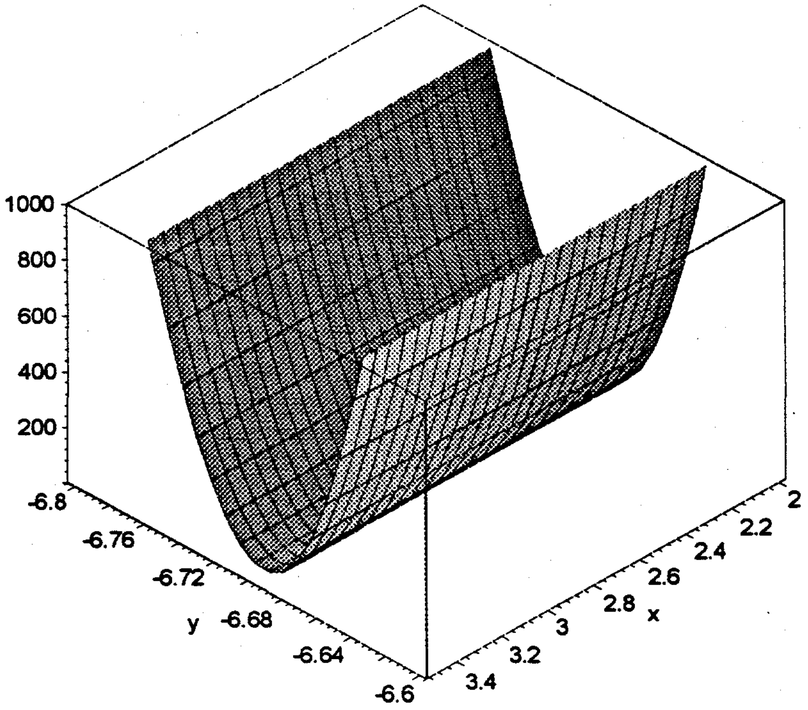

```
> inj:=19.02:taur:=9.95e-6:taua:=2.47:p5:=plot([seq([log10(
tt[i][1]/.02),tt[i][2]],i=1..N)],style=point,symbol=box,
color=black,labels=[``,``]):p6:=plot(1/(1/f(t0,taua,10^(i+
inj))+1/fr(t0,taur,10^(i+inj)))),i=-.2..1.8,color=black,
labels=[``,``],linestyle=3):plots[display]({p1,p2,p3,p4,p5,
p6},axes=boxed,labels=[`log|Relative Intensity|`,`Bulk
Lifetime (ns)`]);
```

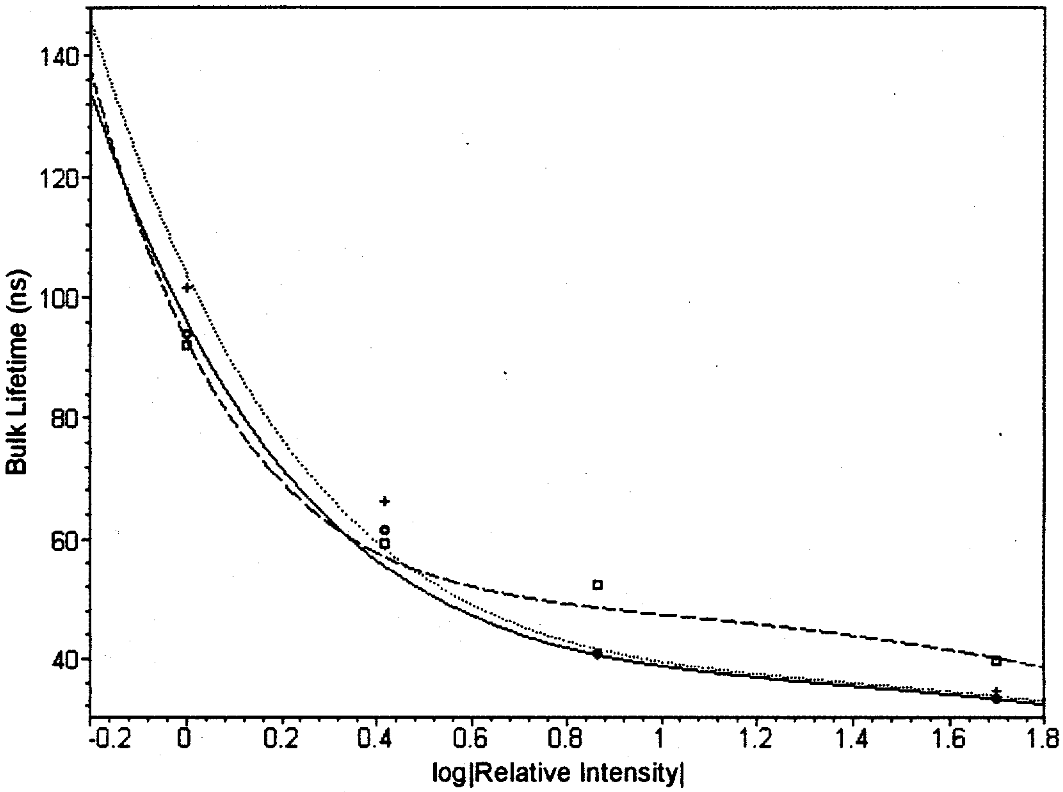

Appendix C - SRH Recombination Model

The SRH recombination rate given in Equation 2.37 can be rewritten by dividing the numerator and denominator by σ_p, resulting in

$$U=\frac{\left(pn-n_i^2\right)N_t v_{th}\sigma_n}{p_0+n_0\gamma+(1+\gamma)n'+\left(\gamma e^{\frac{E_t-E_i}{kT}}+e^{-\frac{E_t-E_i}{kT}}\right)n_i}\ , \tag{C.1}$$

where $\gamma=\sigma_n/\sigma_p$ and n' is the excess carrier concentration. If the material is doped p-type, i.e., $p_0>>n_0$, then the expression can be further simplified to give

$$\begin{aligned} U &\approx \frac{\left(n'^2+n'p_0\right)N_t v_{th}\sigma_n}{p_0+(1+\gamma)n'+\left(\gamma e^{\frac{E_t-E_i}{kT}}+e^{-\frac{E_t-E_i}{kT}}\right)n_i} \\ &= \frac{\left(n'^2+n'p_0\right)/\tau_{n0}}{p_0+(1+\gamma)n'+\left(\gamma e^{\frac{E_t-E_i}{kT}}+e^{-\frac{E_t-E_i}{kT}}\right)n_i}\ , \end{aligned} \tag{C.2}$$

using the definition of the electron capture time constant: $\tau_{n0}=1/N_t v_{th}\sigma_n$. Under high-level injection $n'>>p_0$, resulting in the high-level SRH lifetime given by $(1+\gamma)\tau_{n0}$, which is independent of the defect energy. Under low-level injection $n'<<p_0$, giving the following expression for low-level SRH lifetime:

$$\tau_{SRH,ll}=\left[1+\frac{n_i}{p_0}\left(\gamma e^{\frac{E_t-E_i}{kT}}+e^{-\frac{E_t-E_i}{kT}}\right)\right]\tau_{n0}\ . \tag{C.3}$$

The initial decay time, τ_{eff}, is plotted versus injection level for 0.55 eV InGaAsSb in Figures C.1, C.2, and C.3 for various combinations of the defect energy (E_t-E_i), the capture cross-section ratio (γ), and the electron capture time constant (τ_{n0}). From the figures, the shape of the profiles appear to be determined primarily by the defect energy. Note that for defect energies near the conduction band, i.e., E_t-E_i>0.2 eV, the dependence on injection level resembles that of radiative recombination (Fig. 4.6); however, such shallow defects are generally not efficient recombination centers. The capture cross-section ratio determines the ratio of the high-level and low-level injection decay time for a given defect energy.

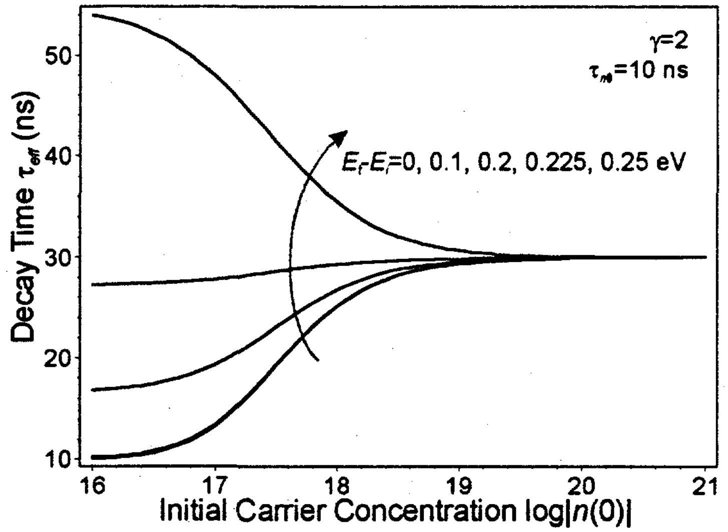

FIGURE C.1 Exponential Decay Time of SRH Model at t=10 ns for Different Defect Energies

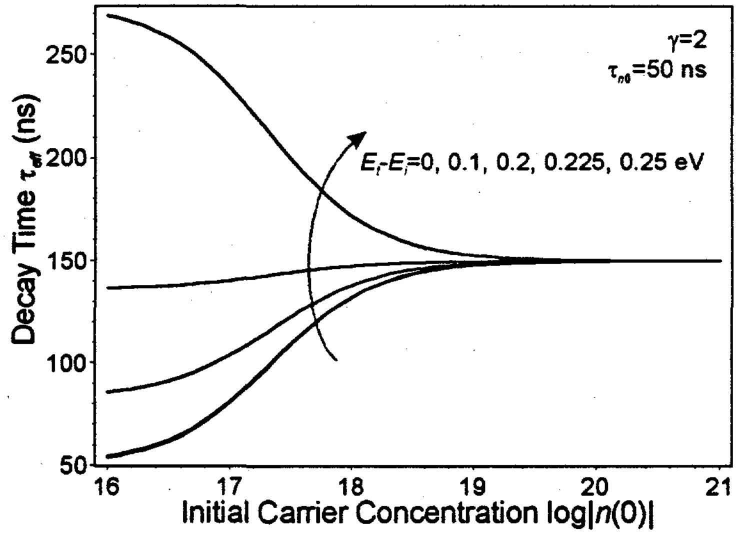

FIGURE C.2 Exponential Decay Time of SRH Model at t=10 ns for Different Defect Energies

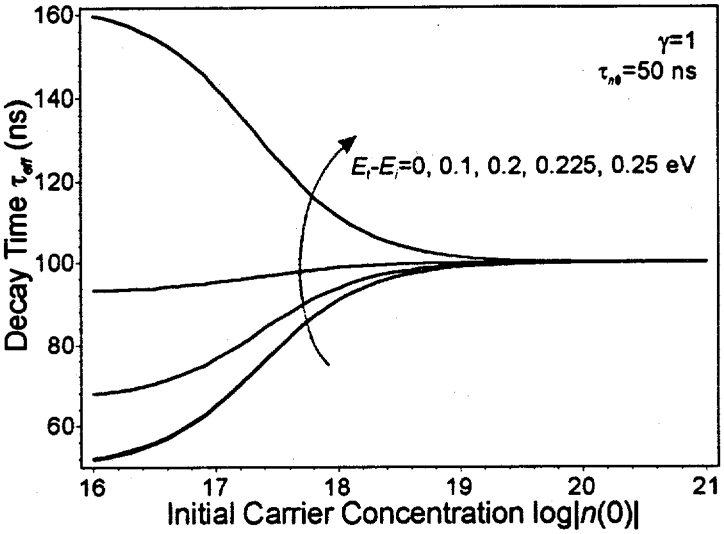

FIGURE C.3 Exponential Decay Time of SRH Model at t=10 ns for Different Defect Energies

Appendix D - Optical Constants

D.1. Measured Absorption Constants and Index of Refraction of III-V Semiconductors

1. GaAs[72]

Wavelength (nm)	Absorption Constant (cm^{-1})
50	2.498577e5
59	3.450427e5
69	3.247407e5
83	4.287100e5
95	9.342096e5
103	9.650485e5
177	1.304915e6
200	1.241557e6
248	2069810.0
253	2009910.0
258	1834170.0
264	1644290.0
270	1477660.0
276	1331280.0
282	1143260.0
288	984860.0
295	880860.0
302	818230.0
310	778650.0
318	752620.0
326	735280.0
335	724140.0
344	717140.0
354	714200.0
365	715280.0
376	723090.0
387	742210.0
400	674170.0
413	592480.0
428	505750.0
443	281330.0
459	190530.0
477	142200.0
496	111740.0
517	90340.0
539	74560.0
564	61460.0
590	51150.0
620	42790.0
653	34400.0
689	28720.0
729	21220.0
775	15060.0
785	14252.67
795	13755.34
805	13267.19
816	12786.67
827	12161.98
832	10994.25
838	10290.71
843	9893.372
849	9293.077
855	8993.824
861	8290.010
867	8290.616
870	8002.034
873	3900.454
879	850.3344
886	239.8054
892	80.01904
898	34.96875
905	18.46770
954	1
1300	0.1

Wavelength (nm)	Index of Refraction
49	1.049
65	0.981
103	0.895
155	0.899
177	1.063
188	1.247
200	1.424
248	1.882
270	3.291
282	3.486
310	3.513
344	3.391
400	4.149
443	4.929
459	4.748
495	4.427
540	4.127
590	3.888
729	3.627
895	3.603
900	3.595
1000	3.509
1200	3.433
1400	3.394
1500	3.375
1600	3.350
1800	3.300
2000	3.325
2500	3.325
3000	3.324
3500	3.324
4000	3.323
4500	3.323
5000	3.322

2. GaSb[72]

Wavelength (nm)	Absorption Constant (cm^{-1})
210	1.469e6
250	1.394e6
300	1.758e6
310	1.477e6
410	6.412e5
500	5.791e5
560	3.895e5
620	2.794e5
650	1.596e5
690	1.115e5
730	8.356e4
770	6.751e4
830	5.237e4
1000	3.246e4
1200	1.850e4
1400	1.054e4
1490	8.181e3
1530	7.441e3
1570	6.531e3
1600	5.804e3
1630	5.003e3
1650	4.433e3
1680	3.815e3
1700	3.001e3
1720	5.465e2
1750	1.314e2
1770	6.517e1
1800	3.770e1
1820	2.458e1
1850	1.712e1
1880	1.337e1
1910	9.227
1940	7.643
1970	7.017
2000	6.786

Wavelength (nm)	Index of Refraction
49	.885
65	.885
103	.885
155	.885
182	.885
200	.885
248	1.369
282	1.723
310	3.450
344	3.774
400	3.766
443	3.760
517	4.513
540	4.492
590	4.705
708	4.722
886	4.290
1000	4.231
1200	4.128
1400	4.025
1500	3.974
1800	3.820
1900	3.802
2000	3.789
2500	3.749
3000	3.898
3500	3.865
4000	3.833
4500	3.829
5000	3.824
6000	3.824
7000	3.843
8000	3.843
9000	3.843
10000	3.843

3. InAs[72]

Wavelength (nm)	Absorption Constant (cm^{-1})
49	2.154235e5
59	2.364182e5
67	2.016246e5
82	2.574573e5
95	3.723614e5
103	4.434831e5
108	4.828744e5
112	5.077038e5
124	5.426848e5
136	5.821186e5
153	6.373532e5
172	6.900545e5
180	6.974336e5
188	6.751082e5
195	6.830950e5
207	6.423082e5
225	6.545683e5
248	7.273800e5
259	8.257901e5
265	8.523793e5
270	8.333365e5
282	6.777819e5
310	3.646274e5
335	3.216616e5
344	3.156205e5
354	3.113194e5
387	3.070156e5
413	3.094431e5
443	3.131664e5
449	3.011509e5
459	2.759674e5
470	2.564920e5
477	2.482978e5
496	2.262453e5
517	1.559251e5
563	9.173674e4
620	6.425064e4
689	4.833219e4
775	3.753697e4
827	3.283736e4
1459	9.991083e3
1550	8.512703e3
1653	7.260063e3
1771	6.492507e3
1907	5.502317e3
2066	4.896384e3
2254	4.153487e3
2480	3.445618e3
2755	2.736778e3
3100	1.949814e3
3351	1.200012e3
3397	9.488590e2
3444	6.750228e2
3493	3.903382e2
3542	1.699405e2
3594	8.985969e1
3647	3.945296e1
3701	1.901423e1
3757	8.495763e0
3815	4.150361e0
3875	1.994405e0

Wavelength (nm)	Index of Refraction
49	1.139
65	1.120
103	0.745
155	0.987
177	1.270
188	1.483
200	1.650
248	1.987
270	3.100
282	3.800
310	3.678
344	3.271
400	3.260
443	3.817
459	4.087
495	4.485
540	4.420
590	4.200
729	3.870
895	3.690
900	3.685
1000	3.615
1200	3.560
1400	3.510
1500	3.510
1600	3.510
1800	3.510
2000	3.510
2500	3.510
3000	3.510
3500	3.510
4000	3.510
4500	3.510
5000	3.510

4. InSb[72]

Wavelength (nm)	Absorption Constant (cm^{-1})
50	3.847e5
60	4.256e5
70	2.754e5
90	3.671e5
100	6.222e5
160	1.070e6
210	1.160e6
300	1.357e6
410	5.507e5
520	5.469e5
620	3.709e5
710	1.899e5
780	9.729e4
890	5.673e4
1030	3.904e4
1240	2.635e4
1600	1.414e4
2000	1.068e4
2500	7.540e3
3000	5.445e3
3500	4.308e3
4000	3.456e3
4500	2.793e3
5000	2.287e3
6000	1.550e3
6500	1.218e3
7000	4.488e2
7500	8.713e1
8000	3.613e1
8500	2.957e1
9000	2.653e1

Wavelength (nm)	Index of Refraction
49	1.15
65	1.18
103	0.75
155	0.88
182	1.06
200	1.20
248	1.56
282	1.73
310	2.62
344	3.51
400	3.42
443	3.32
517	3.82
540	4.05
590	4.22
708	5.06
886	4.40
1000	4.24
1200	4.18
1400	4.12
1500	4.09
1800	4.06
1900	4.04
2000	4.03
2500	4.03
3000	4.03
3500	4.02
4000	4.02
4500	4.02
5000	4.01
6000	4.01
7000	4.01
8000	4.00
9000	3.97
10000	3.95

D.2. Calculated Absorption Constants of InGaAsSb Lattice Matched to GaSb

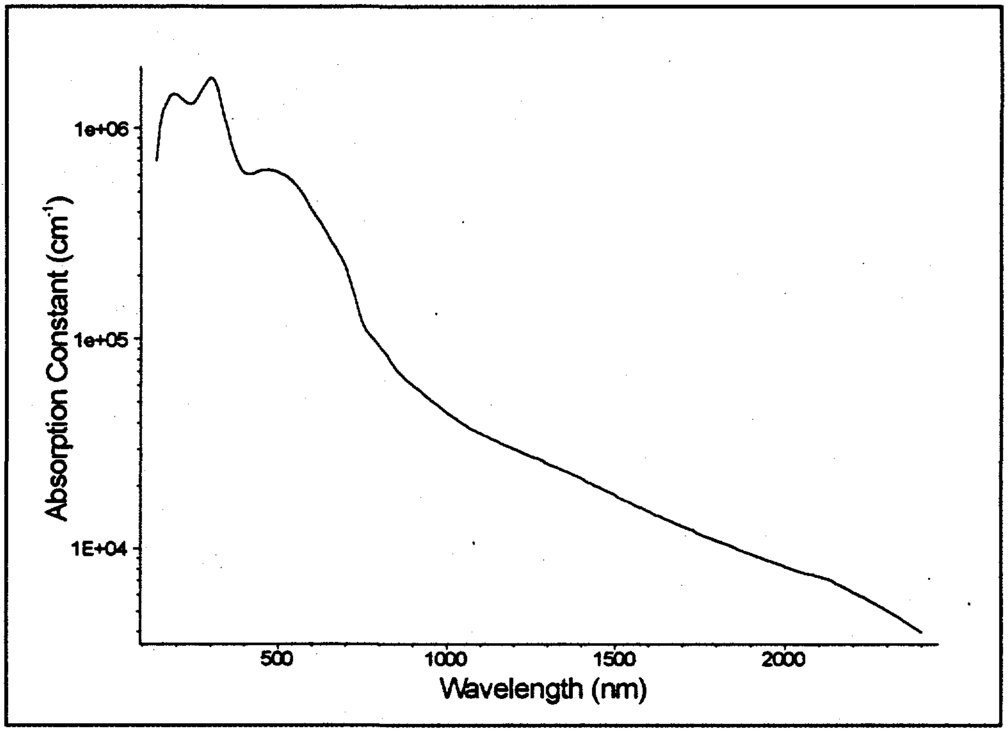

FIGURE D.1 Calculated Absorption Constant of 0.50 eV InGaAsSb

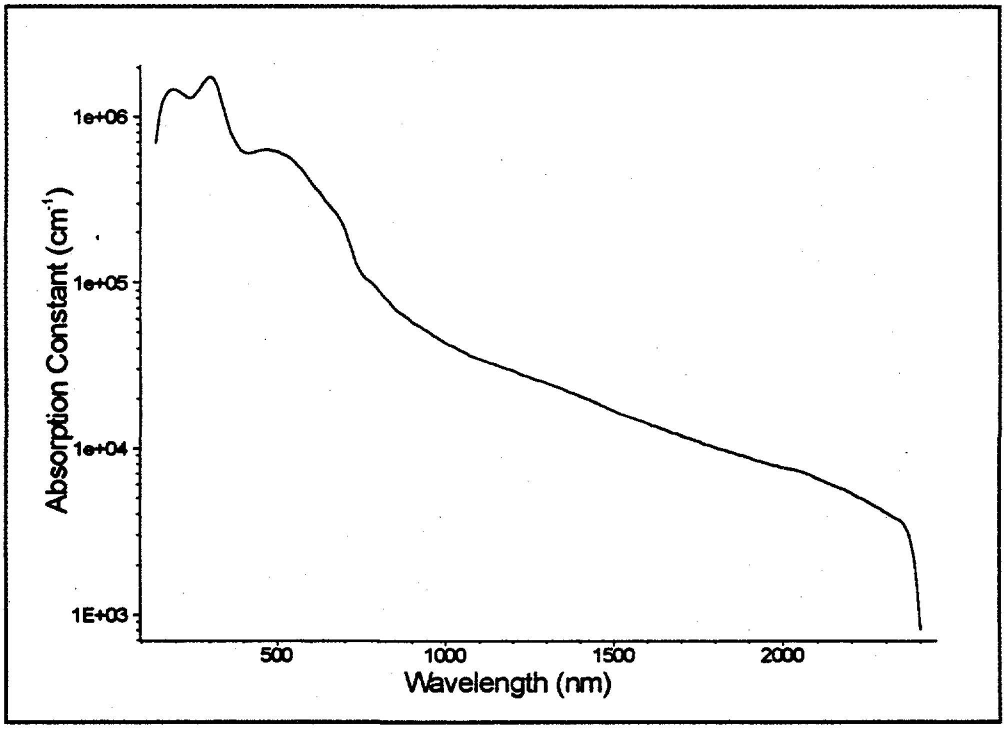

FIGURE D.2 Calculated Absorption Constant of 0.52 eV InGaAsSb

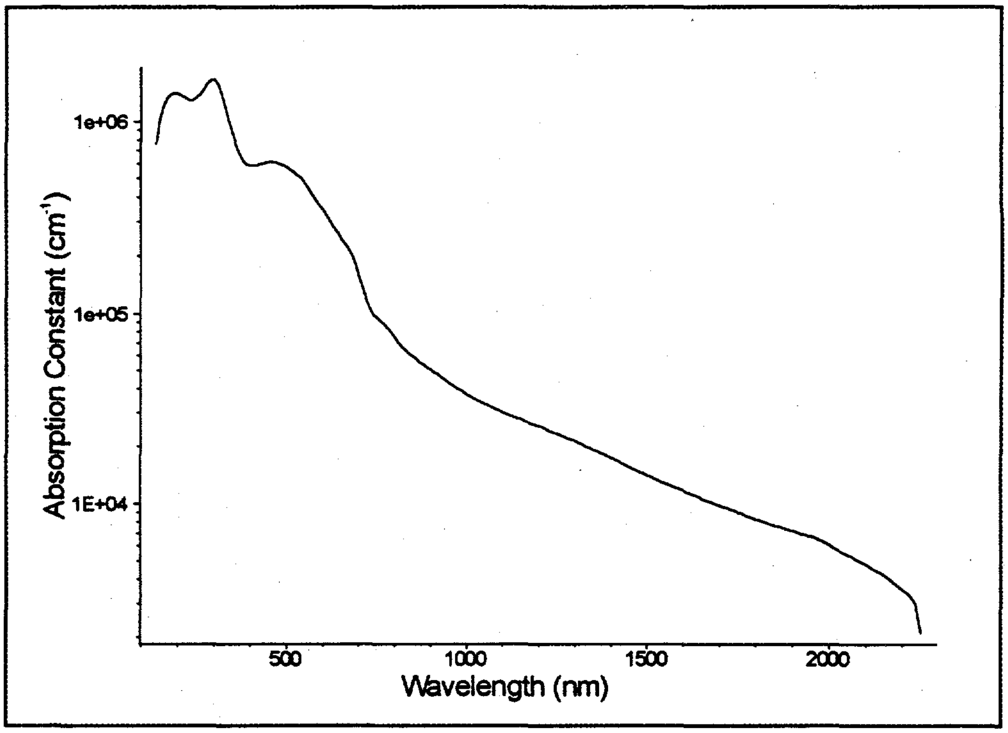

FIGURE D.3 Calculated Absorption Constant of 0.55 eV InGaAsSb

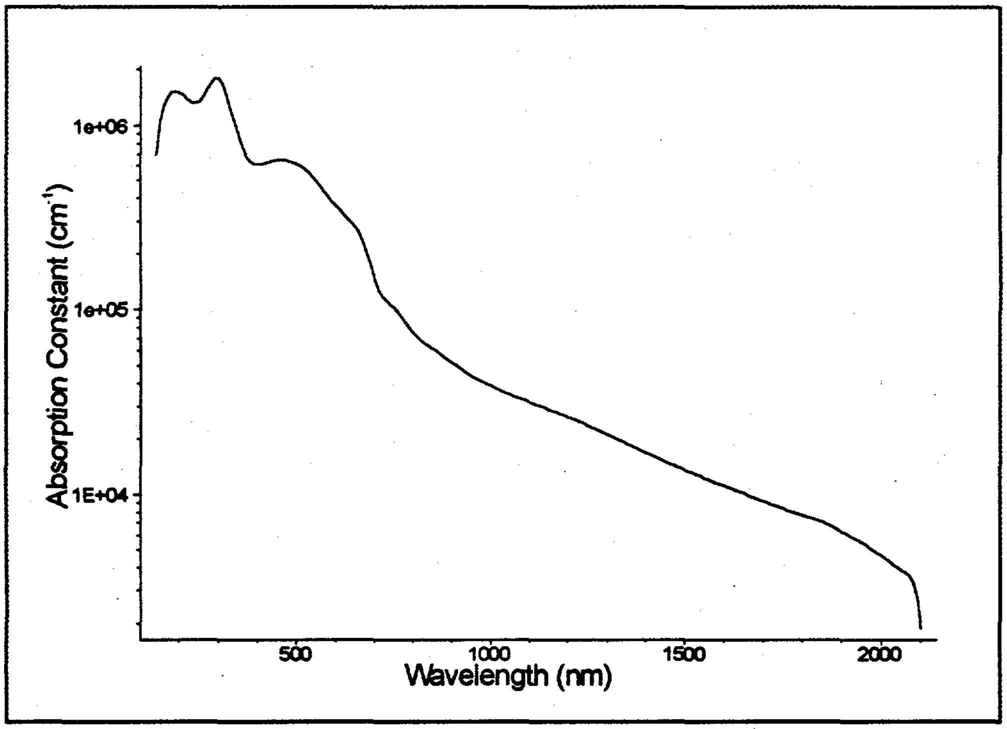

FIGURE D.4 Calculated Absorption Constant of 0.59 eV InGaAsSb

D.3. Calculated Absorption Constants of InGaAsSb Quasi-binary Substrates

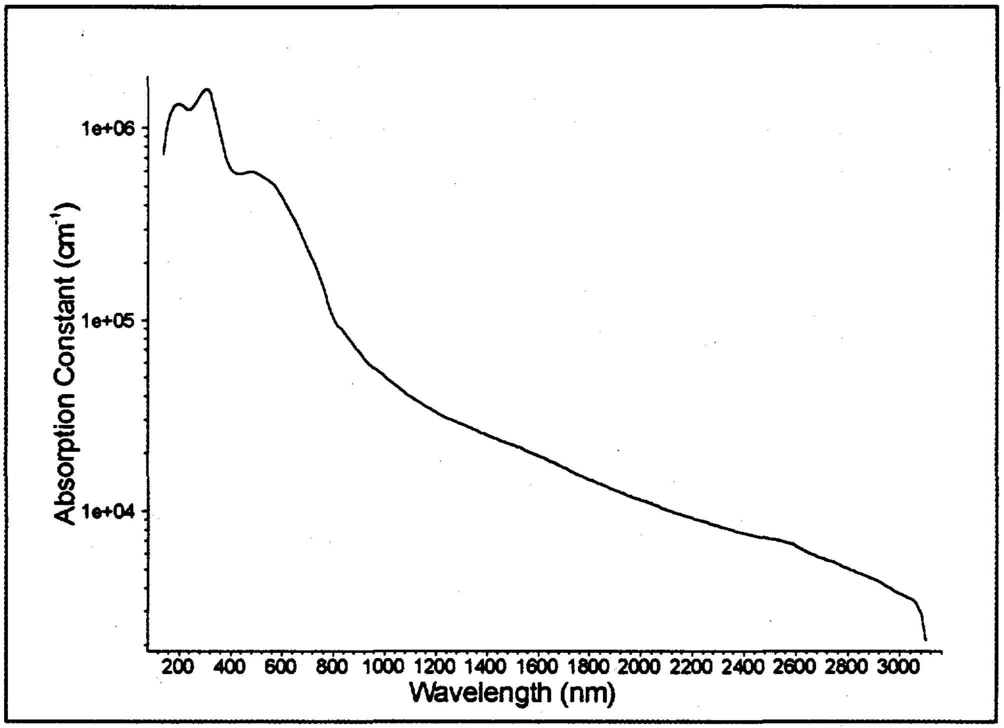

FIGURE D.5 Absorption Constant of 0.40 eV Quasi-binary InGaAsSb

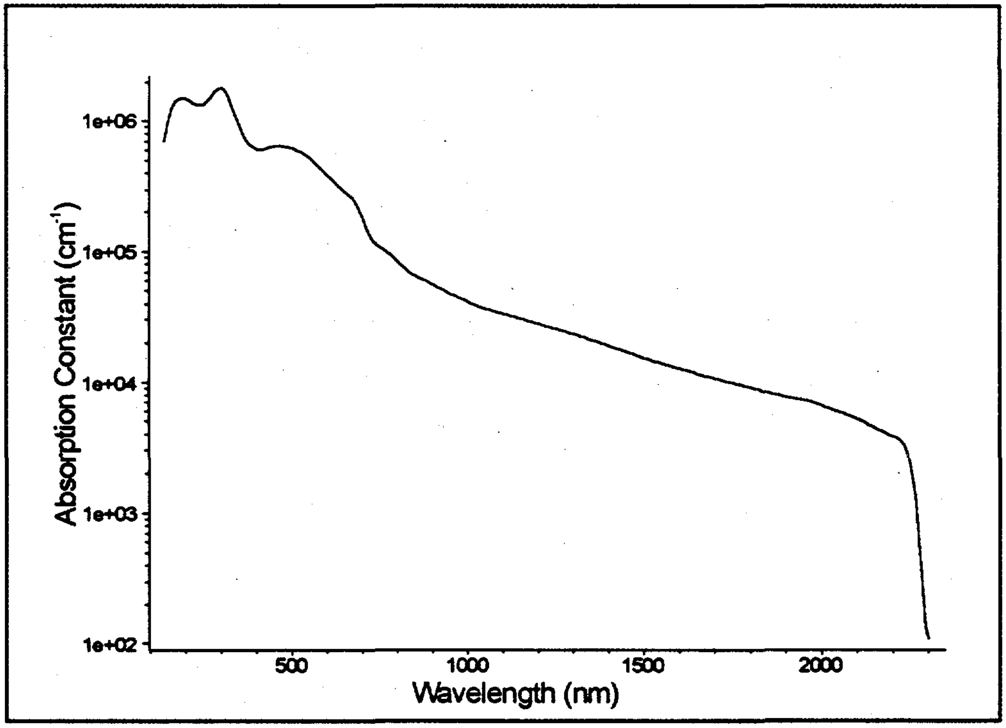

FIGURE D.6 Absorption Constant of 0.55 eV Quasi-binary InGaAsSb

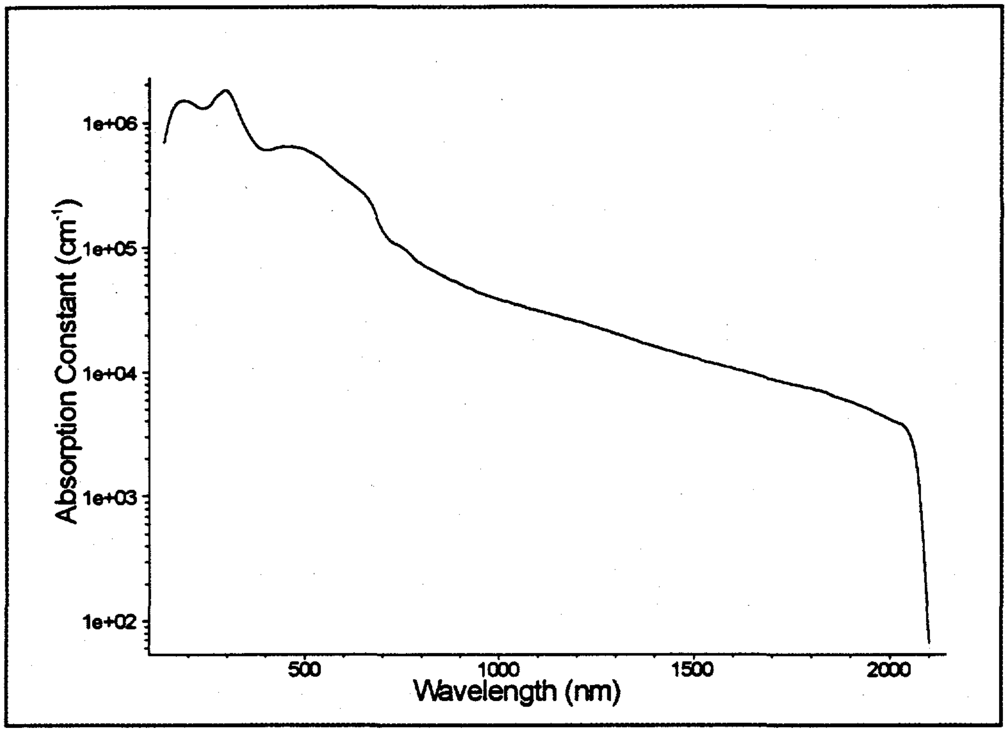

FIGURE D.7 Absorption Constant of 0.60 eV Quasi-binary InGaAsSb

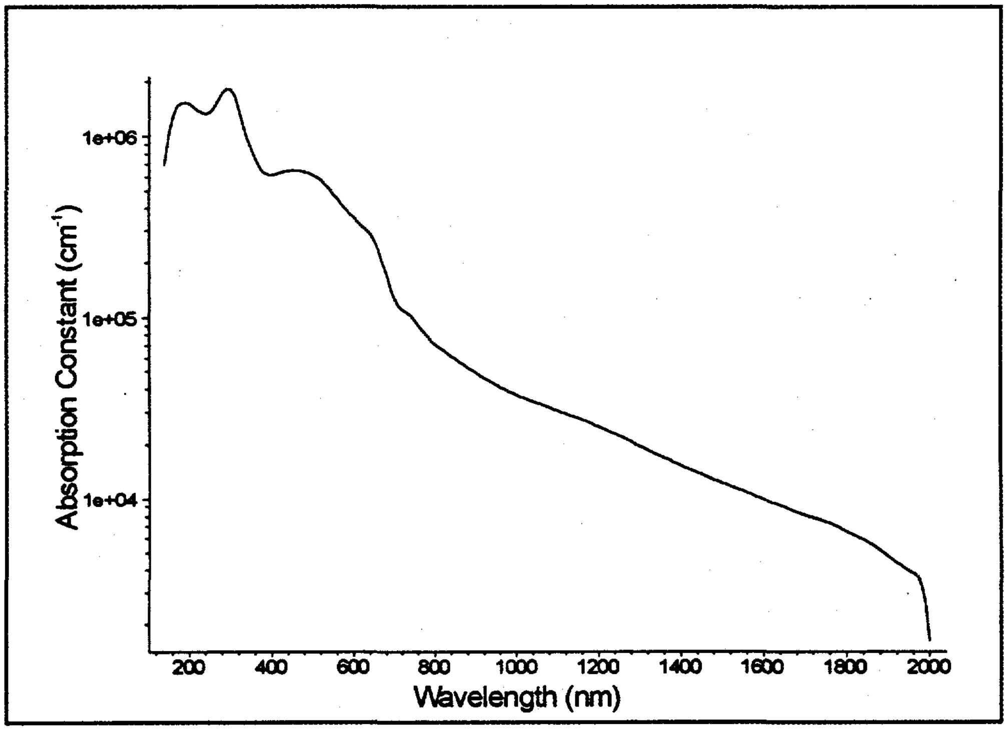

FIGURE D.8 Absorption Constant of 0.62 eV Quasi-binary InGaAsSb

Appendix E - Raw Data From Thick Substrates

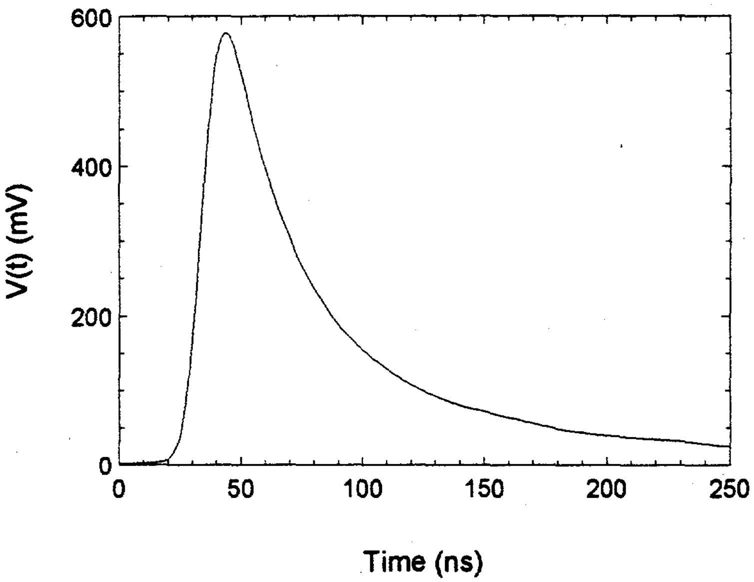

FIGURE E.1 Decay Transient from In-house GaSb Substrate at 1064 nm on a Linear Scale

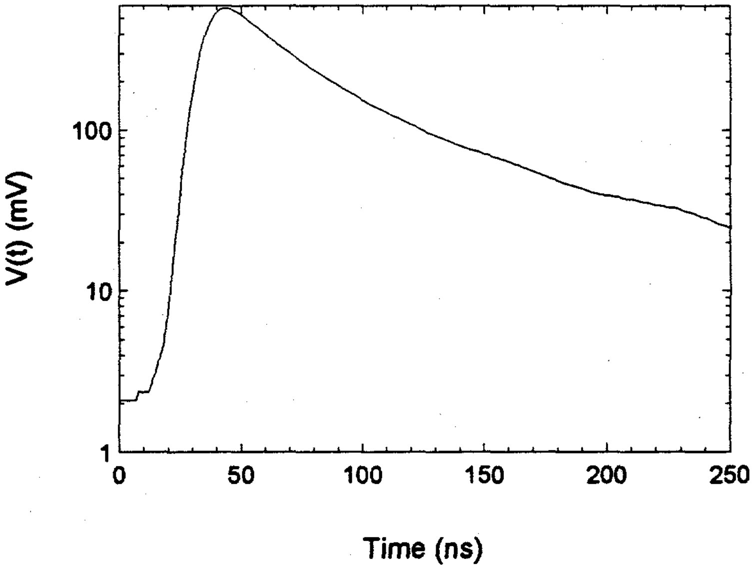

FIGURE E.2 Decay Transient from In-house GaSb Substrate at 1064 nm on a Log Scale

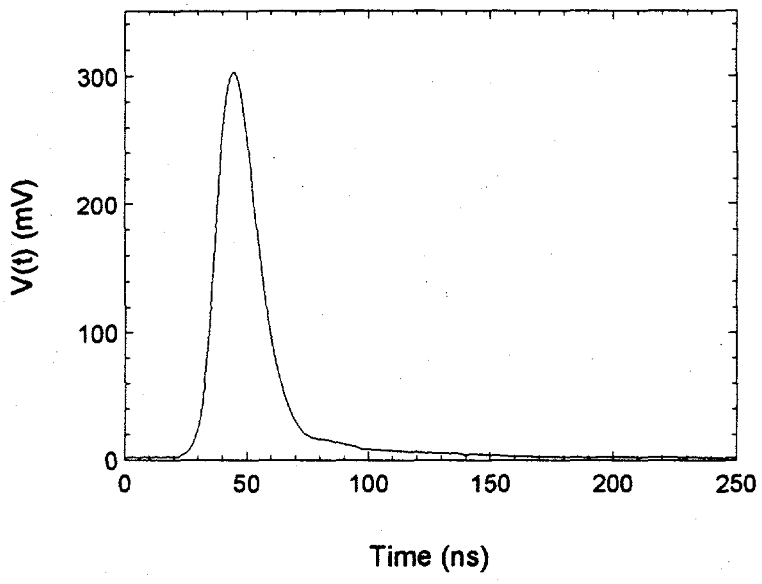

FIGURE E.3 Decay Transient from 0.55 eV Quasi-binary Substrate at 1064 nm on a Linear Scale

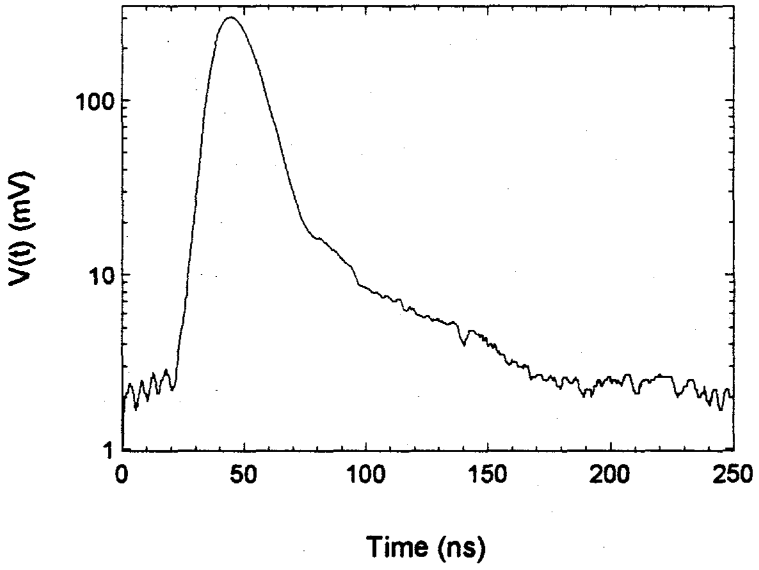

FIGURE E.4 Decay Transient from 0.55 eV Quasi-binary Substrate at 1064 nm on a Log Scale

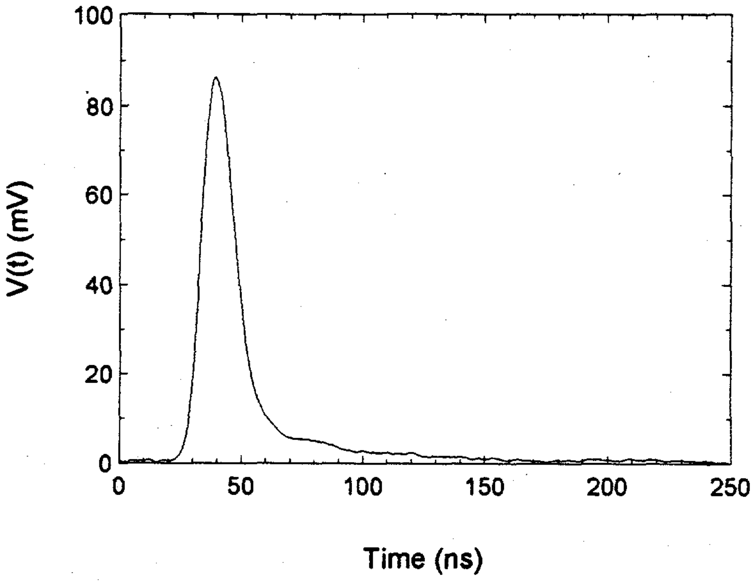

FIGURE E.5 Decay Transient from 0.55 eV Quasi-binary Substrate at 532 nm on a Linear Scale

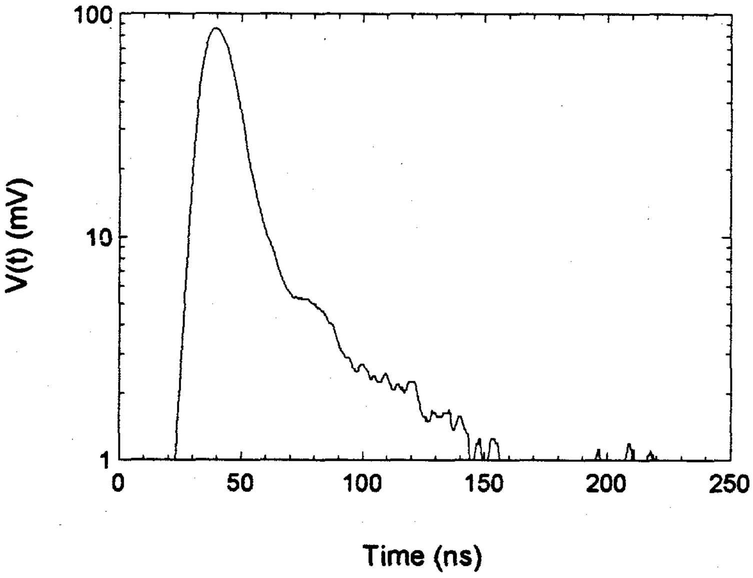

FIGURE E.6 Decay Transient from 0.55 eV Quasi-binary Substrate at 532 nm on a Log Scale

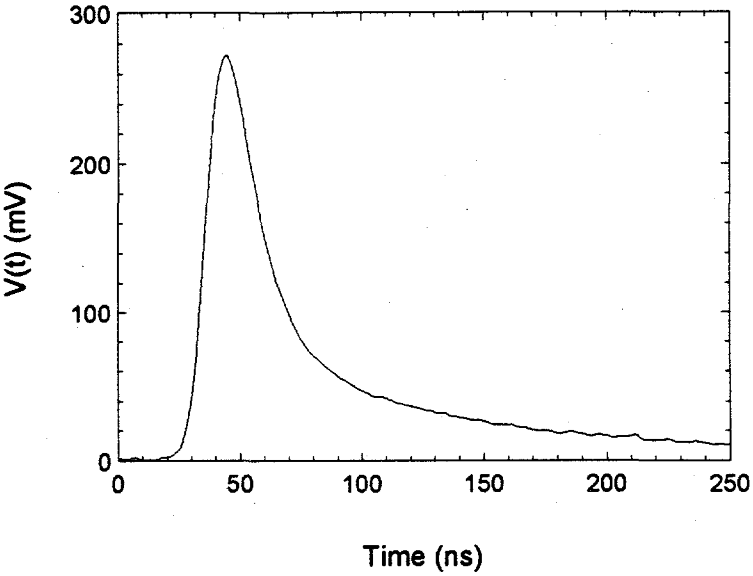

FIGURE E.7 Decay Transient from 0.4 eV Quasi-binary Substrate at 1064 nm on a Linear Scale

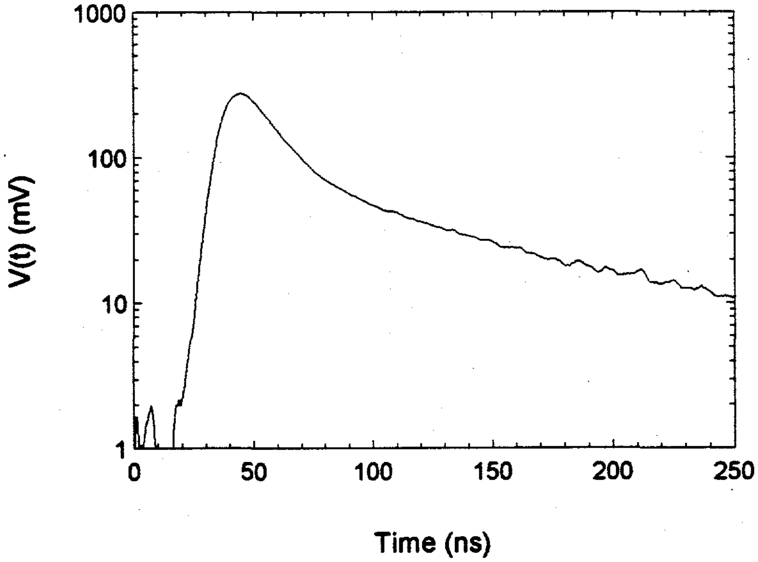

FIGURE E.8 Decay Transient from 0.4 eV Quasi-binary Substrate at 1064 nm on a Log Scale

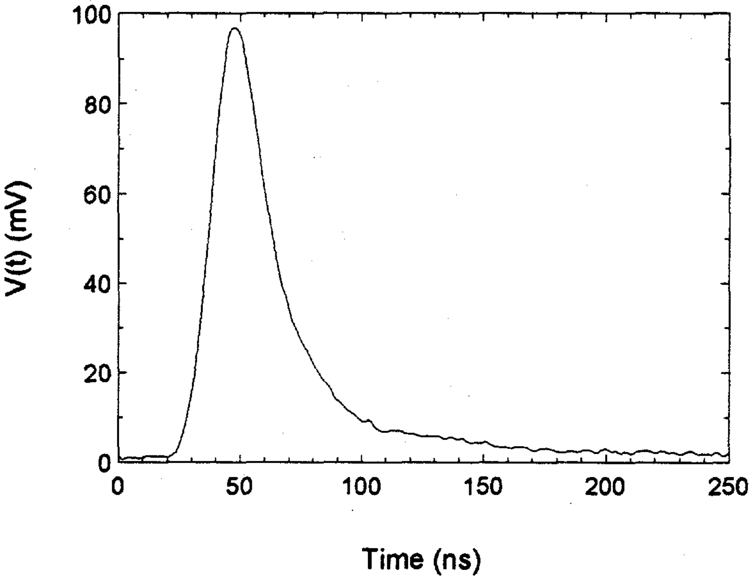

FIGURE E.9 Decay Transient from 0.62 eV Quasi-binary Substrate at 1064 nm on a Linear Scale

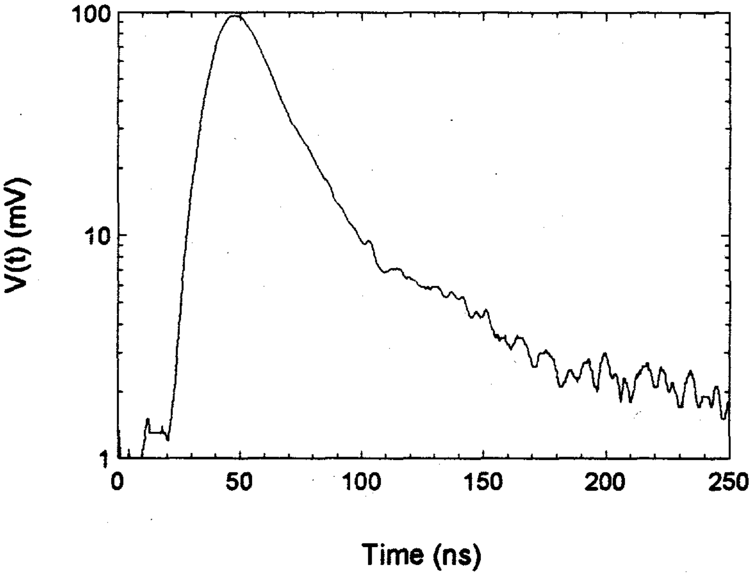

FIGURE E.10 Decay Transient from 0.62 eV Quasi-binary Substrate at 1064 nm on a Log Scale

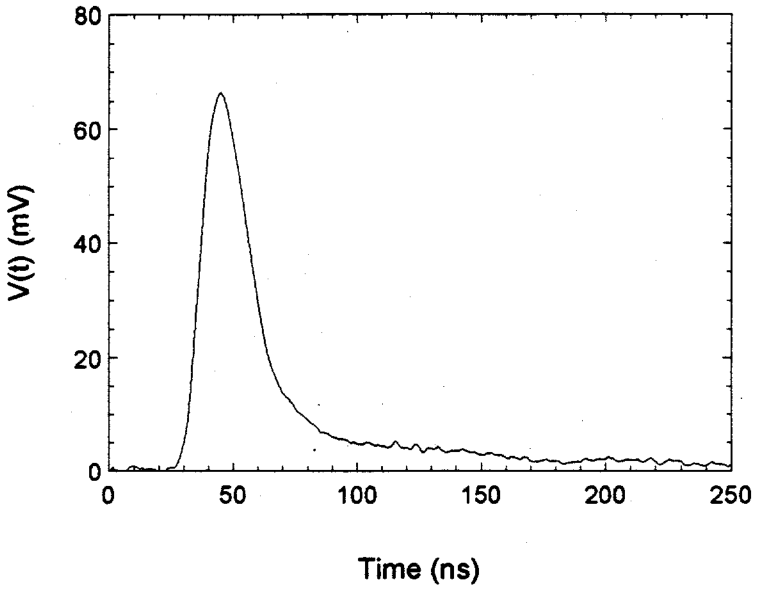

FIGURE E.11 Decay Transient from 0.62 eV Quasi-binary Substrate at 532 nm on a Linear Scale

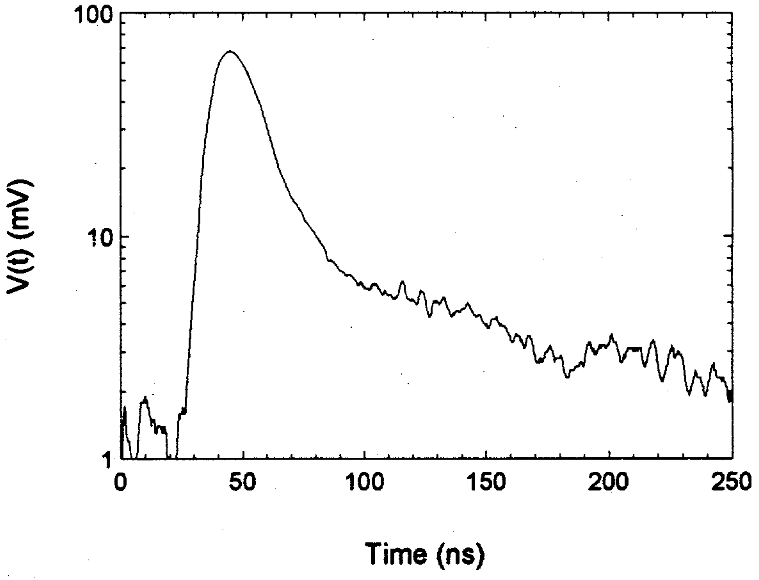

FIGURE E.12 Decay Transient from 0.62 eV Quasi-binary Substrate at 532 nm on a Log Scale

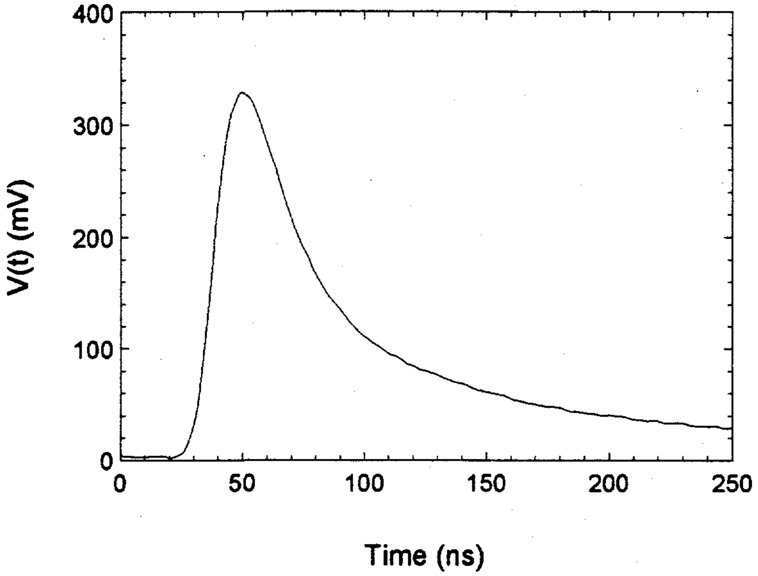

FIGURE E.13 Decay Transient from 0.6 eV Quasi-binary Substrate at 1064nm on a Linear Scale

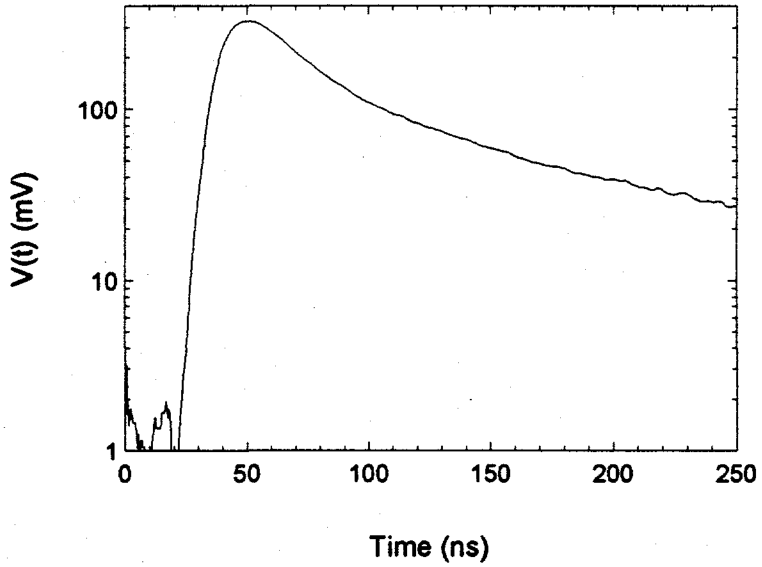

FIGURE E.14 Decay Transient from 0.6 eV Quasi-binary Substrate at 1064 nm on a Log Scale

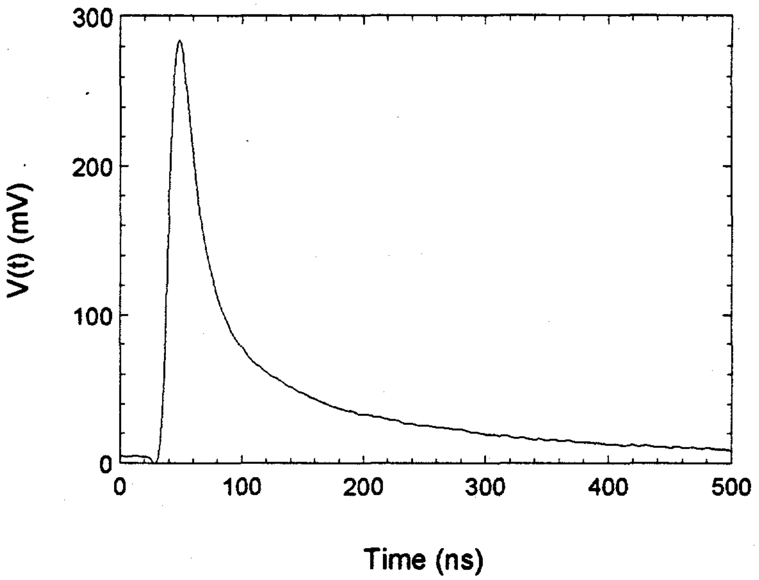

FIGURE E.15 Decay Transient from 0.6 eV Quasi-binary Substrate at 532 nm on a Linear Scale

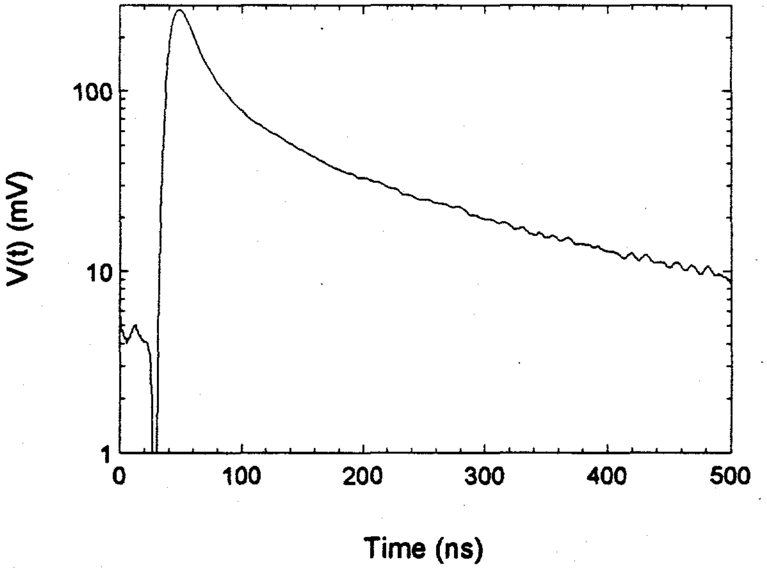

FIGURE E.16 Decay Transient from 0.6 eV Quasi-binary Substrate at 532 nm on a Log Scale